# Selected topics in Computational Relativity

by

Soham Mukherjee

A thesis
presented to the University of Waterloo
in fulfillment of the
thesis requirement for the degree of
Doctor of Philosophy
in
Physics

Waterloo, Ontario, Canada, 2022

© Soham Mukherjee 2022

**Examining Committee Membership**

The following served on the Examining Committee for this thesis. The decision of the Examining Committee is by majority vote.

| | |
|---|---|
| External Examiner: | Bernd Brügmann<br>Theoretical Physics Institute, University of Jena |
| Supervisor(s): | Erik Schnetter<br>Physics and Astronomy, University of Waterloo<br>Perimeter Institute for Theoretical Physics |
| | Avery Broderick<br>Physics and Astronomy, University of Waterloo<br>Perimeter Institute for Theoretical Physics |
| Internal Member: | Niayesh Afshordi<br>Physics and Astronomy, University of Waterloo<br>Perimeter Institute for Theoretical Physics |
| Internal-External Member: | David Del Rey Fernandez<br>Department of Applied Mathematics, University of Waterloo |
| Other Member(s): | Luis Lehner<br>Physics and Astronomy, University of Waterloo<br>Perimeter Institute for Theoretical Physics |

## Author's Declaration

This thesis consists of material all of which I authored or co-authored: see Statement of Contributions included in the thesis. This is a true copy of the thesis, including any required final revisions, as accepted by my examiners.

I understand that my thesis may be made electronically available to the public.

## Statement of Contributions

Chapter 2 contains yet to be published work done by me during the first half of my PhD. The code for this project is open-source, and is available [here]. Chapters 3 and 4 contain work done in collaboration with Nathan K. Johnson-McDaniel, Wolfgang Tichy, and Steve Liebling that has been submitted for publication, and is available at [1]. The evolutions reported in Chapter 4 were carried out by Nathan K. Johnson-McDaniel and Steve Liebling. In both chapters 3 and 4, I performed all the analyses, created all the figures, and contributed significantly to the writing of the text, as well as the numerical code for the initial data solver.

Chapter 5 contains work done in collaboration with Chunxiao Li, Jonathan Chung, Marc Vinyals, Noah Fleming, Antonina Kolokolva, Alice Mu, and Vijay Ganesh, and published at [2]. My contribution to this work has been towards the empirical analyses presented in Sec. 5.1 and 5.2 of the paper, where I built the empirical hardness model for SAT instances, for which the code is available [here]. The chapter has been adapted from the paper to best fit the thesis.

## Abstract

This thesis addresses a collection of topics that are either directly related to, or have implications for, current challenges in computational relativity. Consequently, it is divided into three parts, each with its own separate focus.

In the first part, we explore a spacetime discretization method for computational relativity, where, instead of foliating spacetime into space-like hypersurfaces for evolution, we decompose spacetime into spacetime volume elements with null boundaries. This offers unique computational advantages, for distributing the computation over a large number of processes, as well as for studying spacetime regions close to black hole singularities. In Chapter 2, we describe an evolution scheme based on spacetime volume elements in spherical symmetry, and consider evolutions of a Schwarzschild black hole and a self-gravitating massless scalar field to test the stability and convergence of our discretization scheme.

In the second part, we present a method to construct initial conditions for numerical evolution of charged, spinning black hole binaries. Evolution of these initial conditions provide a proxy for binary black hole waveforms in modified theories of gravity. Such waveforms are expected to play a crucial role in testing general relativity using gravitational wave observations. In Chapter 3, we construct conformally curved initial conditions for different configurations of orbiting binaries, e.g., with black holes that are highly charged or rapidly spinning (90 and 80 percent of the extremal values, respectively), and for generic spinning, charged black holes. In Chapter 4, we report on exploratory evolutions of head-on collisions of charged binary black holes, and orbiting binaries for the uncharged case.

In the third part of the thesis, we focus on building an empirical understanding of why Boolean Satisfiability (SAT) solvers—which form the basis of formal verification methods—are efficient for real world problems, when, theoretically, the Boolean SAT problem is computationally intractable. Understanding what makes SAT solvers efficient for real world instances could open up the possibility of using formal methods for problems that are currently inaccessible due to their scale; e.g., verification of computational relativity software. In Chapter 5, we build and evaluate a statistical model based on the hierarchical community structure of a Boolean SAT formula, to understand why certain SAT problems are computationally easier to solve, than others. We find that although we improve on existing results, our parameterization is insufficient for building a general hardness model for the SAT problem.

**Acknowledgements**

I struggled during my PhD. In hindsight, I might have left the program long ago, if not for the support and encouragement I had from my advisor, Erik Schnetter. Thank you for being patient with me, and sharing your ideas, advice, and wisdom, for physics, and for life; perhaps the most memorable of which would be T.T.T; that Things Take Time.

I am also indebted to Nathan K. Johnson-McDaniel for being my mentor, and the most patient of collaborators for the past 6 years, and Vijay Ganesh, for introducing me to the wonderful world of SAT and many other areas of computer science, but more importantly, for believing in me, when I did not believe in my own ability to do good research.

I would also like to express my gratitude to Niayesh Afshordi, Luis Lehner, and Avery Broderick for their guidance, and being a part of my advisory committee. I have learnt a lot from each of you.

I am especially grateful to have had wonderful friends during my time here in Waterloo. The list is long, but in particular, Saumya, Vasanth, Navya, Supranta, Aditya, Matthew, Fiona, Tomáš, Max, Nils, Mike, and Celine—thank you, for being a part of my life. Finally, I would like to thank my Mom and Dad for their unconditional and unwavering support, and Angela, for being the light at the end of the tunnel.

# Table of Contents

**List of Tables** ix

**List of Figures** x

**1 Introduction** 1

**2 A Spacetime Discretization Method for Computational Relativity** 9

2.1 The computational algorithm . . . . . 10

2.1.1 Spacetime elements using double null coordinates . . . . . 10

2.1.2 Pseudospectral Collocation Method . . . . . 12

2.1.3 Asynchronous parallelism model . . . . . 15

2.2 Numerical Tests . . . . . 15

2.2.1 Scalar wave on 1+1D Minkowski . . . . . 16

2.2.2 Schwarzschild spacetime . . . . . 17

2.2.3 Self-gravitating scalar field . . . . . 20

2.3 Discussion . . . . . 24

**3 Initial data for charged black hole binaries** 26

3.1 Initial Data Formalism . . . . . 27

3.1.1 The XCTS formalism for vacuum GR . . . . . 27

3.1.2 Extending to electrovacuum GR . . . . . 31

3.2 Numerical Method . . . 34
3.2.1 Surface Fitting Coordinates . . . 34
3.2.2 Computing diagnostics . . . 37
3.2.3 Controlling BH spin and ADM linear momentum . . . 39
3.3 Results . . . 40
3.4 Conclusions . . . 44

**4 Exploratory evolutions of charged binary black hole initial data 45**
4.1 Uncharged binary black holes in orbit . . . 46
4.2 Head-on collisions of charged binary black holes . . . 47
4.3 Head-on collisions of boosted uncharged binary black holes . . . 49
4.4 Discussion . . . 52

**5 Towards a parameterized hardness model for Boolean SAT instances 54**
5.1 HCS of a Boolean SAT formula . . . 55
5.2 Empirical hardness model for SAT using HCS . . . 57
5.2.1 Predicting the category of a SAT instance . . . 59
5.2.2 Predicting the runtime of a SAT instance . . . 61
5.3 Conclusions . . . 62

**6 Summary & Future Directions 64**

**Bibliography 67**

**Appendices 83**

**A Pseudospectral method using Chebyshev Gauss Lobatto points 84**

**B Kerr-Newman black hole in Kerr-Schild coordinates 85**

**C Linearized XCTS equations 87**

# List of Tables

3.1 Summary of the parameters of the initial data sets for orbiting binaries ("qc" for "quasicircular"), also indicating the case for which we performed a test evolution with BAM. Here $\mathcal{Q}_A$ and $\boldsymbol{\chi}_A$ are the dimensionless charge and spin on black hole $A$, respectively. Additionally, $q$, $\Omega_0$, correspond to the mass ratio and angular velocity, respectively. We set the radial velocity, i.e., $\dot{a} = 0$ for all the cases, except for `qc-sp5` where we set $\dot{a} = 0.006531$. Finally, $d$ is the separation between the two black holes and $\zeta$ is the attenuation width parameter defined in Eq. (3.43). We set the velocity of each black hole using the Newtonian expression in terms of $\Omega_0$ and $d$. . . . . 40

4.1 Summary of the parameters of the initial data sets for head-on collisions (abbreviation "ho" ) of equal-mass, equal-charge, nonspinning binaries we constructed and performed test evolutions of with HAD and BAM. Here, $v$ is the magnitude of the velocity of each black hole. We set $d = 10M_{\rm T}$ and $\zeta = 2$ for all configurations listed here and set $\dot{a}_0 = -v/d$ for the head-on collisions. . . . . 49

# List of Figures

2.1 Spacetime discretization using spacetime volume elements in 1+1 dimensions or spherical symmetry. (A) On the right, we show the tiling to spacetime using spacetime volume elements with null boundaries. Elements with the same number are causally disconnected from each other and are solved parallel. Initial data on the incoming surfaces is computed by either solving the constraint equations on the boundaries $(u_0, v_0)$, or using the solution on the outgoing boundaries from elements in the past of an element, i.e., those with a lower number. (B) Each spacetime volume element (shown here with 5 collocation points in each direction) has two incoming null boundaries $(u_{\rm in},\ v_{\rm in})$ (marked in green) and two outgoing null boundaries $(u_{\rm out},\ v_{\rm out})$ (marked in blue, with red borders). Given the initial data on $(u_{\rm in}, v_{\rm in})$, we do an implicit solve for the entire element to compute the solution on the collocation points marked in blue. . . . . 11

2.2 An example showing $p$ and $h$ refinement of a spacetime element as implemented in our numerical scheme. (A) A single spacetime element. (B) The spacetime element in (A) after $p$ refinement, where the order of the element has been increased by 1. (C) The spacetime element in (A) after $h$ refinement, where the spectral order in each element remains the same, but the size of each element decreases from $h$ to $h/2$. . . . . 14

2.3 (Left) Solution to the scalar wave equation in 1+1 dimensions for $\sigma = 0.5$, computed using $N_p = N_h = 8$. The time coordinate $t = v + u$ increases diagonally from $u = v = -1$ to $u = v = 1$. (Right) Exponential decay of the expansion coefficients $(c_{pq})$ of $\Psi$ with polynomial order $p$. . . . . 17

2.4 Convergence results for the evolution of a scalar wave in 1+1 dimensions for different values of $\sigma$. On the left, we show the convergence of the error $\mathcal{E}_p$ with increasing $p$ in each element. On the right, we plot the convergence of $\mathcal{Q}_h$ with increasing the number of elements. . . . . 18

2.5 The metric component $r(u,v)$ (left) and the logarithm of the norm of the constraint violations (right) for the evolution of a Schwarzschild spacetime, with $N_p = 4, N_h = 16$. The horizon is located at $u = 0$, and the black hole singularity at $(uv = 1)$ (shown as the dashed black line). Here, the time coordinate increases from left to right, and the radial coordinate increases from top to the bottom (as shown by the colour scheme) in each figure. . 19

2.6 (Left) Convergence the constraint violations $\mathcal{C}$ for the evolution of Schwarzschild spacetime in three different computational domains at different distances $(r_1 = 0.404M, r_2 = 1.241M, r_3 = 2.541M)$ from the singularity. (Right) Convergence of the ratio $(\mathcal{Q} = \mathcal{C}_h/\mathcal{C}_{h/2})$ with $h$ refinement. Here, we used $N_p = 4$ in each element. . . . . 20

2.7 Initial conditions for $\Psi(u,v)$ and the corresponding solution to Eq. (2.5) for $a(u,v)$ for different values of $k$. . . . . 21

2.8 $p$ and $h$ convergence the of the constraint violations for the evolution of a self-gravitating scalar field on a computational domain not containing $r = 0$, for different values of the wave number $k$. For $p$ refinement, we used $N_h = 2$, and for $h$ refinement we set $N_p = 4$ in each element. . . . . 22

2.9 (Left) The error $(\Psi - \Psi_p)$ in numerical solution for the evolution of a scalar wave equation on a Minkowski background in spherical symmetry, for $N_p = 18, N_h = 1$. (Right) The maximum of absolute value of the coefficients $c_{pq}$ along $q$ for each $p$, for the numerical solution $\Psi_p$ computed using $N_p = 18$ points. . . . . 24

3.1 The $\phi = 0$ slice in the coordinates we use for the binary black hole configuration `qc-sp7cp5` (see Table 3.1). The black holes are centered at $x = \pm 5M_{\rm T}$, where $M_{\rm T}$ is the total mass of the superposed black holes. Lines of constant $A_{\rm Ans}$ and $B_{\rm Ans}$ are shown using purple and red, respectively. The excision surfaces are ellipsoids located at $A_{\rm Ans} = 0$. The grid is separated into two computational subdomains that meet along the $yz$-plane (seen here only as the line $x = 0$). . . . . 36

3.2 Convergence of the constraint residuals for four different binary configurations, a highly spinning case (`qc-hs`), highly charged (`qc-hc`) and moderately charged (`qc-mc`) cases, and a more generic charged and spinning case (`qc-sp7cp5`). In all cases, we show the Hamiltonian and momentum constraints ("ham" and "mom"), and for the charged cases, we also show the electric and magnetic constraints ("div E" and "div B"). The horizontal axis gives the number of points used for each coordinate ($N$) and the vertical axis shows the $L^2$ norm of the physical constraints over the entire computational grid (scaled by the total volume of the computational grid). Hence, we scale the $L^2$ norm by the square of the total Christodoulou mass $M_{\mathrm{T,C}}$. For the momentum constraint, this includes the Euclidean vector norm on the components of the constraint. For $N = 12$, the initial data solver does not converge for `qc-hs` and `qc-sp7cp5`, since the larger gradients near the horizon from significant spin require more resolution to reach the convergent regime. . . . . 41

3.3 The electric (top panel) and magnetic (bottom panel) fields (multiplied by $M_{\mathrm{T,C}}$) at the grid points around the two black holes in the $xy$-plane for `qc-sp7cp5`. The arrows represent the unit vectors of the projection of the field into the $xy$-plane. The magnitude of the projection is shown by the color scheme. The black hole on the left (right) has its spin aligned along the $x$- ($y$-) axis giving rise to two magnetic dipole moments aligned with the two spin axes. . . . . 43

4.1 The real part of the $l = m = 2$ mode of the Weyl scalar $\psi_4$ from the uncharged, quasicircular, aligned-spin evolution `qc-sp5`. The left panel shows the complete waveform, and the right panel shows the waveform around the merger. . . . . 47

4.2 Puncture tracks of the two black holes for the `qc-sp5` evolution. The tracks show approximately 8 orbits before merger and demonstrate the nonnegligible eccentricity of $\sim 0.06$. . . . . 48

4.3 A comparison of the real part of the $l = m = 2$ mode of $\psi_4$ from the head-on collision of two uncharged black holes starting from rest (`ho-v0q0`) evolved using HAD and BAM. The waveforms are not aligned in any way. . . . . 50

4.4 The $l = 2, m = 0$ mode (in the rotated frame with the black holes on the $z$-axis) of $\psi_4$ (top panel) and $\Phi_2$ (bottom panel) aligned at merger using the peak of the amplitude of the real part of the waveform. These waveforms correspond to head-on collisions of equal-mass, nonspinning charged black holes evolved using HAD for different charge to mass ratios, i.e., `ho-v0qp1`, `ho-v0qp3`, and `ho-v0qp5`. . . . . 51

5.1 (Left) The variable incidence graph (VIG) of the Boolean formula given in Eq. (5.3) with nested circles showing the hierarchical community structure. Here, $C$ represents the root level community, that is the entire graph. Further, $C_1$ and $C_2$ are the two sub-communities containing nodes $(x_1, x_2, x_3)$ and $(x_4, x_5, ..., x_8)$ respectively. The community $C_2$ can be further decomposed into two communities $C_{2,1}$ and $C_{2,2}$, with literals $x_4$ and $(x_5, ..., x_8)$, respectively. (Right) The hierarchical structure of the partition of the vertex set shown as a tree. . . . . 57

5.2 An example of a two–level decision tree, with one root node (red), one internal node (blue) and three leaf nodes (green). At the root node, the data $Q_m = \{x_i, y\}$ where $x_i$ are the set of features, and $y$ are the corresponding labels, is split into two subsets $(Q_{m,l}, Q_{m,r})$ on the $j^{\text{th}}$ feature, using a threshold $t_m$. The subset $Q_{m,r}$ is further split into $Q_{m,r,l}$ and $Q_{m,r,r}$ on the the $k^{\text{th}}$ feature for threshold parameter $t_n$. A split is only considered if the resulting tree minimizes an overall cost function; else the node terminates as a leaf node. In this simple case, learning the decision tree would involve learning the parameters $(j, t_m, k, t_n)$ that minimizes the associated cost function for the tree. . . . . 58

5.3 A 2D t–SNE embedding of our 49 dimensional data showing a clear separation between different categories of SAT instances. The axes $x_1$ and $x_2$ are arbitrary directions chosen by the t–SNE algorithm for the lower dimensional embedding. Note that the structure of a t–SNE embedding depends on the choice of certain parameters for the t–SNE algorithm. We verified that presence of well-separated clusters in the figure is independent of the choice of such parameters. . . . . 60

5.4 Predicted solving time ($t_{\text{pred}}$) vs. the actual solving time ($t_{\text{true}}$) for SAT instances with varying levels of hardness computed using the random forest regression model. . . . . 62

# Chapter 1

# Introduction

The next generation of gravitational wave (GW) detectors [3, 4, 5] are expected to probe the strongest, most dynamical regions of the spacetime with much higher sensitivity than current detectors in operation. This would require gravitational waveform models with much higher accuracy [6, 7] than those currently available, and numerical (computational) relativity (NR) is expected to play a crucial role in the development of such models [8]. For NR applications, where one often uses distributed computing to solve a set of time dependent partial differential equations (PDE), a significant bottleneck to improving the computational efficiency of a parallel algorithm is the amount of communication required between processes [9, 10]. Relative to computation, exchanging data between processes (depending on their physical proximity on the distributed computing hardware) is much more expensive on modern supercomputers, due to their hierarchical memory architecture. This limits the computational scalability of these algorithms, which makes it challenging to improve the accuracy of these large scale numerical simulations, or study interesting astrophysical scenarios that are particularly expensive to simulate (e.g., binary black hole mergers with intermediate mass ratios with $q \sim 1/100$, or binary neutron star mergers with more realistic astrophysics). To make progress, one thus needs to develop algorithms that are not only accurate, but also make efficient use of the current and next generation of distributed computing hardware [8].

Most large scale evolution codes for NR (e.g., [11, 12, 13]) use a method of lines approach, or in the context of numerical relativity, a 3+1 decomposition of spacetime, to construct a time evolution scheme. In this approach, spacetime is foliated into spacelike hypersurfaces, which are then evolved using a time-stepping scheme. To distribute the computation over multiple processes, each spacelike hypersurface is further subdivided into smaller computational patches that are solved in parallel. Since these computational

patches share timelike boundaries, they need to exchange boundary data at every time step, during evolution. This kind of evolution thus alternates between a computation phase and a communication phase at every time step. The communication cost, thus, depends both on the amount of data that needs to be communicated at every time step, as well as the number of communication phases (equivalently, time-steps) required during evolution.

To improve the computational scalability, several recent works [9, 10, 14] have investigated more efficient spatial discretization methods (e.g., those based on discontinuous Galerkin finite element or wavelet based reconstruction methods) to decrease the amount of data that needs to be communicated at each time step, as well as different models of parallelism (e.g., task-based, instead of patch-based parallelism) to balance the computational load more efficiency across multiple processes. However, all these approaches use a time-stepping scheme, and hence require communication at every time-step. This becomes a major part of the communication overhead, especially if one requires high spatial resolution in some regions of the computational domain (as is often the case in NR, where one needs to resolve astrophysical phenomena over different length scales), since due to the Courant–Friedrichs–Lewy (CFL) condition, higher spatial resolution also increases the number of time-steps (and hence, the total number of communication phases) required for a stable evolution.

In the first part of this thesis, we consider a spacetime discretization for solving time-dependent PDEs, which has the potential to significantly reduce the communication overhead, compared to a time-stepping based approach. In contrast to the method of lines approach, where one considers a discretization first in space, and then in time, in a spacetime method, one simultaneously discretizes the evolution equation(s) in space and time. In the context of numerical relativity, this corresponds to decomposing spacetime into spacetime volume elements instead of spacelike hypersurfaces, and computing the solution in each spacetime volume element, instead of on each spatial hypersurface.

Such a discretization offers two main advantages. First, it allows for a more accurate, higher order method in both space and time, in each spacetime element. This is particularly useful in situations where one requires highly accurate interpolations in both space and time; e.g., for computing geodesics in numerical spacetimes [15, 16]. Second, if each spacetime element is designed to have null or spacelike boundaries, then each element can be computed independently of its neighbours, and would only need initial data from elements in its past. Further, if one chooses to compute the solution using an implicit solver, one could take much larger time steps, compared to an explicit time-stepping scheme. Together, a spacetime method could significantly reduce the amount of communication required per time-step, and hence, might scale much more efficiently than conventional time-stepping based methods, as was shown by Jayasinghe *et al.* in [17] for a one dimensional fluid flow

problem.

A spacetime method also presents unique advantages for studying spacetimes near black hole singularities, perhaps due to the fact that they are a more natural choice for GR than a 3+1 decomposition, which introduces an artificial time coordinate. In a standard $3+1$ scheme, one needs to choose suitable gauge conditions (specifically, a time coordinate) to ensure stable evolutions. These gauge conditions, however, are designed to avoid singularities, which makes it difficult to numerically evolve the spacetime region near the singularity. In contrast, in a spacetime method, one does not need to make a gauge choice related to a particular foliation, and hence, could potentially allow one to study spacetime regions closer to the singularity, e.g., by investigating the geometry and evolution trapped regions in black hole spacetimes, as was done in [18, 19].

In Chapter 2, we investigate a spacetime element method for spherically symmetric spacetimes in numerical relativity. We describe a spacetime decomposition based on spacetime volume elements with null boundaries (which minimizes the amount of communication required during evolution between spacetime elements), and use a pseudospectral collocation method to compute the solution in each element (that allows for *hp* adaptivity in both space and time). We investigate the stability, accuracy, and convergence of our method for evolutions of Schwarzschild spacetime and a self-gravitating scalar wave in spherical symmetry.

In the second part of the thesis, we change our focus towards the problem of using numerical relativity simulations to test GR using GW observations. GW observations of compact binary mergers, primarily binary black holes (e.g., [20, 21, 22]), have made it possible to test general relativity (GR) in the strong-field, high velocity regime where GR is most likely to break down (see [23, 24, 25] for results of such tests carried out by the LIGO-Virgo collaboration). However, these tests are all null tests of one sort or another, and one would ideally want to compare the predictions of GR for the coalescence of compact binaries with the predictions of a suite of well-motivated alternative theories (in particular, [26] discusses some of the problems encountered with certain null tests). To carry out such comparisons, one needs to construct high-accuracy waveform models in alternative theories, just as have been constructed in GR. At present, constraints on alternative theories using binary black hole observations have been restricted to using model waveforms constructed with only low-order post-Newtonian (PN) calculations in the alternative theories [27, 28].

Numerical relativity simulations of the late inspiral and merger in alternative theories will be a key ingredient in constructing such waveform models, just as in GR. However, such simulations come with several challenges. Many of these modified theories either do not have a *known* well-posed initial value formulation (making them unsuitable for numerical

evolution) or lack a construction of constraint-satisfying initial data for compact binaries. While significant progress has been made towards finding a well-posed formulation for Einstein-scalar-Gauss-Bonnet, Lovelock, and Horndeski theories at weak coupling [29, 30] and their subsequent numerical evolution [31, 32, 33], most approaches to simulating binary black holes in modified theories of gravity depend on an order reduction method [34, 35, 36, 37, 38]. Such approaches compute the effects of modified theories as perturbations to the GR solution, which leads to a secular drift between the true solution and the perturbative solution [34, 36], though there are proposals for methods to remove this drift [39]. There are also approaches that modify the equations to make the theories well-posed [40], but not yet any evolutions of binary black holes with such approaches.

For theories that do have a known well-posed initial value formulation, evolutions of binary black hole mergers have been carried out using approximate initial data. Examples include a study [41] in Einstein-Maxwell-dilaton theory [42] and evolutions in scalar-tensor theories of gravity [43, 44] where, in the absence of externally imposed scalar field dynamics, binary black holes in scalar-tensor theory have the same dynamics as those in vacuum GR.

Here we consider charged binary black holes in Einstein-Maxwell theory. This provides a well-posed framework that mimics some of the features of binary black hole mergers in modified theories. Additionally, various modified theories besides Einstein-Maxwell-dilaton theory also contain vector fields with a Maxwell-like kinetic term (see, e.g., [45]), so this is a first step to performing simulations in those theories. The specific features of Einstein-Maxwell theory that mimic some of the effects seen in modified theories are modified or additional PN terms in the dynamics of the binary (see, e.g., [46]) and differences in the spectrum of quasinormal modes for the final black hole (see, e.g., [47, 48, 49]). Both of these effects are directly encoded in the binary's GW signal. In particular, charged binary black holes with unequal charge-to-mass ratios emit dipole radiation (see, e.g., [46]), a common feature in several modified theories of gravity, e.g., scalar Gauss-Bonnet (sGB) gravity [50] and scalar-tensor theories of gravity [51]. Binary black holes emit dipole radiation due to a charge in sGB gravity, as well, though there it is a scalar charge, as opposed to the U(1) charge we consider here. Binary black holes in scalar-tensor theories do not emit dipole radiation, but systems with matter will in general emit scalar dipole radiation in those theories. Nevertheless, the leading PN effect of the dipole radiation on the binary's dynamics will have the same frequency dependence in all cases, viz., a $-1$PN order contribution to the orbital phasing and thus to the phase of the GW signal (in the case where the dipole radiation can be treated as a perturbation to the dominant quadrupole radiation—see, e.g., [46]).

From an observational perspective, the LIGO-Virgo analyses (e.g., [23, 24, 25]) currently test for the presence of such an additional $-1$PN term in the phase. In the absence of

dipole radiation (which is the case for charged binary black holes with equal charge-to-mass ratio and the same sign of charge) the deviations from vacuum GR will only occur at 1PN order and above (since the 0PN modifications are degenerate with a rescaling of the binary's masses, as discussed in, e.g., [52]). This is similar to some modified theories, e.g., dynamical Chern-Simons theory, where the deviations from GR start at 2PN [53]. Many of the other LIGO-Virgo tests of general relativity check (explicitly or implicitly) for such deviations in higher-order PN coefficients. Additionally, a recent analysis [49] checks for the presence of charge in the ringdown waveforms, but finds that one can only place very weak constraints using the ringdown phase alone due to correlations between the charge and spin parameters.

Charged binary black hole waveforms, therefore, provide a proxy for BBH waveforms from modified theories of GR that would allow us to test the sensitivity of current LIGO-Virgo tests of GR to completely consistent, parameterized deviations from GR (see [54] for an initial study using phenomenological waveforms). Since the charge can be varied freely up to the extremal limit, this allows for significant deviations from vacuum GR. Further, one can use the waveforms from numerical simulations of charged binary black holes to create a waveform model that one can use to analyze gravitational wave data. Such a waveform model would likely also have significant input from PN calculations [46, 55] and black hole perturbation theory computations of quasinormal modes [47, 48, 49], and possibly also from black hole perturbation theory/self-force calculations of waveforms in the extreme mass-ratio limit (see [56, 57, 58] for work in this direction involving charge). Such a model would allow one to constrain the charges of observed black holes. Such an analysis has already been carried out for low-mass, inspiral-dominated signals in [59] using a simple waveform model created by combining a vacuum GR model with the known, still relatively low-order PN contributions from the charges from [46]. There is also a study of GW150914 using numerical relativity waveforms of charged binary black holes and simple data analysis arguments in [60] (see also further data analysis calculations with these waveforms in [61]). A full waveform model tuned to numerical relativity simulations would also allow one to constrain the charges of high-mass binaries, as well as firming up the constraints obtained with the simple waveform model presented in [59]. As a first step towards constructing such waveform models, in Chapter 3, we construct initial conditions for spinning, charged binary black holes in orbit. We generate excision based initial data for both highly charged and highly spinning binaries using the pseudospectral initial data solver SGRID [62, 63], and in Chapter 4, we discuss our exploratory evolutions of the initial data in some cases with both the BAM [13] and HAD [64] evolution codes.

In the third and final part of this thesis, we again switch our focus, but this time, to understand a problem that is at the foundation of formal verification methods [65], i.e., the

Boolean Satisfiability (SAT) problem. Formal methods, that aim to prove the correctness of a design under formal mathematical specifications, have been very successful towards improving the robustness (e.g., check for hardware and software errors) critical numerical software; e.g., in nuclear physics and aeronautics [66, 67, 68].

While formal verification methods have yet not found applications in computational relativity, there are several problems where they could be potentially useful. For example, formal methods can be used to computationally check for the existence of a solution. In the context of numerical relativity, such a problem arises routinely when looking for a solution to a set of nonlinear algebraic equations. Consider, e.g., the con2prim problem [69] in general relativistic magnetohydrodynamic (GRMHD) simulations. Numerical codes for GRMHD simulations use conserved variables such as baryon number density ($D$), energy ($\tau$), and momentum density ($S_i$) for the evolution. However, at each step of the computation, for a given equation of state, one needs to recover the the primitive variables such as density ($\rho$), pressure ($p$) and matter velocity ($v_i$) in order to compute the stress-energy tensor and numerical flux terms for fluid and spacetime evolution. This recovery, however, is non-trivial, since the map between the conserved variables and the primitive variables is nonlinear. Concretely,

$$D = \rho W, \qquad \tau = \rho h W^2 - p - D, \qquad S_i = \rho W^2 h v_i, \tag{1.1}$$

where $W$ is the local Lorentz factor. The robustness, as well as efficiency of this recovery is crucial for the reliability of such numerical simulations. However, it has been shown that the various schemes (all of which use some variant of a root finding algorithm) that have been proposed to recover the primitive variables from the conserved variables, fail in some cases [69]. The failure of a root finding scheme, could be, e.g., due to the evolved variables being unphysical, for which no solution to the set of equations in (1.1) exists. Thus, one would ideally like to guarantee the existence of a solution before the (often computationally expensive) root finding algorithm is invoked to find the solution. Since Eq. (1.1) can be encoded as first-order logic formulas over the real numbers, one could use a SAT-based theorem prover such as Z3 [70], or dReal [71], to check the existence of the solution to Eq. (1.1). SAT solvers, therefore, have the potential to improve the overall robustness of the evolution scheme in GRMHD simulations, e.g., those involving binary neutron star mergers.

Despite their success and utility in several areas of numerical computing, the efficiency of formal methods, in practice, remain poorly understood [72]. At their core, formal methods solve the Boolean satisfiability problem [73]. The SAT problem can be described as follows. Given a Boolean formula (instance) $F(x_1, x_2, ..., x_n)$ with Boolean literals $(x_1, x_2, ..., x_n)$ in conjunctive normal form (i.e., as a conjunction of one or more clauses, where a clause is

is a disjunction of literals), the Boolean satisfiability problem asks whether there exists an assignment to the variables $(x_1, x_2, ..., x_n)$ such that the formula $F(x_1, x_2, ..., x_n)$ evaluates to true under that assignment. If there exists such an assignment, the formula $F$ is said to be satisfiable. If there exists no such assignment, $F$ is said to be unsatisfiable. For example, the Boolean formula

$$(x_1 \wedge \bar{x}_1 \wedge x_2) \vee (\bar{x}_3 \wedge x_3), \tag{1.2}$$

is not satisfiable for any possible values of $x_1, x_2$ and $x_3$. A SAT solver, in this case, would give a proof of unsatisfiability, whereas, if there exists assignment(s) for which Eq. (1.2) evaluates to true, a SAT solver would output one such assignment.

From a theoretical point of view, the SAT problem is computationally intractable, i.e., it can be proven that *any* algorithm for solving SAT would, in the worst case, take exponential ($2^n$) time to solve on instances with $n$ variables [74, 75]. Surprisingly, modern implementations of SAT solvers based on conflict-driven clause learning (CDCL) [76, 77, 78] routinely solve real world (e.g, those obtained from hardware and software testing, analysis, and verification applications) instances with tens of thousands of variables with much higher efficiency, but at the same time, perform very poorly on smaller randomly generated or cryptographic (i.e. those obtained from verification/analysis of cryptographic applications) instances. Thus, a key open problem in SAT research is to understand what makes certain SAT instances *easier* or *harder*[1] for a (CDCL) SAT solver to solve, than others?

As for why SAT solvers are even able to efficiently solve large real world SAT instances of a computationally intractable problem, it has been argued that theoretically, the SAT algorithm is expected to take exponential time (in the size of the input) only in the worst case scenario, whereas, in practice we encounter real world instances that may not be as hard as an instance representing the worst case scenario. Due to the limitations of such a worst-case complexity analysis for real world SAT instances, several previous studies [79, 80, 81, 82, 83, 84, 85] over the past two decades, have worked towards building a richer (parameterized) computational complexity model for describing the hardness of SAT instances. The basic idea behind such an approach is based on the assumption that there exists, preferably a small set of parameters characterizing a SAT instance, that can

[1]There could be different approaches to measure the hardness of a SAT instance. From an applied standpoint, one could use the time required for a SAT solver to solve a particular SAT instance as a proxy for the hardness of the formula. In a theoretical setting, the hardness of a particular instance can be related to the length of the proof required to show that a formula is unsatisfiable. For a CDCL SAT solver, which, in a certain sense, iteratively constructs a proof of unsatisfiability for a given SAT instance, the two notions of hardness can be assumed to be equivalent to each other.

distinguish between easy and hard instances, such that, for "good" values of these parameters, the SAT instance will be easy for a SAT solver, and conversely, for "bad" values of these parameters, the SAT solver will take exponential time to converge to a solution. In Chapter 5, we explore a parameterized complexity model for the Boolean SAT problem, based on the hierarchical community structure of a SAT formula. Specifically, we build an empirical hardness model for SAT instances that predicts the runtime and category (as a measure of hardness) of a SAT instance using parameters characterizing the hierarchical community structure of the SAT formula.

# Chapter 2

# A Spacetime Discretization Method for Computational Relativity

In this chapter, we describe a spacetime method for numerical relativity. While spacetime methods have existed in the literature for a long time [86, 87], most works have either been mainly mathematical, or have been investigated in the context of engineering problems [88, 89, 17]. In relativity, while the idea of finding a solution simultaneously in space and time have been explored in several different contexts (see, e.g., [90, 91, 92, 93, 94]), none of these, or other works, to the best of our knowledge, have investigated a spacetime decomposition method using pseudospectral elements with null or spacelike boundaries.

Given the novelty of this approach, we develop a spacetime method for NR, starting in a lower dimensional setting, specifically, spherically symmetric (that are, from a numerical point of view, effectively 1+1 dimensional) spacetimes. This allows us to use double null coordinates to construct spacetime elements with null boundaries. While such a choice of coordinates is not necessary for a spacetime method in general, it gives a straightforward way to construct spacetime volume elements, and investigate the convergence and stability of this method in a simpler setting. We do not prove the (continuous or discrete) well-posedness of our numerical method; instead, we numerically investigate the stability and convergence our method, starting with the evolution of the linear scalar wave equation in 1+1 dimensions, and then considering the fully nonlinear evolution of a Schwarzschild black hole, and a self-gravitating massless scalar field in spherical symmetry.

This chapter is organized as follows. In Sec. 2.1, we give an overview of our numerical algorithm to implement an evolution scheme based on a spacetime discretization method. In Sec. 2.2, we discuss the numerical evolutions we considered for testing our implementa-

tion, and in Sec. 2.3 we conclude with a discussion.

## 2.1 The computational algorithm

Our main computational algorithm has three main parts: the construction spacetime volume elements using double null coordinates, an asynchronous parallelism model based on futures, and a pseudospectral collocation method to discretize the evolution equations in each element. We describe them in the following sections.

### 2.1.1 Spacetime elements using double null coordinates

We first describe our spacetime decomposition approach specific to spherical symmetry. Our construction closely follows the suggestion presented in [90]. We use double null coordinates $(u, v)$ to construct spacetime volume elements with null boundaries. In spherical symmetry, these null coordinates can be defined as

$$u = t + r(u, v), \qquad v = t - r(u, v), \tag{2.1}$$

where $r(u, v)$ is a priori, an unknown function of $u$ and $v$. In Schwarzschild spacetime, $r(u, v)$ corresponds to the tortoise coordinate

$$r(u, v) \equiv r^* = \eta + 2M \ln \left| \frac{\eta}{2M} - 1 \right|, \tag{2.2}$$

where $\eta = v - u$.

As shown in Fig. 2.1, we decompose the spacetime into spacetime volume elements with element boundaries along constant $u$ and $v$ hypersurfaces, such that each spacetime element has two incoming null boundaries ($u_{\text{in}}$, $v_{\text{in}}$) and two outgoing null boundaries ($u_{\text{out}}$, $v_{\text{out}}$). This guarantees that the solution on the outgoing boundaries is completely determined by the initial conditions on the incoming boundaries. The evolution thus proceeds element by element, where solution on the outgoing boundaries of each element provide initial conditions on the incoming boundaries of element(s) in its future. Consequently, in Fig. 2.1 (A), elements labelled with a lower number provide initial conditions for the computing the solution on elements labelled with higher numbers.

For GR evolutions, we solve Einstein's field equations using an implicit method on each element. The spherically symmetric metric in double null coordinates is given by [95]

$$\mathrm{d}s^2 = -4\, a(u, v)^2\, \mathrm{d}u\mathrm{d}v + r(u, v)^2 \mathrm{d}\Omega^2 \tag{2.3}$$

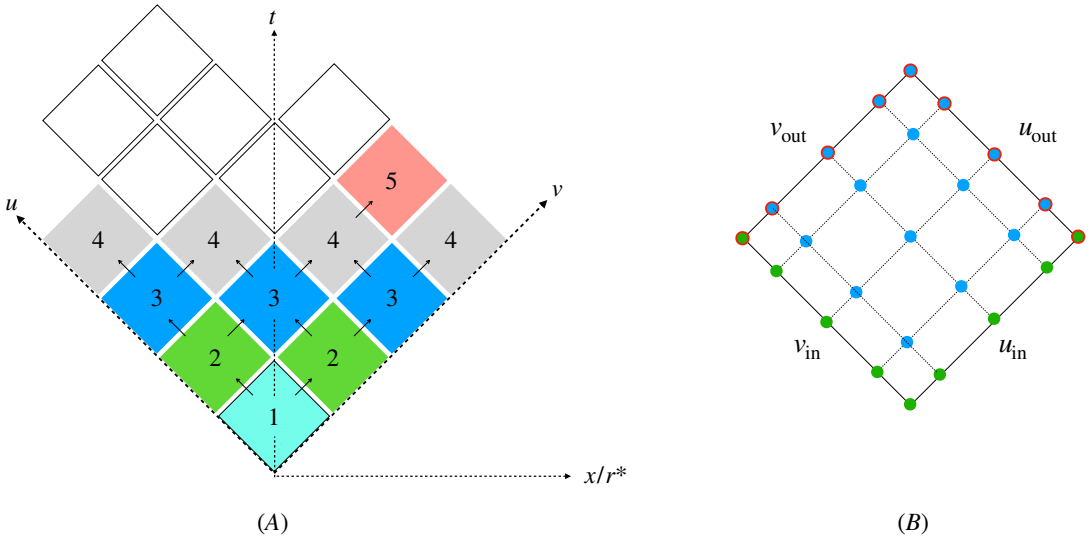


Figure 2.1: Spacetime discretization using spacetime volume elements in 1+1 dimensions or spherical symmetry. (A) On the right, we show the tiling to spacetime using spacetime volume elements with null boundaries. Elements with the same number are causally disconnected from each other and are solved parallel. Initial data on the incoming surfaces is computed by either solving the constraint equations on the boundaries $(u_0, v_0)$, or using the solution on the outgoing boundaries from elements in the past of an element, i.e., those with a lower number. (B) Each spacetime volume element (shown here with 5 collocation points in each direction) has two incoming null boundaries ($u_{\text{in}}$, $v_{\text{in}}$) (marked in green) and two outgoing null boundaries ($u_{\text{out}}$, $v_{\text{out}}$) (marked in blue, with red borders). Given the initial data on $(u_{\text{in}}, v_{\text{in}})$, we do an implicit solve for the entire element to compute the solution on the collocation points marked in blue.

where $\mathrm{d}\Omega^2 = \mathrm{d}\theta^2 + \sin^2\theta\,\mathrm{d}\varphi^2$, and $(\theta,\, \varphi)$ are the standard polar coordinates on the unit sphere. For a spacetime with a scalar field $\Psi(u, v)$, the field equations reduce to (see, e.g., [96, 97])

$$r_{,uu} - 2a^{-1}a_{,u}r_{,u} = -4\pi r\Psi_{,u}^2 \tag{2.4a}$$

$$r_{,vv} - 2a^{-1}a_{,v}r_{,v} = -4\pi r\Psi_{,v}^2, \tag{2.4b}$$

$$a^{-1}a_{,uv} - a^{-2}a_{,u}a_{,v} + r^{-1}r_{,uv} = -4\pi\Psi_{,u}\Psi_{,v}, \tag{2.4c}$$

$$4r_{,uv} + 4r^{-1}\left(r_{,u}r_{,v} + a^2\right) = 0, \tag{2.4d}$$

$$\Psi_{,uv} + r^{-1}\left(r_{,u}\Psi_{,v} + r_{,v}\Psi_{,u}\right) = 0. \tag{2.4e}$$

Here, $\partial_x u = u_{,x}$. The first two equations, i.e., Eq. (2.4a) and (2.4b), henceforth referred to as $C_1$ and $C_2$, constrain the solution $(a, r, \Psi)$ on each null hypersurface, and we use these equations to solve for initial conditions for on the initial incoming boundaries $(u_0, v_0)$. Concretely, given $r(u, v)$ and $\Psi(u, v)$, we solve the first order linear partial differential equation for $a(u, v)$ to get

$$\ln a(u, v) = \int_{u_0}^{u} 4\pi \left( \frac{r}{r_{,u}} \right) \Psi_{,u}^2 \, \mathrm{d}u + C, \tag{2.5}$$

where $C$ is a constant of integration. To construct initial data, we compute the above integral numerically, for a given function $r(u, v)$ and $\Psi(u, v)$ on the initial incoming hypersurface.

We use remaining equations, i.e., Eqs. (2.4c), (2.4d) and (2.4e), to compute the solution in each spacetime volume element, using a nonlinear solver based on the trust region method [98]. As an initial guess to the nonlinear solver, we use a linear superposition of the initial conditions to extrude the initial data at the boundary into the interior of the element.

### 2.1.2 Pseudospectral Collocation Method

We use a pseudospectral collocation method to compute the solution on each element. We use Chebyshev Gauss-Lobatto collocation points (see Fig. 2.1) along both $u$ and $v$ directions and a Chebyshev expansion in both $u$ and $v$ directions. Concretely, the collocation points on an element with arbitrary boundaries, i.e., where $u_{\min} \leq u \leq u_{\max}$ and $v_{\min} \leq v \leq v_{\max}$, is given by

$$u_i = \left[ \frac{u_{\max} - u_{\min}}{2} \right] x_i + \left[ \frac{u_{\max} + u_{\min}}{2} \right], \tag{2.6a}$$

$$v_j = \left[ \frac{v_{\max} - v_{\min}}{2} \right] x_j + \left[ \frac{v_{\max} + v_{\min}}{2} \right], \tag{2.6b}$$

where $x_i$ and $x_j$ are the one dimensional Gauss-Lobatto collocation points defined on the interval $[-1, 1]$, described in in Appendix A. Given a function $f$ evaluated on the above collocation points, we compute its derivative using the derivative operators $(\mathbf{D}_u, \mathbf{D}_v)$ defined as

$$\mathbf{D}_u = I_{ij} \otimes D_{kl}, \qquad \mathbf{D}_v = D_{ij} \otimes I_{kl}, \tag{2.7}$$

where $I_{ij}$ and $D_{ij}$ are the one dimensional identity and derivative operators (see Appendix A), respectively, and $A \otimes B$ corresponds to the Kronecker product between two matrices, i.e.,

$$C_{ikjl} = A_{ij} \otimes B_{kl}. \tag{2.8}$$

Here, we have suppressed the indices on $\mathbf{D}_u$ and $\mathbf{D}_v$ for notational simplicity. Explicitly, the action of the derivative operators on function values $f_{ij} = f(u_i, v_j)$ can be represented as

$$(\partial_u f)_{ij} = \sum_{kl} \mathbf{D}_u^{ijkl} \, f_{kl}, \tag{2.9a}$$

$$(\partial_u f)_m = \sum_{n} \mathbf{D}_u^{mn} \, f_n \equiv \mathbf{D}_u f \tag{2.9b}$$

where, we have introduced abstract indices $m = ij$ and $n = kl$, which allows us to represent the action of derivative operator as a matrix vector product. We also define an integration operator

$$\mathbf{W} = W_{ij} \otimes W_{jk}, \tag{2.10}$$

where $W_{ij}$ corresponds to the one dimensional integration operator, such that $\mathrm{Tr}(\mathbf{W}f)$ is the value of the definite integral of a function $f$ evaluated at the collocation points. Here, $\mathrm{Tr}(A)$ is the trace of a matrix $A$. Further, we define a projection operator $\mathbf{P}$ and its inverse $\bar{\mathbf{P}}$, to go between the grid point values ($f_{ij}$) and the expansion coefficients ($c_{pq}$) of a function $f$ such that

$$c_{pq} = \mathbf{P} f_{ij}, \qquad f_{ij} = \bar{\mathbf{P}} c_{pq}. \tag{2.11}$$

where $f_{ij}$ and $c_{pq}$ are related by the equation

$$f_{ij} = \sum_{mn} c_{mn} \, T^m(x_i) T^n(x_j). \tag{2.12}$$

Here, $T^p(x)$ are the Chebyshev polynomials

$$T^p(x) = \cos(p \, \cos^{-1} x). \tag{2.13}$$

of order $p$. We compute $P$ as

$$\mathbf{P} = I_{ij} \otimes P_{kl} + P_{ij} \otimes I_{kl}. \tag{2.14}$$

Here, $P_{ij}$ is the one dimensional projection operator given by $P_{ij} = T^i(x_j) \, w_j$, where $w_j$ are the one dimensional integration weights corresponding to the Gauss Lobatto collocation points given in Appendix A.

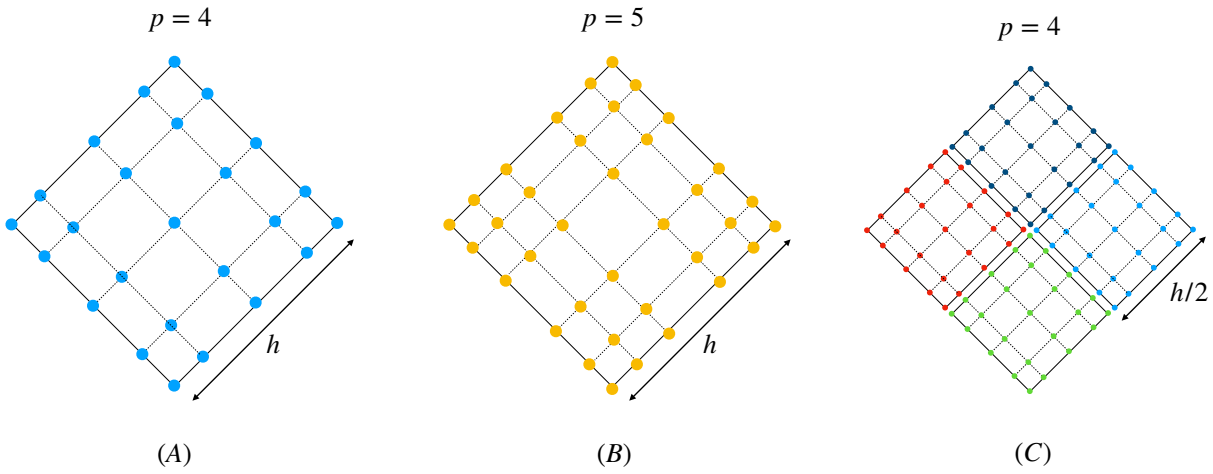


Figure 2.2: An example showing $p$ and $h$ refinement of a spacetime element as implemented in our numerical scheme. (A) A single spacetime element. (B) The spacetime element in (A) after $p$ refinement, where the order of the element has been increased by 1. (C) The spacetime element in (A) after $h$ refinement, where the spectral order in each element remains the same, but the size of each element decreases from $h$ to $h/2$.

To increase the resolution of the computational grid, we consider two kinds of refinement, i.e., $h$ and $p$ refinement. For $p$ refinement we increase the number of points ($N_p$) (equivalently, the spectral order $p$) in each element. For $h$ refinement, we increase the number of elements ($N_h$) in the same computational domain, by dividing a parent element into four smaller, equal sized child elements. We shown an example of these two kinds of refinement for a single spacetime element in Fig. 2.2. In our current implementation, we do not use locally adaptive mesh refinement, but use a global refinement strategy, where all elements are refined uniformly across the entire computational grid.

We now discuss the convergence of our method with increasing resolution. In a pseudospectral element scheme, the discretization error in each element of order $p = N_p - 1$ and size $h$, should scale approximately as

$$\mathcal{E} \sim \mathcal{O}\left(h^{p+1}\right) \tag{2.15}$$

Thus, for $p$ refinement, we expect the error to convergence exponentially, whereas for $h$ refinement, where each element is divided into 4 elements with size $h/2$, we expect the

error to drop geometrically, i.e.,

$$\mathcal{Q}_h = \frac{\mathcal{E}_h}{\mathcal{E}_{h/2}} \sim \frac{\mathcal{O}\left(h^{p+1}\right)}{\mathcal{O}\left(\left[\frac{h}{2}\right]^{p+1}\right)} \sim 2^{p+1}. \tag{2.16}$$

Equivalently, we expect the ratio $Q_h$ to converge to $2^{p+1} = 2^{N_p}$ with $h$ refinement.

### 2.1.3 Asynchronous parallelism model

Since each spacetime element has null incoming (and outgoing) boundaries, in Fig. 2.1, elements labelled with the same number are causally disconnected from each other, and hence, can be solved in parallel. We implement parallelism by defining the elements as futures, a standard abstraction in asynchronous programming. In asynchronous computing, a future is a place-holder object for a value that may not yet exist. When the object is computed and exists, the future makes its value available to subsequent processes, which frees up computational resources for those processes that do not depend on its value and can be computed independently. This allows us to translate the causal dependency between spacetime elements to a computational dependency graph that can be distributed asynchronously across several processes.

Concretely, the computation proceeds by calling three main routines: `setUVboundary`, `computeSTelement`, and `extractUVboundary`. These set initial conditions on $(u_{\rm in},\, v_{\rm in})$, compute the solution on the element, and extract the computed solution at $(u_{\rm out},\, v_{\rm out})$ for each spacetime element, respectively. Thus, the routine `extractUVboundary` depends on the result of `computeSTelement`, which in turn, depends on the result of `setUVboundary`. The routine `setUVboundary`, either depends on the the output of `extractUVboundary` from elements in the past, or computes initial data on the incoming hypersurfaces by solving constraint equations on the null hypersurfaces (for elements at the boundary of the domain). In our algorithm, each of these functions accept a future of the computational result they require, and return a future to the computation they perform. Hence, the computation is distributed at the level of tasks that are processed asynchronously, the order of which depend the casual dependency of the tasks.

## 2.2 Numerical Tests

We now discuss the convergence and stability of our numerical implementation for the evolution of a Schwarzschild black hole and a self-gravitating scalar field, in spherical

symmetry. Before discussing fully nonlinear evolutions of GR spacetimes, we consider the evolution of a massless scalar wave in 1+1 dimensions. This allows us to test the numerical stability of our code without the complexities arising from the presence of nonlinearity, spacetime curvature, or coordinate singularities we encounter in the spherically symmetric case.

### 2.2.1 Scalar wave on 1+1D Minkowski

For a scalar field $\Psi$, the 1+1 dimensional wave equation in Minkowski spacetime in $(t, x)$ coordinates is given by

$$-\Psi_{,tt} + \Psi_{,xx} = 0, \tag{2.17}$$

which, under a coordinate transformation to double null coordinates $(u = t + x, v = t - x)$ takes the simple form

$$\Psi_{,uv} = 0. \tag{2.18}$$

Note that even in this simple case, it is challenging to establish the well-posedness of a double null evolution scheme using energy estimates. The main issue is finding an appropriate definition of an energy norm that bounds the energy of the scalar field in both $u$ and $v$ directions; see, e.g., Sec. 2.1 in [99]. Due to this reason, and the fact that a double null evolution scheme is just one of many approaches to constructing a spacetime method, we refrain from analyzing the well-posedness of our numerical scheme.

For the evolution of scalar wave in 1+1 dimensions, we can freely specify initial conditions. Thus, for initial conditions, we set

$$\Psi(u_0, v) = \sin(\pi v) \exp\left[-\frac{v^2}{\sigma^2}\right], \quad \Psi(u, v_0) = \sin(\pi u) \exp\left[-\frac{u^2}{\sigma^2}\right], \tag{2.19}$$

where $\sigma$ is a free parameter that determines the width (equivalently, the energy) of the incoming waves. In Fig. 2.3, we show the numerical solution (and its expansion coefficients) for the above initial conditions with $\sigma = 0.5$, on a computational domain where $u, v \in [-1, 1]$. Since $u$ and $v$ are the characteristic (null) directions, the evolution equations advect the initial conditions at the incoming boundaries along $u$ and $v$, as shown in Fig. 2.3.

To compute the error in the numerical solution, we numerically integrate the difference between the computed and the analytic solution on each spacetime element, and take the $L_2$ norm of the integrated error over all elements. For the initial conditions given by Eq. (2.19), the analytic solution is of the form

$$\Psi(u, v) = \sin(\pi v) \exp\left[-\frac{v^2}{\sigma^2}\right] + \sin(\pi u) \exp\left[-\frac{u^2}{\sigma^2}\right], \tag{2.20}$$

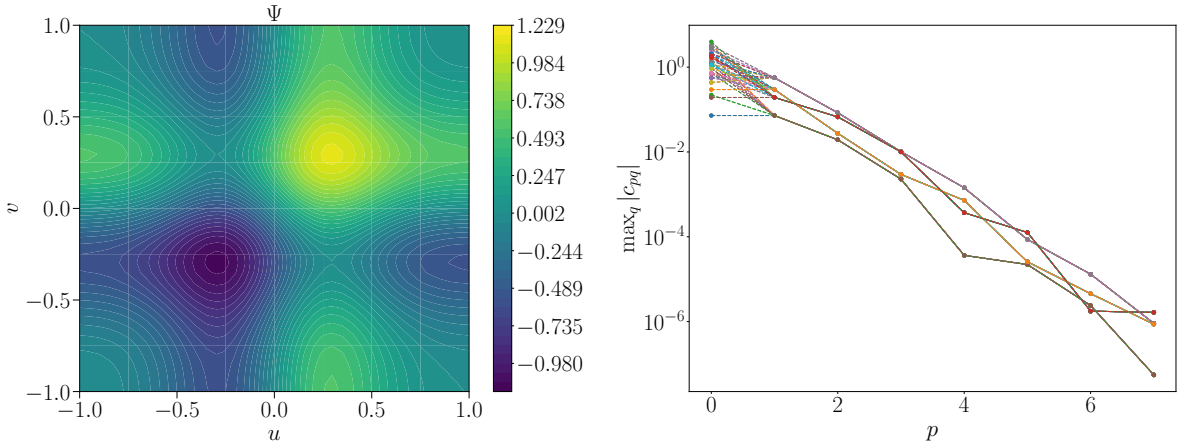


Figure 2.3: (Left) Solution to the scalar wave equation in 1+1 dimensions for $\sigma = 0.5$, computed using $N_p = N_h = 8$. The time coordinate $t = v + u$ increases diagonally from $u = v = -1$ to $u = v = 1$. (Right) Exponential decay of the expansion coefficients ($c_{pq}$) of $\Psi$ with polynomial order $p$.

which is just the linear superposition of the initial conditions in Eq. (2.19). In Fig. 2.4, we show the convergence of this error with $p$ and $h$ refinement for different values of $\sigma$. We observe that for $p$ refinement, the error falls off exponentially with increasing $p$, until it saturates around $\sim 10^{-10}$. Further, the error in the solution for different values of $\sigma$ fall off at different rates. This is expected since a pseudospectral method requires a higher number of points to resolve sharper peaks (corresponding to lower values of $\sigma$) in the numerical solution. For $h$ refinement, we set $N_p = 4$ in each element. We find that the ratio $Q_h$ eventually converges to the expected value of $2^3 = 8$ with increasing $N_h$. These results suggest that our method converges, and is stable for the wave equation in 1+1 dimensions.

Having established convergence and the stability our code in the linear setting, we now consider nonlinear spacetime evolutions in spherical symmetry.

### 2.2.2 Schwarzschild spacetime

We now consider the evolution of a Schwarzschild black hole using a spacetime method. The solution to Eq. (2.4) for a Schwarzschild black hole, i.e., $\Psi = 0$, is well-known [95,

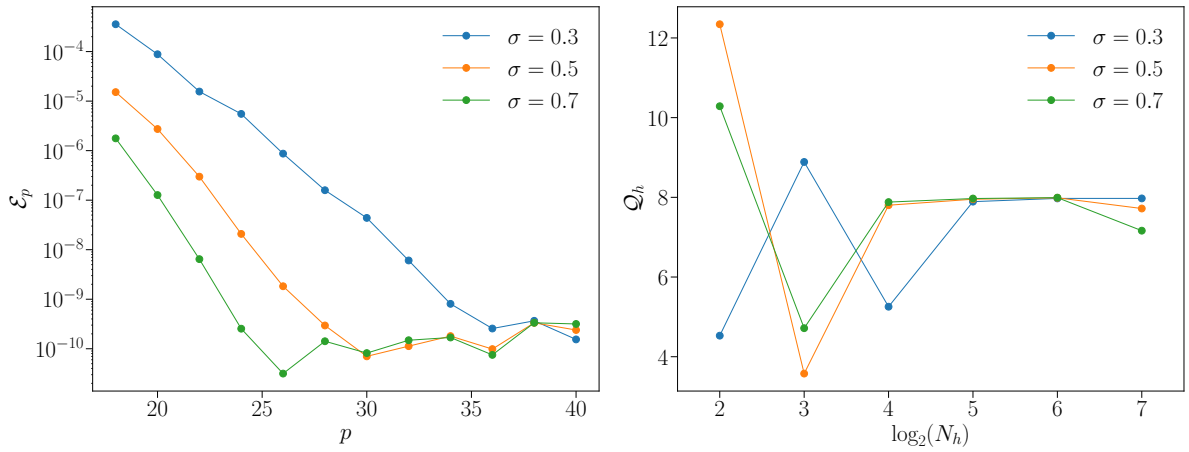


Figure 2.4: Convergence results for the evolution of a scalar wave in 1+1 dimensions for different values of $\sigma$. On the left, we show the convergence of the error $\mathcal{E}_p$ with increasing $p$ in each element. On the right, we plot the convergence of $\mathcal{Q}_h$ with increasing the number of elements.

100]. Concretely, we have

$$r(u,v) = uv + \left[\frac{r}{2M} - 1\right] \exp\left(\frac{r}{2M}\right), \tag{2.21a}$$

$$a(u,v) = -\left[\frac{32M^3}{r} \exp\left(-\frac{r}{2M}\right)\right]^{1/2}, \tag{2.21b}$$

where $M$ corresponds to the mass of the Schwarzschild black hole. We use the Eq. (2.21) to set initial conditions for $a(u,v)$ and $r(u,v)$ on the initial incoming null boundaries. Since $r(u,v)$ is an implicit function of $u$ and $v$ in Eq. (2.21a), we use a numerical root finder to compute $r(u,v)$ as a function of $u$ and $v$ on the initial null hypersurfaces.

With respect to the evolution, we find that our spacetime method is stable, and is able to evolve spacetime regions very close to the singularity. In Fig. 2.5, we show the numerical solution for $r(u,v)$ alongside the logarithm of the norm of the constraint residual vector $\mathcal{C} = [C_1, C_2]$, for a unit mass black hole, on a computational domain where $u \in [-2,1], v \in [1,4]$. Since our computational domain contains a spacetime singularity at $uv = 1$ (shown as the dashed black line in Fig. 2.5 ), we do not compute the solution on those elements which contain grid points where $uv \geq 1$, in order to "excise" the singularity. In elements close to the singularity (e.g., $r_{\min} = 0.404M$), even though the constraint violations are

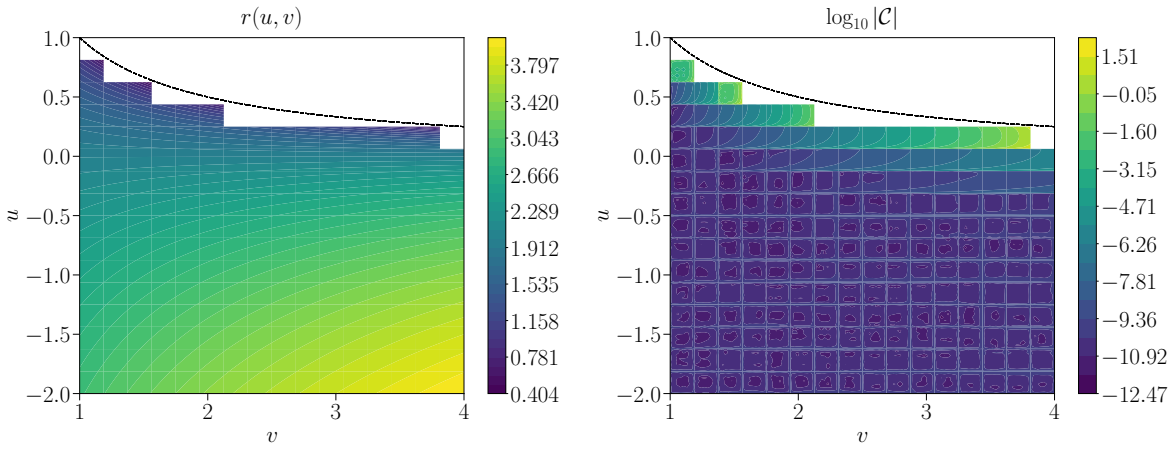


Figure 2.5: The metric component $r(u, v)$ (left) and the logarithm of the norm of the constraint violations (right) for the evolution of a Schwarzschild spacetime, with $N_p = 4, N_h = 16$. The horizon is located at $u = 0$, and the black hole singularity at $(uv = 1)$ (shown as the dashed black line). Here, the time coordinate increases from left to right, and the radial coordinate increases from top to the bottom (as shown by the colour scheme) in each figure.

much larger than in elements far away from the singularity, the constraint violations decay exponentially with $p$ refinement, as shown in Fig. 2.6.

In Fig. 2.6, we show the convergence of the constraint violations with $h$ and $p$ refinement, for different computational domains that represent spacetime regions with different minimum distances $(r_1 = 0.404M, r_2 = 1.241M, r_3 = 2.541M)$ from the black hole singularity. As we see from Fig. 2.6, our implementation shows exponential convergence on all computational domains, even those representing spacetime regions very close to the singularity. Further, we also find the constraint violations to decrease, with a rate approaching the the theoretical estimate ($\sim 8$, since we use $N_p = 4$) with increasing $N_h$. The numerical error, i.e., the difference between the analytic and numerical solution show similar convergence for both $p$ and $h$ refinement. This indicates that our spacetime evolution scheme is stable and convergent, even for nonlinear vacuum spacetimes in spherical symmetry. We therefore test our implementation further, by considering the nonlinear evolution of a non-vacuum spacetime in spherical symmetry.

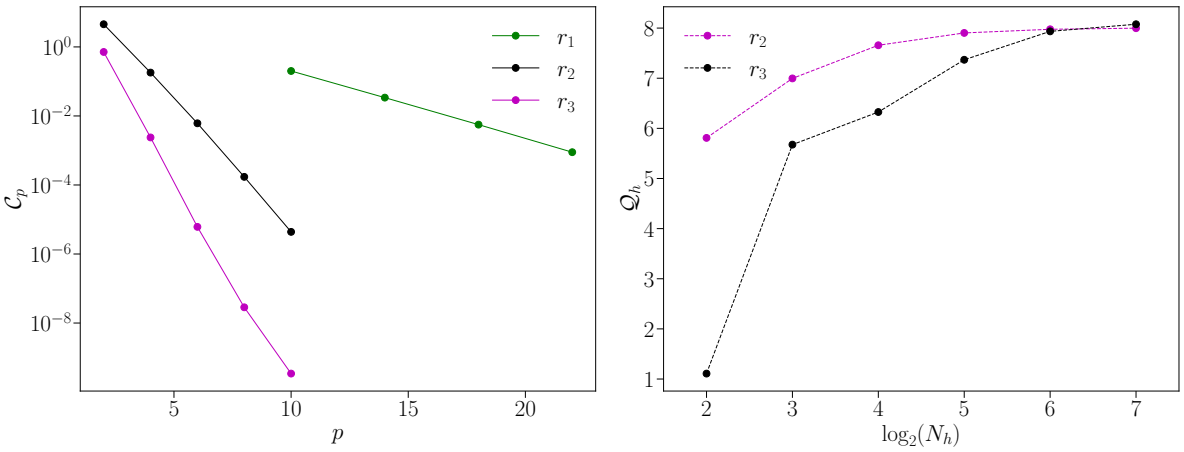


Figure 2.6: (Left) Convergence the constraint violations $\mathcal{C}$ for the evolution of Schwarzschild spacetime in three different computational domains at different distances ($r_1 = 0.404M, r_2 = 1.241M, r_3 = 2.541M$) from the singularity. (Right) Convergence of the ratio ($\mathcal{Q} = \mathcal{C}_h/\mathcal{C}_{h/2}$) with $h$ refinement. Here, we used $N_p = 4$ in each element.

### 2.2.3 Self-gravitating scalar field

We now discuss the evolution of a self-gravitating scalar field in spherical symmetry using a spacetime method. The evolution of a self-gravitating scalar field in spherical symmetry has been studied numerically [101, 102, 96, 90] as well as analytically or semi-analytically [97, 103, 104], for investigating critical collapse phenomena, and the interior of black holes.

Here, we only consider subcritical evolutions, i.e., where the collapsing scalar field does not form a black hole, but instead disperses to infinity. To construct valid initial data on the incoming null hypersurfaces, we set

$$r(u, v) = v - u, \tag{2.22a}$$

$$\Psi(u, v) = \cos(kt - \alpha)\, \frac{\sin kr}{kr}, \tag{2.22b}$$

and compute $a(u, v)$ using Eq. (2.5). Here $k$ and $\alpha$ are constants, and $t = u+v$. Figure. 2.7 shows the solution for $a(u, v)$ for different initial conditions for $\Psi(u, v)$ that correspond to different values of $k$. Here, we consider initial conditions with very low energies; e.g., ($k \sim 0.01$), to ensure that the collapse of the scalar wave does not lead to black hole formation. Since the evolution equations (2.4) are singular on the axis, i.e., $r(u, v) =$

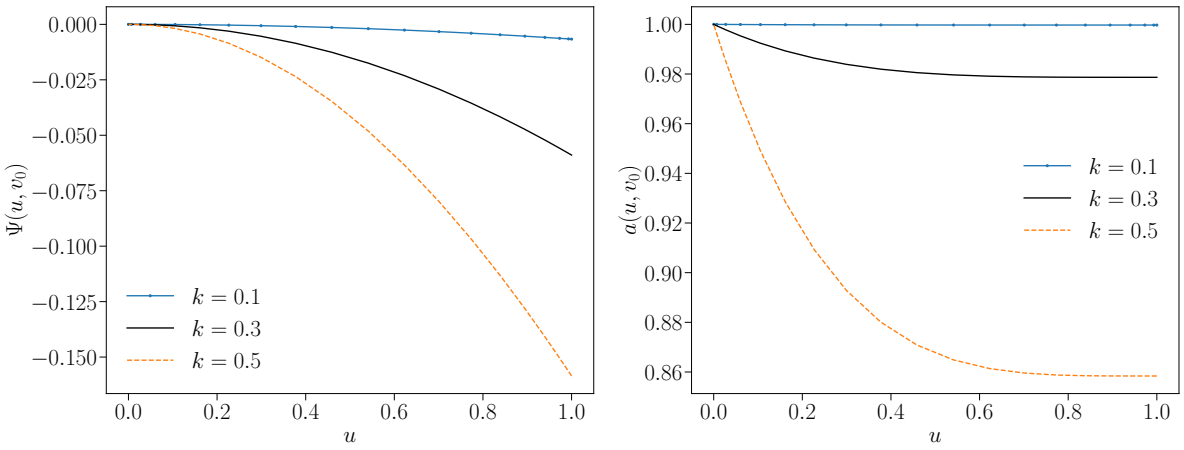


Figure 2.7: Initial conditions for $\Psi(u, v)$ and the corresponding solution to Eq. (2.5) for $a(u, v)$ for different values of $k$.

$0$[1], one needs to appropriately regularize these equations on the axis, to avoid overflows and/or numerical instabilities. We investigated two different approaches to regularize the evolution equations, but were unable to get a convergent numerical solution for either of the approaches. Away from the axis, however, our numerical method was stable, and converged exponentially with $p$ refinement, and at the correct geometric rate for $h$ refinement. In Fig. 2.8, we show the convergence of the constraint violations for various values of $k$, on a computational domain where $u \in [2, 4], v \in [5, 7]$. Therefore, we suspect that the problem with evolutions containing the axis might be related to our approach to regularizing the evolution equations, which we discuss below.

We first considered implicitly enforcing regularity conditions by considering a pseudospectral collocation grid that puts the axis $r = 0$ in between collocation points. We construct such a grid by translating the collocation points by a small amount ($\sim 1e - 5$) such that there exists no collocation point where ($u_i = v_j$) on the computational grid. Since the singularities in the evolution equations are "apparent", i.e., they arise due to our choice of spherical polar coordinates, the expansion coefficients in a pseudospectral method will not diverge, as long as the basis functions are regular at the origin [105]. However, for this approach, we found our implementation to be unstable; i.e., the constraints violations increased with $p$ refinement.

[1]While $r(u, v)$ is an unknown function of the coordinate radius, the location of the axis is always fixed at $u = v$ as a result of spherical symmetry.

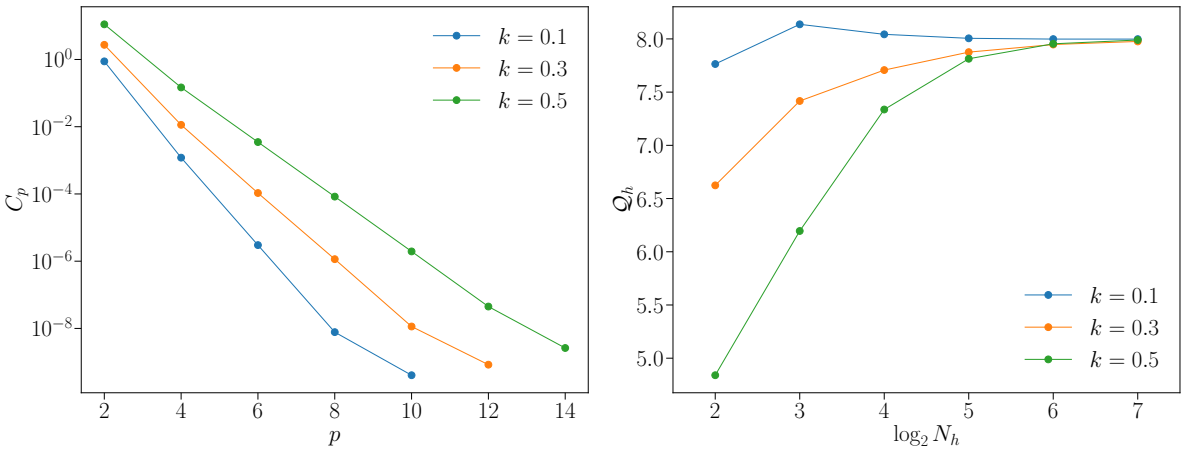


Figure 2.8: $p$ and $h$ convergence the of the constraint violations for the evolution of a self-gravitating scalar field on a computational domain not containing $r = 0$, for different values of the wave number $k$. For $p$ refinement, we used $N_h = 2$, and for $h$ refinement we set $N_p = 4$ in each element.

Since we found that simply avoiding collocation points at $r = 0$ might be insufficient for a stable spacetime evolution scheme, we considered regularizing the evolutions equations by introducing a new evolution variable $s(u, v)$ defined as

$$r(u, v) = s(u, v)\, \eta \tag{2.23}$$

where $\eta = v - u$. We demand $s$ to be an even functions of $\eta$, that is nonzero at the origin. Substituting Eq. (2.23) in the evolution equations (2.4), we get

$$s_{,uv} + \frac{s_{,u} s_{,v}}{s} + \frac{2}{\eta}\left(s_{,u} - s_{,v}\right) - \frac{1}{\eta^2}\left(-s + \frac{a^2}{4s}\right) = 0, \tag{2.24a}$$

$$\frac{a_{,uv}}{a} + \frac{s_{,uv}}{s} + 4\pi \Psi_{,u} \Psi_{,v} + \frac{1}{\eta}\left(\frac{s_{,u} - s_{,v}}{s}\right) = 0, \tag{2.24b}$$

$$\Psi_{,uv} + \frac{1}{\eta}\left(\Psi_{,v} - \Psi_{,u}\right) + \frac{1}{s}\left(s_{,u} \Psi_{,u} + s_{,v} \Psi_{,v}\right) = 0. \tag{2.24c}$$

Since $\eta$ and $\Psi$ are even functions of $\eta$, we have

$$s_{,\eta} = 0 = s_{,u} - s_{,v}, \tag{2.25a}$$

$$\Psi_{,\eta} = 0 = \Psi_{,u} - \Psi_{,v}. \tag{2.25b}$$

Given Eq. (2.25), we observe that the all the singular $(1/\eta)$ terms in Eq. (2.24) go to zero on the origin. To regularize the $(1/\eta^2)$ term in Eq. (2.24a) we use L'Hôspital's rule

$$\lim_{\eta\to 0}\left[\frac{u}{\eta^2}\right] = \frac{u_{,\eta}}{2\eta} = \frac{u_{,\eta\eta}}{2}, \tag{2.26}$$

where $u = -s + a^2/4s$. Note that in applying the L'Hôspital's rule, we have implicitly assumed both $u$ and $u_{,\eta}$ go to zero at $\eta = 0$. Thus, the evolution equations (2.24) on the axis, reduce to

$$s_{,uv} + \frac{s_{,u}s_{,v}}{s} - \frac{a}{2s}\left(\frac{a^2_{,\eta}}{a} + a_{,\eta\eta}\right) = 0, \tag{2.27a}$$

$$\frac{a_{,uv}}{a} + \frac{s_{,uv}}{s} + 4\pi\Psi_{,u}\Psi_{,v} = 0, \tag{2.27b}$$

$$\Psi_{,uv} + \frac{1}{s}\left(s_{,u}\Psi_{,u} + s_{,v}\Psi_{,v}\right) = 0. \tag{2.27c}$$

which are all regular at $\eta = 0$. To compute the solution on an element containing the axis, we thus enforced Eq. (2.27) on collocation points on the axis, and used Eq. (2.24) to constrain the solution on points not on the axis. In this case, we found that our nonlinear solver failed to converge to a residual below $10^{-2}$ even after 1000 iterations.

A nonlinear solver could fail to converge to a solution for several reasons. It could fail, e.g., if one one starts from an initial guess that is too far away from the actual solution. In particular, if the size of the spacetime element is too large, the nonlinear solver might fail to converge for evolutions of highly nonlinear phenomena. However, in our investigations, reducing the element size (which, in for our case, also improves the quality of the initial guess), did not improve the convergence of the nonlinear solver.

To investigate the possibility that our approach for constructing regularized equations leads to an unstable iteration scheme for the nonlinear solver, we considered the evolution of a spherical scalar wave on a Minkowski background, i.e., where $a(u, v) = s(u, v) = 1$, for which Eq. (2.24c) and (2.27c), simplify to

$$\Psi_{,uv} + \frac{1}{\eta}\left(\Psi_{,v} - \Psi_{,u}\right) = 0, \quad \text{and} \quad \Psi_{,uv} = 0, \tag{2.28}$$

Since Eq. (2.28), is linear, the nonlinear solver always converged. However, similar to the self-gravitating scalar field case, we found that the error, i.e., the difference between the numerical and analytic solution [given by Eq. (2.22b)] did not converge below $\sim 10^{-2}$ with increasing resolution. The issue is likely related to the fact that the expansion coefficients

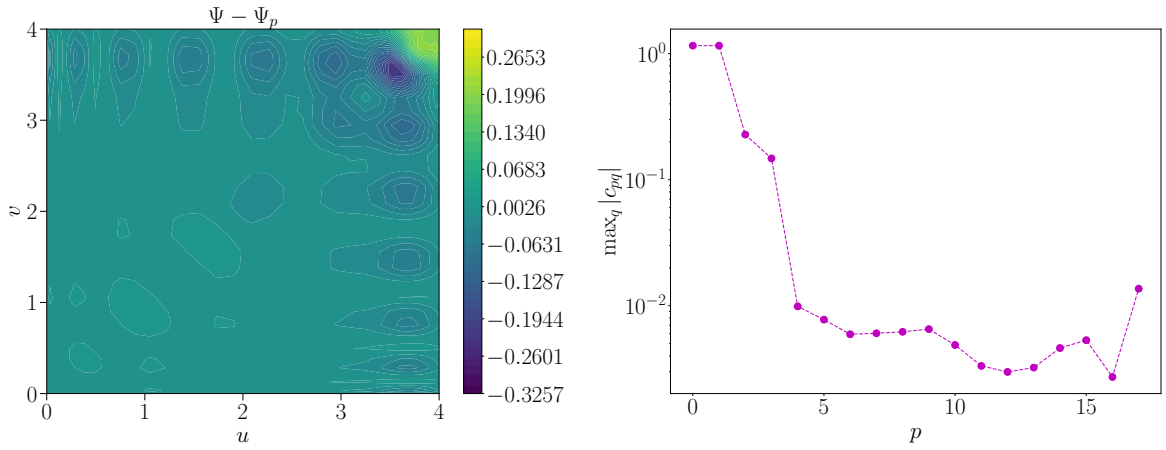


Figure 2.9: (Left) The error $(\Psi - \Psi_p)$ in numerical solution for the evolution of a scalar wave equation on a Minkowski background in spherical symmetry, for $N_p = 18, N_h = 1$. (Right) The maximum of absolute value of the coefficients $c_{pq}$ along $q$ for each $p$, for the numerical solution $\Psi_p$ computed using $N_p = 18$ points.

of the numerical solution for $\Psi$ do decay exponentially with increasing polynomial order, which prevents the numerical solution from converging to the analytic solution, for higher resolutions. In Fig. (2.9), we show the numerical error (which clearly shows the presence of spurious high frequency modes), and the expansion coefficients for the numerical solution for $\Psi$ that not decay beyond $\sim 10^{-3}$.

The saturation of the coefficients near $10^{-3}$ is likely not due to aliasing error, which could be reduced by implementing some form of filtering. As a check, we implemented spectral filtering, where we set the top 1/3 of the modes of the expansion of each component of the solution to zero [106] at every iteration of the nonlinear solver. However, our method still failed to converge for any evolutions containing the axis in the computational domain.

## 2.3 Discussion

In this chapter, we described a spacetime discretization method based on spacetime volume elements for numerical relativity evolutions in spherical symmetry. We used double null coordinates to construct spacetime volume elements with null boundaries, and implemented a pseudospectral method for computing the solution in each spacetime element. We

tested our discretization scheme by first evolving a test scalar wave on a 1+1 dimensional Minkowski spacetime, and then evolving a Schwarzschild black hole and a self-gravitating scalar field in spherical symmetry. We found that our method is stable and converges as expected for both $p$ and $h$ refinement for the evolution of the test scalar field, as well as for Schwarzschild black hole, even very close to the singularity. However, for evolutions of the self-gravitating scalar field, we found that our method converges only in spacetime regions away from the axis of symmetry located at $r = 0$. For evolutions in spacetime regions containing the axis, the nonlinear solver failed converge to a solution.

The failure of the nonlinear solver, we suspect, is due to the numerical inaccuracies arising from the evolution equations involving terms that are singular on the axis. While several authors have used different approaches to handling the coordinate singularity in the double null evolution equations in the past; see, e.g., [101, 102, 96], none of these approaches are directly applicable to our unique numerical evolution scheme. We investigated two different approaches to construct evolution schemes that are regular on the axis but neither of them led to stable, convergent evolutions, even in the simpler case involving the evolution of a spherical scalar field on a Minkowski background, where the evolution equations are linear. While it could be useful to investigate a different approach to regularizing the double null evolution equations in spherical symmetry, it might be more productive—from the point of view of developing a practical algorithm for NR simulations—to construct spacetime elements using more general coordinates, e.g., using unstructured spacetime meshes [107, 108]. This would not only circumvent the problems we faced due to our specific choice of double null coordinates in spherical symmetry, but also allow for more flexibility for adapting a spacetime method to more complicated spacetime geometries.

# Chapter 3

# Initial data for charged black hole binaries

In this chapter, we describe our construction of excision based initial data for both highly charged and highly spinning binaries. Recently, Bozzola and Paschalidis [109] constructed conformally flat, puncture initial data for multiple charged black holes with linear and angular momenta (but with zero magnetic fields) using the conformal transverse traceless approach. Here, we take a different approach to solving for charged binary black hole initial data.

Specifically, we construct conformally curved excision initial data by extending the approach developed by Lovelace *et al.* in [110] to include charge. The approach is based on the Extended Conformal Thin-Sandwich formalism [111, 112] and uses the superposition of two boosted Kerr black holes in Kerr-Schild coordinates (weighted by attenuation functions) for the conformal metric. Compared to the conformal transverse traceless construction, this approach has several advantages (at least in the uncharged case). For example it allows for higher spins [110], less junk radiation [113], and better control over the physics through the boundary conditions at the excision surfaces. For our case, we replace the Kerr black holes by Kerr-Newman black holes and solve for the final electric field by solving for a correction to the superposed electric field (given by a scalar potential) to satisfy the divergence constraint. We use a simple boundary condition for the scalar potential on the excision surfaces that allows us to fix the charges of the black holes. We compute the magnetic field from the superposed vector potentials so that it satisfies the divergence constraint by construction.

This chapter is organized as follows. In Sec. 3.1, we first review the construction

from [110] and then give its extension to the charged case. In Sec. 3.2, we discuss the details of our numerical implementation. We then show examples of our initial data construction in Sec. 3.3, and conclude in Sec. 3.4. We use lowercase Latin letters to denote spatial indices and Greek letters for spacetime indices, and reserve the index $A$ to label the black holes. We use geometric units ($G = c = 1$) and Gaussian units for the electromagnetic field throughout the chapter.

## 3.1 Initial Data Formalism

To compute constraint satisfying initial data for a charged black hole binary on a Cauchy hypersurface $\Sigma$, one needs to solve the Hamiltonian and momentum constraints for the geometry, and the electromagnetic constraint equations for the electric and magnetic field.

With standard decompositions, these constraints constitute a set of coupled, nonlinear, second order differential equations for a given set of freely specifiable variables, and this set has to be supplemented with appropriate boundary conditions. There are several approaches to solving this problem, each with a different decomposition of the gravitational constraint equations and a corresponding unique group of freely specifiable variables (see, e.g., [114, 115] for reviews). Different decompositions can result in different initial data, e.g., with different amounts of junk radiation [114, 116] that could lead to different physical parameters of the binary. We now review one such decomposition, the Extended Conformal Thin Sandwich formalism, which forms the basis of our initial data construction.

### 3.1.1 The XCTS formalism for vacuum GR

The Extended Conformal Thin Sandwich (XCTS) formalism [111, 112] is an alternative approach to the transverse-traceless construction [117] for calculating initial data. In contrast to the transverse-traceless construction, it allows for some degree of control over the time evolution of the initial data. As is standard, this construction begins by splitting the spatial metric $\gamma_{ij}$ into a conformal factor $\psi$ and the conformally related metric $\tilde{\gamma}_{ij}$, and then splitting the extrinsic curvature $K_{ij}$ into its trace $K$ and a traceless part $A_{ij}$, giving

$$\gamma_{ij} = \psi^4 \tilde{\gamma}_{ij}, \tag{3.1a}$$

$$K_{ij} = A_{ij} + \frac{1}{3}\gamma_{ij} K. \tag{3.1b}$$

In the XCTS formalism, we are allowed to freely specify $\{\tilde{\gamma}_{ij}, K\}$ together with their time derivatives $\{\tilde{u}_{ij}, \partial_t K\}$. We then solve for $\{\gamma_{ij}, K_{ij}\}$ in terms of $\psi$, the shift vector $\beta_i$, and the lapse $\alpha$ multiplied by the conformal factor $(\alpha\psi)$, respectively.

For a given choice of freely specifiable variables, the Hamiltonian and momentum constraint equations (see, e.g., [118] for an introduction to the gravitational constraint equations)

$$R + K^2 - K_{ij}K^{ij} = 16\pi\rho, \tag{3.2a}$$

$$\nabla_j \left(K^{ij} - \gamma^{ij}K\right) = 8\pi J^i \tag{3.2b}$$

decompose into a set of coupled elliptic equations for $\psi, \alpha\psi$, and $\beta_i$ given by

$$\tilde{\nabla}_j\tilde{\nabla}^j\psi - \frac{1}{8}\tilde{R}\psi - \frac{1}{12}K^2\psi^5 + \frac{1}{8}\psi^{-7}\tilde{A}^{ij}\tilde{A}_{ij} = -2\pi\psi^5\rho, \tag{3.3a}$$

$$\tilde{\nabla}_j\left[\frac{\psi^7}{2(\alpha\psi)}\left(\tilde{L}\beta\right)^{ij}\right] - \frac{2}{3}\psi^6\tilde{\nabla}^i K - \tilde{\nabla}_j\left[\frac{\psi^7}{2(\alpha\psi)}\tilde{u}^{ij}\right] = 8\pi\psi^{10}J^i, \tag{3.3b}$$

$$\tilde{\nabla}_j\tilde{\nabla}^j(\alpha\psi) - (\alpha\psi)\left[\frac{\tilde{R}}{8} + \frac{5}{12}K^2\psi^4 + \frac{7}{8}\psi^{-8}\tilde{A}^{ij}\tilde{A}_{ij}\right] + \psi^5(\partial_t K - \beta^k\partial_k K) = (\alpha\psi)\left[2\pi\psi^4(\rho + 2\sigma)\right], \tag{3.3c}$$

where

$$(\tilde{L}\beta)_{ij} := \tilde{\nabla}_i\beta_j + \tilde{\nabla}_j\beta_i - \frac{2}{3}\tilde{\gamma}_{ij}\tilde{\nabla}_k\beta^k, \tag{3.4a}$$

$$\tilde{A}^{ij} = \psi^{10}A^{ij} = \frac{\psi^7}{2(\alpha\psi)}\left[(\tilde{L}\beta)^{ij} - \tilde{u}^{ij}\right]. \tag{3.4b}$$

In these equations, the terms decorated with a tilde are associated with the conformal metric. Thus, $\tilde{\nabla}_j$ and $\tilde{R}$ are the covariant derivative and Ricci scalar associated with $\tilde{\gamma}_{ij}$, respectively. We also have electric $(E_i)$ and magnetic $(B_i)$ fields due to the presence of charged black holes, so the expressions for energy density $\rho$, the momentum density $J^i$, and the trace of the stress tensor as measured by an Eulerian observer are given by [119]

$$\rho = \frac{1}{8\pi}\left(E^iE_i + B^iB_i\right) = \sigma, \tag{3.5a}$$

$$J^i = \frac{1}{4\pi}(\mathbf{E}\times\mathbf{B})^i, \tag{3.5b}$$

where

$$(\mathbf{E}\times\mathbf{B})^i = \frac{1}{\sqrt{\gamma}}\,\epsilon_F^{ikl}E_kB_l \tag{3.6}$$

is the curved-space version of the cross product. Here $\gamma$ is the determinant of $\gamma_{ij}$ and $\epsilon_F^{ikl} = \epsilon^F_{ikl}$ is the flat space Levi-Civita symbol taking values in $\{0, \pm 1\}$. Here, and in the rest of the chapter, we raise and lower indices of the physical fields, e.g., $E_i$ and $B_i$, using the physical metric. For the conformally related variables, we use the conformal metric to raise and lower indices. We use boldface letters to denote three-dimensional vector quantities.

Given the XCTS equations (3.3), the next step is to make a choice for the freely specifiable variables $\{\tilde{\gamma}_{ij}, K\}$ and $\{\tilde{u}_{ij}, \partial_t K\}$. For $\tilde{\gamma}_{ij}$ and $K$, we closely follow the construction by Lovelace *et al.* [110], and superpose two boosted, spinning Kerr-Newman black holes in Kerr-Schild coordinates (see Appendix B for the complete expressions) weighted by Gaussian attenuation functions centered around each black hole. Specifically, we set

$$\tilde{\gamma}_{ij} = f_{ij} + \sum_{A=1}^{2} e^{-r_A^2/w_A^2}(\gamma_{ij}^A - f_{ij}), \tag{3.7a}$$

$$K = \sum_{A=1}^{2} e^{-r_A^2/w_A^2} K_A. \tag{3.7b}$$

Here $\gamma_{ij}^A$ and $K_A$ are the spatial metric and the trace of the extrinsic curvature of black hole $A$ where $A \in \{1, 2\}$, and $f_{ij}$ is the flat space spatial metric. Further, $r_A$ and $w_A$ are the coordinate distance from the center of each black hole and the freely specifiable attenuation weight for that black hole, respectively. The free parameters $w_A$ allow one to control the extent of influence of each black hole on the other. In particular, these attenuation functions limit significant deviations from maximal slicing assumption ($K = 0$) and conformal flatness to the regions surrounding each black hole.[1] The choice of $w_A$ affects the amount of junk radiation, and can thus be adjusted to minimize the junk radiation, as mentioned in [113]. We discuss our choices for these weights in Sec. 3.3.

We set the freely specifiable time derivatives, i.e., $\{\tilde{u}_{ij}, \partial_t K\}$, to zero, again as in [110]. For binary black holes in quasicircular orbit, or for eccentric orbits at apoapsis, this is a reasonable approximation, since we can expect the system to be in quasi-equilibrium in an instantaneously corotating frame. For highly boosted head-on collisions, however, this approximation will break down with increasing boost, and we can no longer set these quantities to zero while still obtaining accurate initial data. We will return to this point in Sec. 3.3.

[1] While having asymptotically conformally flat data was shown to be necessary for consistency of the outer boundary conditions (and thus to obtain exponential convergence of the initial data) in [113], the same argument does not apply to our construction, since we do not put the corotation term in the outer boundary condition (see Sec. 3.1.1) as was done in [113].

The final components of our initial data construction for the geometry are the boundary conditions we need to impose on the domain boundaries. Our numerical grid has two boundaries (discussed further in Sec. 3.2.1). The outer boundary is located at spatial infinity ($i_0$) and the inner boundaries are the excision surfaces ($\mathcal{S}_A$) for the two black holes. At spatial infinity, we again follow [110] and set

$$\psi = 1 \quad \text{at } i_0, \tag{3.8a}$$
$$\alpha\psi = 1 \quad \text{at } i_0. \tag{3.8b}$$

These equations ensure that our spatial metric is asymptotically flat. For $\beta^i$, we follow [120] but remove the corotation and expansion terms ($\mathbf{\Omega_0} \times \mathbf{r}$ and $\dot{a}_0 r^i$) from the corresponding expression, and set

$$\beta^k = v_0^k \quad \text{at } i_0. \tag{3.9}$$

Here $v_0^i$ is a velocity parameter used to drive the Arnowitt-Deser-Misner (ADM) linear momentum to zero in our initial data (see Sec. 3.2.3). The corotation and expansion terms diverge at spatial infinity, and thus cause problems in our numerical setup with a compactified grid. We introduced auxiliary variables to handle the diverging terms analytically, but were still unable to get our initial data solver to converge when including these terms in the outer boundary conditions. Instead, we transfer the corotation and expansion terms usually included in the outer boundary condition to the inner boundary condition on $\beta^i$. This transferral leads to equivalent initial data in the conformally flat case, as shown for the corotation term in [121] but is not equivalent in the conformally curved case.[2] Note that this transferral is not completely consistent with our assumption of quasi-equilibrium. Specifically, in the absence of the corotation term at the outer boundary condition for $\beta_i$, we are no longer in a corotating frame, and hence not in quasi-equilibrium. However, we find that our modified boundary conditions for the shift also leads to orbiting black holes, and thus ignore the inconsistency in this present work. Concretely, we set

$$\begin{aligned}\beta^i = \alpha s^i - \Omega_r^k \xi^i{}_{(k)} - [\mathbf{\Omega}_0 \times (\mathbf{r} - \mathbf{r}_{\rm CM})]^i \\ - \dot{a}_0 (\mathbf{r} - \mathbf{r}_{\rm CM})^i \quad \text{on } \mathcal{S}_A.\end{aligned} \tag{3.10}$$

Here, we use the Euclidean cross product. Further, $s^i$ is the outward-pointing normal to the excision surface, $\Omega_r^k$ is a free parameter (similar to $v_0^i$) used to control the magnitude of the spin of each black hole as in, e.g., [110], and $\xi^i{}_{(k)}$ are approximate rotational Killing vectors on $\mathcal{S}_A$. Additionally, $\mathbf{r}$ and $\mathbf{r}_{\rm CM}$ correspond to the coordinate position vector and

[2] The same argument also holds for the expansion term, since it is also a conformal Killing vector in this case.

the position of the Newtonian center of mass of the binary, respectively. Finally, $\mathbf{\Omega}_0$ and $\dot{a}_0$ correspond to the orbital and radial velocity of the binary, which are adjusted to reduce the eccentricity of the binary. Here $\Omega_r^k$ and $\xi^i{}_{(k)}$ are in general different for the two black holes, but we omit the $A$ label on them, for notational simplicity.

We take $\xi^i{}_{(k)}$ to be the rotational Killing vectors in flat space, i.e.,

$$\xi^i{}_{(k)} = \epsilon^F_{ikl} \left(\mathbf{r} - \mathbf{r}_{\rm BH}\right)^l , \tag{3.11}$$

the same choice used to measure black hole spins in BAM [122], where $\mathbf{r}_{\rm BH}$ is the coordinate location of the center of each black hole (again omitting the $A$ label). Additionally, these flat space rotational Killing vectors lead to spin measurements that agree well with PN predictions for nutation [123]. Thus, the more involved approximate Killing vector constructions in [124, 110] may not necessarily lead to better initial data. In particular, it is likely most useful for waveform modelling purposes to have spin measurements that agree well with the PN definitions. However, it would likely be worthwhile to consider the boost-fixed version of the flat space rotational Killing vectors introduced in [123].

For the rest of the inner boundary conditions, we follow [110] and set

$$\tilde{s}^k \partial_k \psi = -\frac{\psi^3}{8\alpha} \tilde{s}^i \tilde{s}^j (\tilde{L}\beta)_{ij} - \frac{\psi}{4} \tilde{h}^{ij} \tilde{\nabla}_i \tilde{s}_j + \frac{1}{6} K \psi^3 \quad \text{on } \mathcal{S}, \tag{3.12a}$$

$$\alpha\psi = 1 + \sum_{A=1}^{2} e^{-r_A^2/w_A^2} (\alpha^A - 1) \quad \text{on } \mathcal{S}, \tag{3.12b}$$

where $\tilde{s}^i$ and $\tilde{h}_{ij}$ are the conformally-rescaled surface normal and the conformal 2-metric on $\mathcal{S} := \mathcal{S}_1 \cup \mathcal{S}_2$, respectively. (Here we just refer to $\mathcal{S}$, since these boundary conditions do not have anything specific to a given excision surface.) Specifically,

$$h_{ij} = \gamma_{ij} - s_i s_j = \psi^4 (\tilde{\gamma}_{ij} - \tilde{s}_i \tilde{s}_j) = \psi^4 \tilde{h}_{ij}. \tag{3.13}$$

This inner boundary condition on the conformal factor ensures that the excision surfaces coincide with the apparent horizons, while the condition on the lapse is a gauge choice that ensures that the time coordinate near each black hole is close to that of the corresponding Kerr-Schild spacetime.

### 3.1.2 Extending to electrovacuum GR

For binary black hole spacetimes with electric charge, we will have nonzero electric and (in general) magnetic fields. These electromagnetic (EM) fields, like the geometric quantities

in the previous section, cannot be freely specified on the Cauchy surface and need to satisfy the EM constraint equations

$$\nabla_i E^i = 4\pi\rho_{\rm EM}, \tag{3.14a}$$

$$\nabla_i B^i = 0. \tag{3.14b}$$

(See [119] for the $3+1$ decomposition of the Einstein-Maxwell equations.) Here $\rho_{\rm EM}$ is the charge density as measured by an Eulerian observer and $\nabla_i$ is the covariant derivative compatible with the physical metric $\gamma_{ij}$. Similar to the XCTS equations, we choose a particular decomposition of these equations, which uniquely determines the degrees of freedom we solve for and the choice of freely specifiable variables.

To solve for the electric field, we start by introducing a correction to the background (superposed) electric field $(E_{\rm sp})^i$ in the form of a gradient of a scalar potential[3] $\phi$, giving

$$E^i = (E_{\rm sp})^i + \nabla^i\phi. \tag{3.15}$$

We then insert Eq. (3.15) in Eq. (3.14a) with $\rho_{\rm EM} = 0$ (since we assume the charge to be contained inside our excision surfaces) to get an elliptic equation for $\phi$

$$\nabla_j\nabla^j\phi = -\nabla_i(E_{\rm sp})^i. \tag{3.16}$$

To solve Eq. (3.14b) for the magnetic field, we use an ansatz that satisfies the magnetic divergence constraint by construction, as described below.

We are free to choose the background field $(E_{\rm sp})^i$ in Eq. (3.15). We set it to be the weighted superposition of the electric field of the two individual black holes.

$$(E_{\rm sp})^i = \sum_{A=1}^{2} e^{-r_A^2/w_A^2} E_A^i, \tag{3.17}$$

and solve for $\phi$ to construct $E^i$ using Eq. (3.15). See Appendix B for expressions for the EM fields of a Kerr-Newman black hole in Kerr-Schild coordinates.

To find a magnetic field configuration that satisfies the constraints, we superpose the magnetic vector potentials $\mathcal{A}_A^i$ of the two black holes in the same manner as we superpose the electric fields

$$(\mathcal{A}_{\rm sp})^i = \sum_{A=1}^{2} e^{-r_A^2/w_A^2} \mathcal{A}_A^i, \tag{3.18}$$

[3] A different method to construct a constraint satisfying electric field would be to superpose the individual electric fields weighted by the determinants of the individual physical 3-metrics as suggested by East [125], which satisfies Eq. (3.14a) by construction. While this is a more straightforward approach, it does not allow one to control the charge on each black hole.

and compute the magnetic field as in [119], giving

$$B^i = \frac{1}{\sqrt{\gamma}} \epsilon_F^{ikl} \partial_k (\mathcal{A}_{\rm sp})_l. \tag{3.19}$$

Since the divergence of a curl is zero, Eq. (3.19) automatically satisfies Eq. (3.14b). Thus, we do not explicitly solve for the magnetic field, though the magnetic field of the final solution is affected by the rest of the solution through the contribution of the conformal factor to $\gamma$.

We want the potential $\phi$ to approach a constant at infinity for our isolated binary, so at the outer boundary we set

$$\phi = \text{const} \quad \text{at } i_0. \tag{3.20}$$

The specification of this constant is a gauge choice and we choose it to be zero. On the inner boundaries, we impose a Neumann boundary condition to control the charge of the black hole. Specifically, we scale the superposed electric field $E_{\rm sp}$ on $\mathcal{S}$ to obtain the desired charge on each black hole. We set

$$s^i \partial_i \phi = \left( \frac{Q_{{\rm d},A}}{Q_{{\rm sp},A}} - 1 \right) s^i (E_{\rm sp})_i \quad \text{on } \mathcal{S}_A. \tag{3.21}$$

In the above equation, $Q_{{\rm d},A}$ is the desired charge on the black hole (i.e., the same charge used to compute the background Kerr-Newman metric for that hole), and $Q_{{\rm sp},A}$ is the charge on each black hole computed using the superposed electric field on each excision surface, i.e.,

$$Q_{{\rm sp},A} = \frac{1}{4\pi} \oint_{\mathcal{S}_A} (E_{\rm sp})^i \sqrt{h}\, dS_i, \tag{3.22}$$

where $h$ is the determinant of $h_{ij}$ [which is given in Eq. (3.13)], and $dS_i$ corresponds to the directed surface area element on the excision surface. To compute the charge for a black hole with the final solved electric field $E^i$, we replace $(E_{\rm sp})^i$ with $E^i$ in Eq. (3.22).

This construction will not work if the desired charge is nonzero and the superposed field leads to zero charge (or a much smaller charge than the desired one). However, this sort of situation seems unlikely to occur in practice, and we have not encountered it in our numerical investigations. Nevertheless, this is a relatively simple construction to fix the charge. There is likely a better way to set boundary conditions on the electric field that is more in line with the isolated horizon boundary conditions used for the geometry. We leave investigating such conditions for future work.

In particular, the obvious requirement on the electric and magnetic fields at the horizon from the requirement that the excision surface be an isolated horizon (in fact, just a non-expanding horizon) does not translate into a condition on the normal derivative of $\phi$. Specifically (see, e.g., [126, 127]) the relation

$$ {}^{(4)}R_{\mu\nu} l^\mu p^\nu = 0 \tag{3.23} $$

is satisfied on the apparent horizon for any $p^\nu$ tangent to the horizon. Here ${}^{(4)}R_{\mu\nu}$ is the 4-dimensional Ricci tensor, and $l^\mu$ is the outward-pointing null normal to the horizon. In our Einstein-Maxwell case, Eq. (3.23) implies $F_{\mu\nu} l^\mu p^\nu = 0$ (see Sec. II C in [126]). Thus, from the expression for $F_{\mu\nu}$ in terms of the electric and magnetic fields (see Sec. II in [119]), we have

$$ [E_i^{\parallel} + (\mathbf{s} \times \mathbf{B})_i]\, p^i = 0. \tag{3.24} $$

Here the cross product is the curved-space one from Eq. (3.6) and $E_i^{\parallel} := E_i - s_i s^j E_j$ is the projection of $E_i$ perpendicular to the unit normal to the horizon, $s^i$. Since the vector $p^i$ in Eq. (3.24) is arbitrary and tangent to the horizon, we get

$$ E_i^{\parallel} = -(\mathbf{s} \times \mathbf{B})_i \quad \text{on } \mathcal{S}_A. \tag{3.25} $$

In Sec. 3.3, we discuss how well this condition is satisfied with our construction.

## 3.2 Numerical Method

To construct initial data, we solve Eqs. (3.3) and (3.16), together with the boundary conditions (3.9), (3.10), (3.12), and (3.21) using the pseudospectral code SGRID [63, 62]. We use a Newton-Raphson scheme together with an iterative generalized minimal residual solver with a block Jacobi preconditioner to solve the linearized equations (see Appendix C for the linearized XCTS equations) during each Newton step (see Chap. 4 in [128] for details of the implementation). In the following sections, we first describe our numerical grid and then discuss how we compute the ADM mass and linear and angular momentum of the initial data as well as the quasilocal mass and spin of the black holes in our initial data solver.

### 3.2.1 Surface Fitting Coordinates

We use the compactified $(A_{\rm Ans}, B_{\rm Ans}, \varphi)$ coordinates introduced by Ansorg [129] to cover all of space outside the two excision regions with two computational domains (see Fig. 3.1).

In each domain $A$, the Cartesian coordinates $(x, y, z)$, in terms of the $(A_{\rm Ans}, B_{\rm Ans}, \varphi)$ coordinates, read

$$x = b\left[\frac{1}{(\mathcal{R}^2+\mathcal{X}^2)^2}+1\right]\frac{\mathcal{X}^2-\mathcal{R}^2}{2} \tag{3.26a}$$

$$y = b\left[\frac{1}{(\mathcal{R}^2+\mathcal{X}^2)^2}-1\right]\mathcal{R}\mathcal{X}\cos\varphi \tag{3.26b}$$

$$z = b\left[\frac{1}{(\mathcal{R}^2+\mathcal{X}^2)^2}-1\right]\mathcal{R}X\sin\varphi \tag{3.26c}$$

where $b$ is the coordinate distance of the centre of the black hole from the origin, $\varphi$ corresponds to the azimuthal angle around the $x$-axis, and

$$\begin{aligned}\mathcal{X} =&(1-A_{\rm Ans})\left\{\mathrm{Re}\left[C_A(B_{\rm Ans},\varphi)\right]-B_{\rm Ans}\,\mathrm{Re}\left[C_A(1,\varphi)\right]\right\}\\ &+B_{\rm Ans}\cos\left(\frac{\pi}{4}A_{\rm Ans}+\left[1-A_{\rm Ans}\right]\arg\left[C_A(1,\varphi)\right]\right)\end{aligned} \tag{3.27a}$$

$$\begin{aligned}\mathcal{R} =&(1-A_{\rm Ans})\left\{\mathrm{Im}\left[C_A(B_{\rm Ans},\varphi)\right]-B_{\rm Ans}\,\mathrm{Im}\left[C_A(1,\varphi)\right]\right\}\\ &+B_{\rm Ans}\sin\left(\frac{\pi}{4}A_{\rm Ans}+\left[1-A_{\rm Ans}\right]\arg\left[C_A(1,\varphi)\right]\right).\end{aligned} \tag{3.27b}$$

Here $C_A$ is a complex function different for positive and negative values of $x$ (the domain with black hole $A$), and is given by

$$C_A(B,\phi) = \sqrt{\tanh\left[\frac{\sigma_A(B,\varphi)+i\pi B_{\rm Ans}}{4}\right]} \tag{3.28}$$

where $\sigma_A(B,\phi)$ is a freely specifiable function that determines the shape of the excision surface. Further, the coordinates $A_{\rm Ans}$ and $B_{\rm Ans}$ take values between 0 and 1, and $A_{\rm Ans}=0$ corresponds to the excision surface $\mathcal{S}_A$ in each computational domain, and spatial infinity $i_0$ corresponds to the point $(A_{\rm Ans}=1, B_{\rm Ans}=0)$ on the grid.

As in [110], we impose boundary conditions on the excision surface such that the excision surface coincides with the apparent horizon of each black hole in the solved binary black hole initial data. We thus set the excision surface around each black hole such that it coincides with the event horizon of the boosted Kerr-Newman black hole used in the superposed metric. We do this by numerically solving for $\sigma_A(B_{\rm Ans},\varphi)$ that appears in Eq. (3.28). Concretely, we place the two black holes on $x=\pm b$, and solve for $\sigma_A$ such that the horizon equation

$$\frac{\|\,\mathbf{r}_{\mathcal{S}}-(\hat{\boldsymbol{\chi}}\cdot\mathbf{r}_{\mathcal{S}})\,\hat{\boldsymbol{\chi}}\,\|^2}{r_+^2+M^2\chi^2}+\frac{(\hat{\boldsymbol{\chi}}\cdot\mathbf{r}_{\mathcal{S}})^2}{r_+^2}=1, \tag{3.29}$$

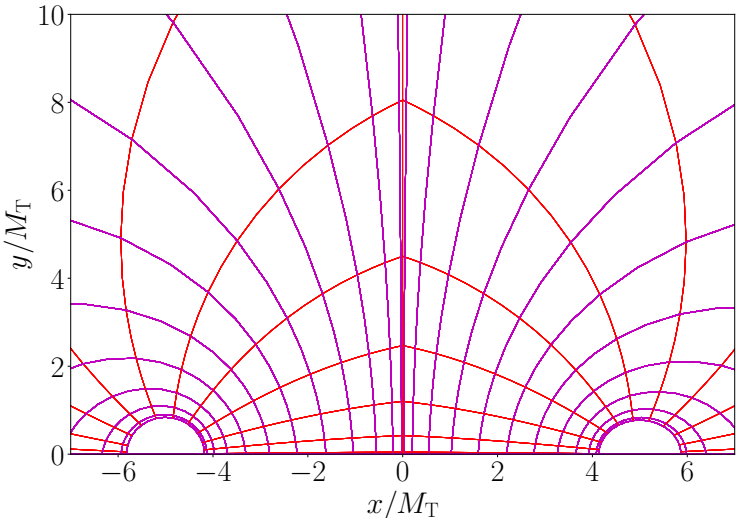


Figure 3.1: The $\phi = 0$ slice in the coordinates we use for the binary black hole configuration `qc-sp7cp5` (see Table 3.1). The black holes are centered at $x = \pm 5M_{\rm T}$, where $M_{\rm T}$ is the total mass of the superposed black holes. Lines of constant $A_{\rm Ans}$ and $B_{\rm Ans}$ are shown using purple and red, respectively. The excision surfaces are ellipsoids located at $A_{\rm Ans} = 0$. The grid is separated into two computational subdomains that meet along the $yz$-plane (seen here only as the line $x = 0$).

is satisfied on each excision surface. Here, $\mathbf{r}_{\mathcal{S}} = (x \pm b, y, z)$ is the coordinate vector pointing from the black hole center to a point on the excision surface (located at $A_{\rm Ans} = 0$). On the excision surface ($A = 0$), the coordinate vector $\mathbf{r}_{\mathcal{S}}$ simplifies to ($\mathbf{r}_{\mathcal{S}} = x \pm b, \rho\cos\varphi, \sin\varphi$) where

$$x = -\frac{b\sin[\sigma_A(B_{\rm Ans},\phi)]}{\cos[B_{\rm Ans}\pi] - \cosh[\sigma_A(B_{\rm Ans},\varphi)]}, \tag{3.30}$$

$$\rho = \frac{b\sin[\sigma_A(B_{\rm Ans},\phi)]}{\cos[B_{\rm Ans}\pi] - \cosh[\sigma_A(B_{\rm Ans},\varphi)]}. \tag{3.31}$$

For a black hole hole with nonzero velocity, we apply the appropriate Lorentz transformation to $\mathbf{r}_{\mathcal{S}}$ to account for the length contraction of the horizon due to the boost. Further, $M$, $\chi$, and $\hat{\boldsymbol{\chi}}$ represent the black hole's mass, the magnitude of its dimensionless spin, and the unit vector along the spin axis, respectively. Additionally, $r_+$ is the radius of the outer

horizon of a Kerr-Newman black hole given by

$$r_+ = M + M\sqrt{1-\chi^2-\mathcal{Q}^2}, \tag{3.32}$$

where $\mathcal{Q} := Q/M$, and $Q$ is the charge of the Kerr-Newman black hole.

Finally, at the interface between the two domains and on the $x$-axis, we impose regularity conditions; see [62, 128]. For the spectral expansions, we use a Fourier basis in the $\phi$ coordinate and Chebyshev bases in both $A_{\rm Ans}$ and $B_{\rm Ans}$ coordinates.

### 3.2.2 Computing diagnostics

In order to characterize our initial datasets and control our initial data parameters, we compute the ADM mass and linear and angular momenta of the initial data. We also compute quasilocal measures of the mass and spin of each individual black hole.

To compute the ADM mass, we follow [130] in obtaining a more numerically accurate expression by writing the original surface integral at infinity as the sum of a volume integral and surface integrals over the excision surfaces and removing the second derivatives of the conformal factor using the Hamiltonian constraint. We correct the expressions from that paper for a flipped pair of indices in the integrand of the surface integral and generalize to the conformally curved case; cf. the original versions of the expressions in [131]. In addition, we also incorporate the source terms arising from the Hamiltonian constraint to obtain

$$\begin{aligned} M_{\rm ADM} = \frac{1}{16\pi}\int_{\mathcal{V}}\left[(1-\psi)\ \tilde{R} + \tilde{\Gamma}^k\ \tilde{\Gamma}^i{}_{ki} - \tilde{\Gamma}^{ikj}\tilde{\Gamma}_{kij} + \psi^{-7}\tilde{A}^{jk}\tilde{A}_{jk} + \psi^5\left(16\pi\rho - \frac{2}{3}K^2\right)\right]\sqrt{\tilde{\gamma}}\ dV \\ + \frac{1}{16\pi}\sum_{A=1}^{2}\oint_{\mathcal{S}_A}\psi^4(\tilde{\Gamma}^k - \tilde{\Gamma}^{ik}{}_{i} - 8\ \tilde{\nabla}^k\psi)\sqrt{\tilde{h}}\ dS_k, \end{aligned} \tag{3.33}$$

where $\tilde{R}$ and $\tilde{\Gamma}^i_{jk}$ are the Ricci scalar and Christoffel symbols computed using the conformal metric and $\tilde{\Gamma}^i := \tilde{\gamma}^{jl}\tilde{\Gamma}^i{}_{jl}$. Additionally, $\mathcal{V}$ is the region outside the excision surfaces and $dV$ is the volume element in flat space.

To compute the ADM linear and angular momentum, we follow [120], adding the rele-

vant source terms due to the presence of the EM fields to get

$$P^i_{\rm ADM} = \frac{1}{8\pi}\sum_{A=1}^{2}\oint_{\mathcal{S}_A} P^{ij}\, dS_j - \frac{1}{8\pi}\int_{\mathcal{V}} G^i\, dV, \tag{3.34a}$$

$$\begin{aligned} J^z_{\rm ADM} = {} & \frac{1}{8\pi}\sum_{A=1}^{2}\oint_{\mathcal{S}_A} (xP^{yj} - yP^{xj})\, dS_j \\ & - \frac{1}{8\pi}\int_{\mathcal{V}} (xG^y - yG^x)\, dV, \end{aligned} \tag{3.34b}$$

where $J^x_{\rm ADM}$ and $J^y_{\rm ADM}$ are obtained by cyclic permutations of $(x, y, z)$ in the above equation, and

$$P^{ij} := \psi^{10}(K^{ij} - K\psi^{-4}\tilde{\gamma}^{ij}), \tag{3.35a}$$

$$G^i := \tilde{\Gamma}^i_{jk}P^{jk} + \tilde{\Gamma}^j_{jk}P^{ik} - 2\tilde{\gamma}_{jk}P^{jk}\tilde{\gamma}^{il}\partial_l(\ln\psi) - 8\pi J^i. \tag{3.35b}$$

As in [120], we apply a rolloff to the volume integrands at large radii in Eqs. (3.34) to reduce the contributions from numerical noise in the regions near infinity where the integrand is small and the volume element is large. Specifically we set

$$G^i_{\rm rolloff} = \begin{cases} G^i & \text{if } r \le R_c \\ (R_c^2/r^2)\; G^i & \text{if } r > R_c, \end{cases} \tag{3.36}$$

where $r$ is the coordinate distance from the origin, and $R_c$ is the roll-off radius. We apply the same roll-off to the volume integrand in Eq. (3.33). We set $R_c = 500M_{\rm T}$, where $M_{\rm T}$ is the sum of the masses of the two superposed Kerr-Newman black holes.

We also compute the quasilocal mass and spin of the black holes in the standard way, through integrals over the excision surfaces, with just a small generalization to the charged case. Specifically, we compute the irreducible mass of the horizon

$$M_{\rm irr} = \sqrt{\frac{\mathcal{H}}{16\pi}}, \tag{3.37}$$

where $\mathcal{H}$ is the area of the horizon. We also compute the angular momentum of the horizon $\mathcal{J}^k$ using the standard isolated horizon integral [132] with the contribution from the EM fields as in [133], giving

$$\mathcal{J}^k = \frac{1}{8\pi}\oint_{\mathcal{S}_{\rm A}} [K_{ij} + 2(\mathcal{A}_{\rm sp})_i E_j]\, \xi^i{}_{(k)}\sqrt{h}\, dS^j, \tag{3.38}$$

where $(\mathcal{A}_{\rm sp})_i$ is given by Eq. (3.18) and $\xi^i{}_{(k)}$ are the flat space Killing vectors defined in Eq. (3.11). The sign of the EM term is opposite the one given in [133], since we found that this gives the correct result for an isolated Kerr-Newman black hole. We presume that this is due to a difference in sign convention, particularly since [109, 61] use the same sign as [133], but have not been able to find the exact source of this difference. We then compute the horizon mass, often known as the Christodoulou-Ruffini mass, $M_{\rm Chr}$ [134], using

$$M_{\rm Chr}^2 = \left(M_{\rm irr} + \frac{Q^2}{4M_{\rm irr}}\right)^2 + \frac{\mathcal{J}^2}{4M_{\rm irr}^2}, \tag{3.39}$$

where $\mathcal{J}$ the magnitude of the angular momentum given by Eq. (3.38), and $Q$ is the horizon charge given by Eq. (3.22) (computed using the solved electric field). In Sec. 3.3, we use the sum of the Christodoulou masses, denoted $M_{\rm T,C}$, which gives the total mass of the binary at infinity.

### 3.2.3 Controlling BH spin and ADM linear momentum

In Sec. 3.1.1, we introduced two parameters in the boundary conditions, $v_0^i$ in Eq. (3.9) and $\Omega_r^i$ in Eq. (3.10), which we use to control the ADM linear momentum and the black hole spins, respectively. We discuss how we set them here. As in [120], we iteratively set $v_0^i$ in Eq. (3.9) to drive the ADM linear momentum to zero. However, we use a simpler iterative procedure, setting

$$v^i_{0,n+1} = v^i_{0,n} - \frac{P^i_{{\rm ADM},n}}{M_{\rm T}}, \tag{3.40}$$

where $n$ indexes the Newton iterations. We start the iteration from $v^i_{0,0} = 0$.

We similarly drive the dimensionless spins to their desired values (those of the superposed Kerr-Newman metrics) by adjusting $\Omega_r^i$ using a simple iteration inspired by the form of the Kerr-Newman horizon angular velocity [135]. We start with the angular velocity of the Kerr-Newman spacetime used in the superposition

$$\Omega^i_{r,0} = \frac{\mathcal{J}^i_{\rm KN}}{4M_{\rm Chr,\,KN}M^2_{\rm irr,\,KN}}, \tag{3.41}$$

where $M_{\rm irr,\,KN}$, $M_{\rm Chr,\,KN}$, and $\mathcal{J}^i_{\rm KN}$ are the irreducible mass, horizon mass (i.e., Kerr-Newman mass parameter), and angular momentum of each superposed black hole, respectively. We then iteratively update $\Omega_r^i$ using

$$\Omega^i_{r,n+1} = \Omega^i_{r,n} + \frac{M^2_{{\rm Chr},n}\chi^i_{\rm KN} - \mathcal{J}^i_n}{4M_{{\rm Chr},n}M^2_{{\rm irr},n}}, \tag{3.42}$$

| Name | $q$ | $\mathcal{Q}_1$ | $\mathcal{Q}_2$ | $\boldsymbol{\chi}_1$ | $\boldsymbol{\chi}_2$ | $M_{\rm T}\Omega_0$ | $d/M_{\rm T}$ | $\zeta$ |
|---|---|---|---|---|---|---|---|---|
| `qc-sp5` | 1 | 0 | 0 | (0, 0, 0.50) | (0, 0, 0.50) | 0.01941 | 10 | 0.5 |
| `qc-hs` | 1.16 | 0 | 0 | (0, 0, 0.69) | (0, 0, 0.79) | 0.02848 | 16 | 1.25 |
| `qc-hc` | 1.16 | 0.97 | −0.97 | (0, 0, 0) | (0, 0, 0) | 0.02848 | 10 | 2 |
| `qc-mc` | 1.16 | 0.59 | −0.45 | (0, 0, 0) | (0, 0, 0) | 0.02848 | 10 | 2 |
| `qc-sp7cp5` | 1.16 | 0.56 | −0.43 | (0, 0.69, 0) | (0.47, 0, 0) | 0.02848 | 10 | 2 |

Table 3.1: Summary of the parameters of the initial data sets for orbiting binaries ("qc" for "quasicircular"), also indicating the case for which we performed a test evolution with BAM. Here $\mathcal{Q}_A$ and $\boldsymbol{\chi}_A$ are the dimensionless charge and spin on black hole $A$, respectively. Additionally, $q$, $\Omega_0$, correspond to the mass ratio and angular velocity, respectively. We set the radial velocity, i.e., $\dot{a} = 0$ for all the cases, except for `qc-sp5` where we set $\dot{a} = 0.006531$. Finally, $d$ is the separation between the two black holes and $\zeta$ is the attenuation width parameter defined in Eq. (3.43). We set the velocity of each black hole using the Newtonian expression in terms of $\Omega_0$ and $d$.

where, as in Eq. (3.40), $n$ indexes the Newton iterations. Thus, e.g., $\mathcal{J}^i_n$ is the horizon angular momentum recomputed after the $n^{\rm th}$ iteration on the excision surface under consideration. Additionally, $\chi^i_{\rm KN} := \mathcal{J}^i_{\rm KN}/M^2_{\rm Chr,\,KN}$ is the dimensionless spin vector of the corresponding Kerr-Newman metric used in the superposition.

## 3.3 Results

We now discuss the initial data we constructed to test the code, particularly its convergence with resolution, and the exploratory evolutions we performed. We summarize the cases we consider in Table 3.1.

To test the convergence of our initial data solver, we consider four representative orbiting configurations: two nonspinning cases with high (`qc-hc`) and moderate (`qc-mc`) charge, one uncharged case with reasonably high spins (`qc-hs`), and finally, a more generic precessing binary with moderate charges and spins (`qc-sp7cp5`). We choose opposite signs for the charges in the charged cases to increase the asymmetry and thus provide a more stringent test of the solver. We use the same number of points ($N$) in the $A_{\rm Ans}, B_{\rm Ans}$, and $\phi$ directions for each configuration, and set

$$w_A = \zeta \frac{M_A}{M_1 + M_2} d, \tag{3.43}$$

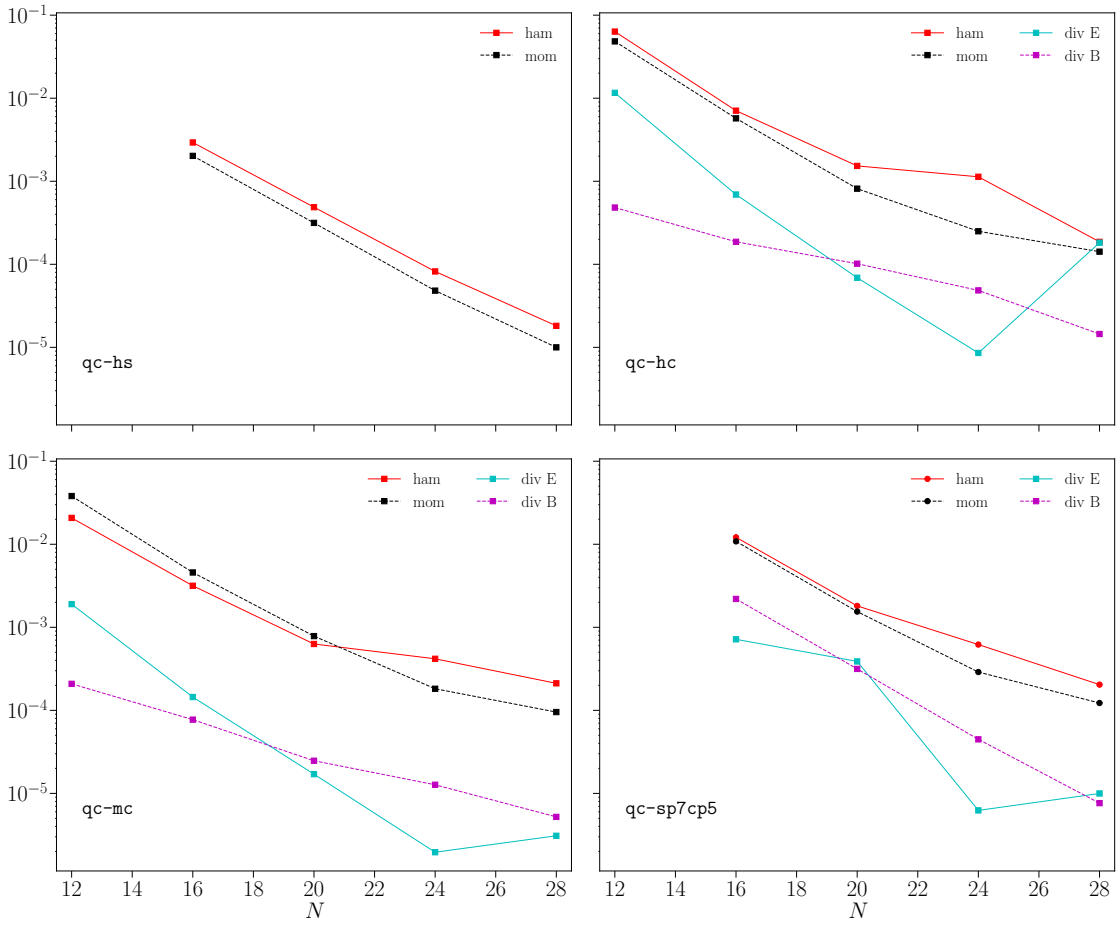


Figure 3.2: Convergence of the constraint residuals for four different binary configurations, a highly spinning case (`qc-hs`), highly charged (`qc-hc`) and moderately charged (`qc-mc`) cases, and a more generic charged and spinning case (`qc-sp7cp5`). In all cases, we show the Hamiltonian and momentum constraints ("ham" and "mom"), and for the charged cases, we also show the electric and magnetic constraints ("div E" and "div B"). The horizontal axis gives the number of points used for each coordinate ($N$) and the vertical axis shows the $L^2$ norm of the physical constraints over the entire computational grid (scaled by the total volume of the computational grid). Hence, we scale the $L^2$ norm by the square of the total Christodoulou mass $M_{\mathrm{T,C}}$. For the momentum constraint, this includes the Euclidean vector norm on the components of the constraint. For $N = 12$, the initial data solver does not converge for `qc-hs` and `qc-sp7cp5`, since the larger gradients near the horizon from significant spin require more resolution to reach the convergent regime.

for the attenuation weights in Eqs. (3.7), (3.17), and (3.18). Here, $\zeta$ is a dimensionless free parameter and $d$ is the coordinate distance between centers of the two black holes. We set $\Omega_0$ and $\dot{a}$ in Eq. (3.10) by performing iterative eccentricity reduction. For the other initial data sets, we set $\Omega_0$ using the PN expression in [136] for `qc-sp5`, and set $\dot{a} = 0$. As we discuss later, we do not expect these settings to give low-eccentricity initial data, so we do not attempt to include the effects of the charge. In Fig. 3.2 we show the convergence of the geometric (Hamiltonian and momentum) and EM constraint residuals for all the four cases. We find the expected exponential (spectral) convergence at low resolutions, but find slower convergence at higher resolution.

In particular, for the geometric constraints, we see spectral convergence only up to $N = 20$ for the highly charged case (`qc-hc`). For the highly spinning case (`qc-hs`), the convergence is exponential up to $N = 28$. For the binary with more generic parameters (`qc-sp7cp5`), the rate of convergence is better than for the highly charged case (possibly due to the fact that the more generic system is less extreme), but the Hamiltonian constraint shows subexponential decay after $N = 20$. While this looks similar to the subexponential convergence found for the construction without attenuation functions in [113], the cause of the slower than expected convergence in our case must be due to a different cause: We use attenuation functions when superposing both the metric and the electromagnetic fields, which ensures that they fall off rapidly at infinity, so there is no possibility for the logarithmic term in the solution that caused the subexponential convergence in [113]. In fact, we do not even have the co-rotation term in the outer boundary condition for the shift that leads to that logarithmic term in the Hamiltonian constraint when combined with the $1/r$ falloff of the conformal metric without attenuation functions. One other possible cause that we can exclude is the adjustments to $v_0$ and $\Omega_r^i$ that we perform during the Newton iterations. We disabled these iterations but found no improvement in the speed of convergence. For the EM constraints, we see spectral convergence for electromagnetic constraints up to $N = 24$ for all the configurations except for `qc-sp7cp5` at $N = 20$. The rate of exponential decay, however, is much slower for the magnetic constraint than for the electric constraint.

We also illustrate the solved electric and magnetic fields for the `qc-sp7cp5` case, with its oppositely charged, spinning black holes, in Fig. 3.3. As one would expect, we observe an overall electric dipole moment aligned along the axis joining the two black holes, and a magnetic dipole for each black hole aligned with its spin axis. Further, the magnetic field due to the orbital motion of the black holes (not visible in the figure, since it is perpendicular to the plane plotted and thus projected out) is consistent with the magnetic field around two charges with different signs moving in opposite directions. Unsurprisingly, we find the largest corrections to the unsolved superposed electric and magnetic fields near

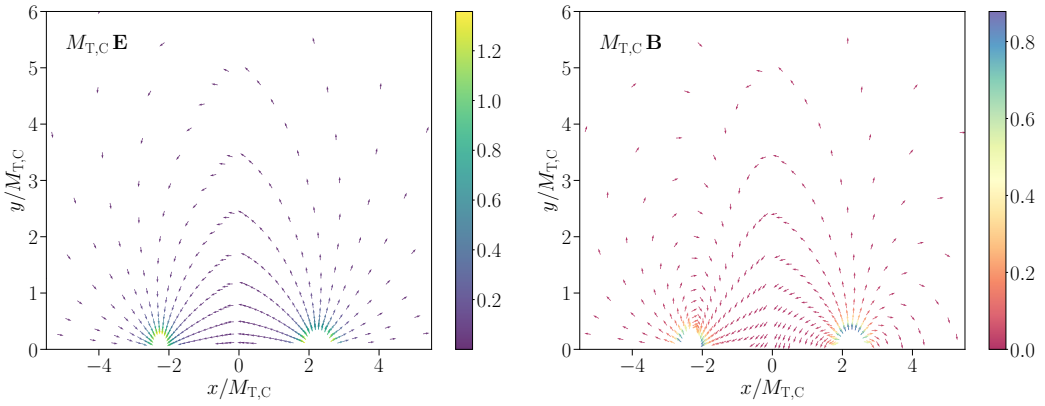


Figure 3.3: The electric (top panel) and magnetic (bottom panel) fields (multiplied by $M_{\rm T,C}$) at the grid points around the two black holes in the $xy$-plane for `qc-sp7cp5`. The arrows represent the unit vectors of the projection of the field into the $xy$-plane. The magnitude of the projection is shown by the color scheme. The black hole on the left (right) has its spin aligned along the $x$- ($y$-) axis giving rise to two magnetic dipole moments aligned with the two spin axes.

each black hole.

Finally, we check how well the isolated horizon condition on the EM fields at the horizon [Eq. (3.24)] is satisfied in our initial data. We do this by computing the $L^2$ norm of the residual over the horizon, as well as the version with the sign reversed, for comparison. Specifically, we define

$$Z_i^{\pm} := E_i^{\parallel} \pm (s \times B)_i, \tag{3.44a}$$

$$\mathrm{EB}^2_{\mathrm{res},\pm} := \oint_{\mathcal{S}_{\rm A}} \gamma^{ij} Z_i^{\pm} Z_j^{\pm} \sqrt{h}\, s^k dS_k, \tag{3.44b}$$

where $\mathrm{EB}_{\mathrm{res},+}/\mathrm{EB}_{\mathrm{res},-}$ gives a dimensionless measure of how well the relation is satisfied on each excision surface. We found the ratio to be the lowest (0.04) for the larger black hole in `qc-sp7cp5` and the largest (0.09) for the smaller black hole in `qc-mc`. Additionally, in the nonspinning cases, we found this ratio to depend on the asymmetry of the magnitude of the two dimensionless charges. Hence, even though the black holes in `qc-mc` have smaller charges than in `qc-hc`, we find the deviations from the isolated horizon condition to be larger for `qc-mc` which has the largest dimensionless charge ratio among the charged, nonspinning configurations.

## 3.4 Conclusions

In this chapter, we constructed initial data for spinning, charged, orbiting binary black holes by extending the superposed Kerr-Schild construction for vacuum binary black hole initial data presented in [113]. In contrast to previous work [109] which constructed conformally flat puncture initial data, our construction gives conformally curved initial data with excision. It also provides a complementary implementation of the original vacuum construction in [113] with a different numerical setup and a slightly different choice of boundary conditions. Specifically, we transfer the corotation and expansion terms from the outer to the inner boundary condition for the shift. We tested our initial data construction for several cases including binaries with highly charged black holes and black holes with both charge and spin. We performed convergence tests and found our initial data implementation gives exponential convergence for low resolutions, but slower convergence for higher resolutions.

# Chapter 4

# Exploratory evolutions of charged binary black hole initial data

In this chapter, we present the results from the test evolutions of the initial data we constructed in Chapter 3. Several previous studies have investigated the dynamics of charged black holes in full numerical relativity. Zilhão *et al.* [137, 138] performed simulations of head-on collisions of nonspinning charged black holes from rest, using either analytic equal charge-to-mass ratio initial data or a simple numerical initial data construction to obtain opposite charge-to-mass ratios. Liebling *et al.* [139] carried out evolutions for weakly charged (electric and magnetic) black holes on quasicircular orbits starting from approximate initial data. More recently, Bozzola *et al.* evolved a set of nonspinning binary black holes with small to moderate charges on quasicircular orbits in [60, 61] and head-on collisions of boosted, charged black holes in [140].

Here we consider evolutions of vacuum data initial data describing orbiting binaries using the BAM code [13], and head-on collisions of charged, and uncharged boosted black holes, using the HAD code [64]. We were unable to produce evolutions of orbiting binaries with HAD[1], even when evolving a vacuum case for which the BAM evolution orbited. Thus, in Sec. 4.1 we discuss the evolution of an uncharged binary in quasi-circular orbit, evolved using BAM. In sections 4.2 an 4.3, we discuss the evolution of charged, and uncharged, boosted black holes using HAD, and compare our results with Newtonian estimates. We conclude with a discussion of our results in Sec. 4.4.

[1]Specifically, we found that the evolutions of orbiting initial data with HAD initially resemble quasi-circular orbits, but quickly the trajectory of the black holes becomes nearly head-on. We discuss this issue further in the Sec. 4.4.

## 4.1 Uncharged binary black holes in orbit

For the uncharged case, we evolved an equal-mass, equal-aligned-spin quasicircular binary inspiral in orbit (`qc-sp5`, with dimensionless spins of 0.5 in the direction of the orbital angular momentum; see Table 3.1) using BAM with the BSSN formulation of the equations and the standard puncture gauge. Since BAM is designed to evolve puncture initial data, and our initial data solver generates excision initial data, we used a generalized version BHfiller algorithm (see Sec.3.2 in [128], or Appendix B in [1], for the generalized version) to fill inside the non-spherical excision surfaces in BAM.

For this initial test, we used 16 points in each direction to construct the initial data using SGRID. For the evolution, we use seven refinement levels with three moving levels and four fixed levels. Each refinement level has half the grid spacing of the previous one with a minimum grid spacing of $0.0625M_{\rm T}$. The outer boundary of the computational domain is at $\sim 250M_{\rm T}$. We use fourth-order spatial finite differencing and fourth-order integration in time, with a Courant factor of 0.25. We extract the gravitational waves at a radius of $r_{\rm ext} = 50M_{\rm T}$.

We reduced the eccentricity by adjusting $\Omega_0$ and $\dot{a}$ using the iterative method in [121], where we measure the eccentricity using the puncture tracks. We found that the eccentricity one obtains from the post-Newtonian values for $\Omega_0$ and $\dot{a}_0$ given in [136] is large enough that the iterative method does not reduce the eccentricity when starting from those values. We thus adjusted those parameters by hand until the eccentricity was small enough that the iterative method produced further reductions of the eccentricity. We obtained an eccentricity of about 0.06, which is relatively large, compared to the eccentricities needed for waveform modeling (e.g., the eccentricities of $\sim 10^{-3}$ achieved for some of the simulations produced in [141]). While we could have carried out further iterations of the eccentricity reduction procedure, we chose not to for this initial test. In particular, the unusual nature of the eccentricity reduced setup we obtained, where the coordinate separation between the punctures increases before decreasing when the data are evolved, deserves more careful investigation.

In Figs. 4.1 and 4.2, we show the real part of the quadrupolar ($l = m = 2$) mode of the Weyl scalar $\psi_4$, and the puncture tracks for the last $\sim 8$ orbits before merger, respectively, for `qc-sp5`, to illustrate that they are qualitatively as expected. As is clear from the nearly overlapping puncture tracks, the binary still has a relatively large eccentricity (consistent with the value of $\sim 0.06$ obtained above). An important consideration when constructing initial data is how much the properties of the binary (e.g., black hole spin) change during early states of the evolution, as the system relaxes and emits junk radiation. We observed

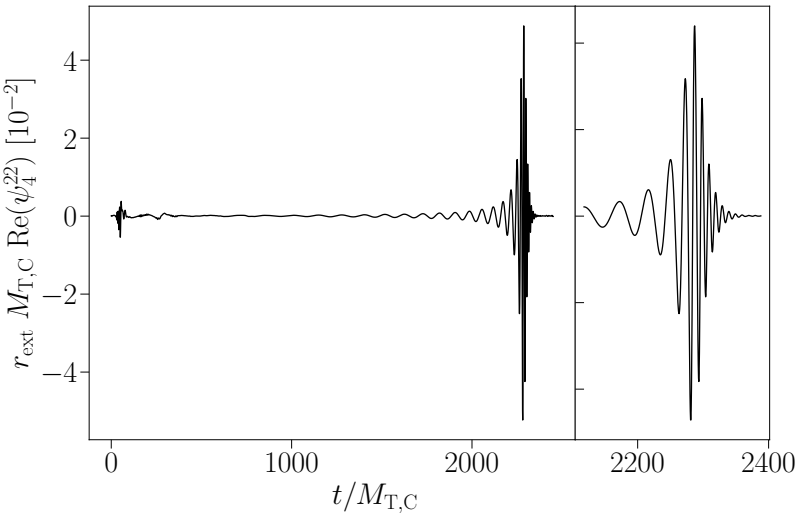


Figure 4.1: The real part of the $l = m = 2$ mode of the Weyl scalar $\psi_4$ from the uncharged, quasicircular, aligned-spin evolution `qc-sp5`. The left panel shows the complete waveform, and the right panel shows the waveform around the merger.

that the dimensionless spins settle to 0.49 (compared to the desired value of 0.5) after the first $900M_{\rm T,C}$ during which the system relaxes by emitting junk radiation. The relative error between the computed and desired spins decreases through the first $900M_{\rm T,C}$ and is $\sim 6\%$ at its maximum.

## 4.2 Head-on collisions of charged binary black holes

We now consider head-on collisions of charged black holes. For our tests of charged, head-on collisions, we evolved equal-mass, equal-charge, nonspinning binaries, as well as some uncharged, boosted head-on collisions (see Table 4.1 for an overview of these cases). The charged cases allow us to compare with previous numerical work [137, 138]. In particular as discussed below, analytical scalings found in their work agree well with our results.

We used a resolution of $(18, 18, 12)$ points in the $A_{\rm Ans}$, $B_{\rm Ans}$, and $\phi$ directions to generate the initial data in SGRID. The HAD evolutions used four refinement levels and each refinement level has half the grid spacing of the previous one, with a minimum grid spacing of $0.0891M_{\rm T}$. The outer boundary of the computational domain is at $\sim 72M_{\rm T}$. We used

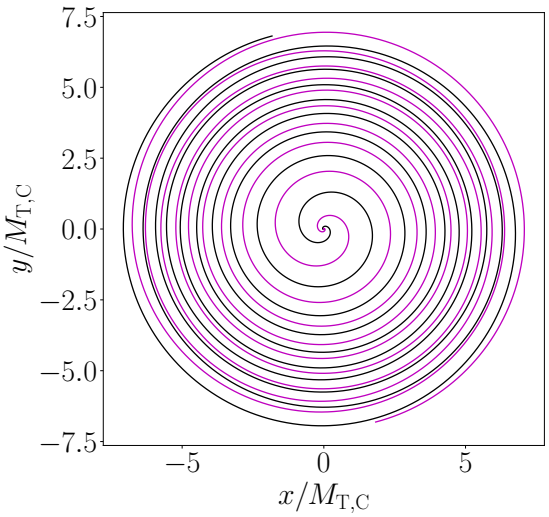


Figure 4.2: Puncture tracks of the two black holes for the `qc-sp5` evolution. The tracks show approximately 8 orbits before merger and demonstrate the nonnegligible eccentricity of $\sim 0.06$.

fourth-order spatial finite differencing and third-order integration in time with a Courant factor of 0.25. We extract gravitational and electromagnetic waves at $r_{\rm ext} = 50M_{\rm T}$. For the electromagnetic emission, we compute the scalar function $\Phi_2$ that contains the transverse radiative degrees of freedom of the electric field, in the asymptotic limit [142]. The details of the evolution system (BSSN with the standard puncture gauge plus constraint damping for the EM equations) and code are described in [41] which evolved binary black holes in Einstein-Maxwell-dilaton theory. For these evolutions we simply set the dilaton coupling parameter $\alpha$ to zero.

In Fig. 4.3, we compare the quadrupolar mode of $\psi_4$ between HAD and BAM evolutions for a head-on collision of two uncharged black holes starting from rest. Both waveforms are extracted at $r_{\rm ext} = 50M_{\rm T}$. Note that while the junk radiation profiles show some differences, the merger section of the waveform is in good agreement. While we have not attempted to quantify the error budgets of the two simulations, we anticipate that the differences seen are well within the combined error budget, particularly since these are not particularly high resolution simulations and have rather small GW extraction radii.

In Fig. 4.4, we show the $l = 2, m = 0$ mode of gravitational and electromagnetic radiation from the head-on collisions of binary black holes for various charge-to-mass ratios,

| Name | $\mathcal{Q}_1 = \mathcal{Q}_2$ | $v$ | Evol |
|---|---|---|---|
| `ho-v0q0` | 0.0 | 0.0 | HAD, BAM |
| `ho-v0qp1` | 0.1 | 0.0 | HAD |
| `ho-v0qp3` | 0.3 | 0.0 | HAD |
| `ho-v0qp5` | 0.5 | 0.0 | HAD |
| `ho-vp1q0` | 0.0 | 0.1 | HAD |
| `ho-vp3q0` | 0.0 | 0.3 | HAD |

Table 4.1: Summary of the parameters of the initial data sets for head-on collisions (abbreviation "ho" ) of equal-mass, equal-charge, nonspinning binaries we constructed and performed test evolutions of with HAD and BAM. Here, $v$ is the magnitude of the velocity of each black hole. We set $d = 10M_{\rm T}$ and $\zeta = 2$ for all configurations listed here and set $\dot{a}_0 = -v/d$ for the head-on collisions.

including the $\mathcal{B} := 1 - \mathcal{Q}^2$ Newtonian scaling that [137] found to account for most of the amplitude's dependence on the charge. In [137] the authors place the black holes on the $z$-axis, whereas in our setup, we place them on the $x$-axis. Thus, to make a direct comparison with [137], we transformed our waveforms to place the black holes along the $z$-axis using the `quaternionic` package [143, 144]. We find that the waveforms from our evolutions satisfy the scalings found in [137] for the merger-ringdown portion of the waveform with reasonable accuracy, though with larger differences than in [137]. Specifically, [137] found differences of at most 2% compared to the scaling for charges up to 98% of maximal. In our simulations, however, we found the differences to be larger (up to $\sim 3\%$) for charges up to 50% of maximal, though our evolutions are preliminary, and we did not attempt to assess convergence, in addition to the issues with the effects of the filling mentioned previously.

## 4.3 Head-on collisions of boosted uncharged binary black holes

We also considered head-on collisions of uncharged black holes boosted towards each other with velocity parameters of 0.1 and 0.3, as well as an unboosted case, for comparison. In the boosted cases, the assumption that the system is in quasi-equilibrium breaks down, and hence our choice of setting $u_{ij} = 0$ becomes increasingly inaccurate for larger initial velocities. However, we still find that increasing the initial velocity decreases the time to merger, so we present these results as a further example of the code's ability to generate

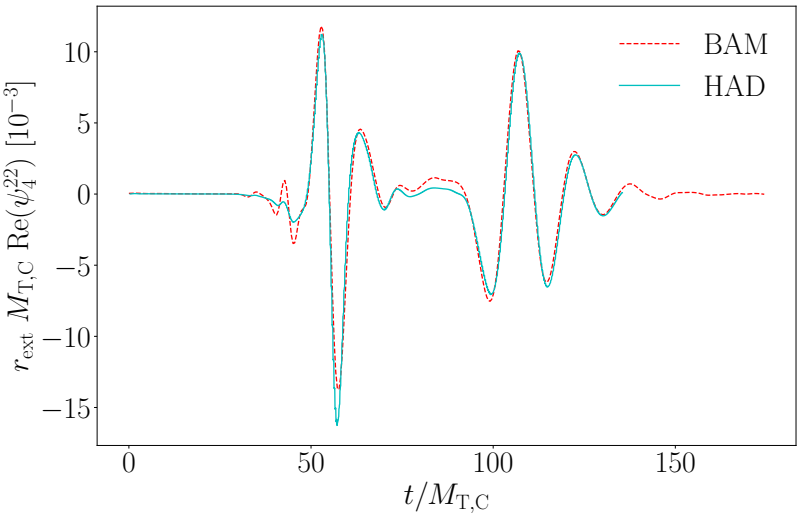


Figure 4.3: A comparison of the real part of the $l = m = 2$ mode of $\psi_4$ from the head-on collision of two uncharged black holes starting from rest (`ho-v0q0`) evolved using HAD and BAM. The waveforms are not aligned in any way.

initial data for generic binaries.

To quantify the effects of the boost, we consider the time to merger for each of the simulations ($t_{\rm sim}$), which we compare with the Newtonian estimate ($t_{\rm m}$), as in the charged case considered above. To compute the merger time from the simulations, we use the time it takes for each black hole to reach the origin, using the minimum of the lapse as a proxy for the location of the black hole. To compute the Newtonian estimate for the merger time, we use energy conservation. Specifically, we generalized the calculation done in [137] to include boosts. For two black holes each with mass $M/2$ and charge $Q/2$ placed initially at $x = \pm d/2$ with initial velocities of $v_0$, conservation of energy implies

$$M\dot{x}^2 - \frac{M^2\mathcal{B}}{4x} = Mv_0^2 - \frac{M^2\mathcal{B}}{2d}, \tag{4.1}$$

where $x$ is the position of one of the black holes and the overdot denotes a time derivative. Rearranging and integrating both sides, we get

$$t_{\rm m} = \frac{\mathcal{B}M}{\mathcal{Z}^3}\left[\frac{\pi}{2} - \arctan\left(\frac{2v_0}{\mathcal{Z}}\right)\right] - \frac{2v_0 d}{\mathcal{Z}^2}, \tag{4.2}$$

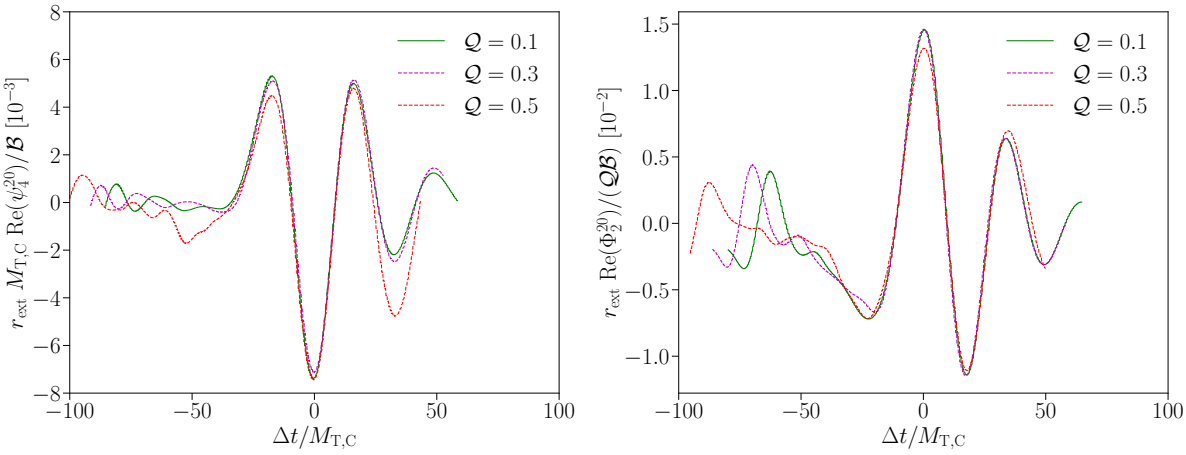


Figure 4.4: The $l = 2, m = 0$ mode (in the rotated frame with the black holes on the $z$-axis) of $\psi_4$ (top panel) and $\Phi_2$ (bottom panel) aligned at merger using the peak of the amplitude of the real part of the waveform. These waveforms correspond to head-on collisions of equal-mass, nonspinning charged black holes evolved using HAD for different charge to mass ratios, i.e., `ho-v0qp1`, `ho-v0qp3`, and `ho-v0qp5`.

where

$$\mathcal{Z} := \sqrt{\frac{\mathcal{B}M}{d} - 4v_0^2}, \tag{4.3}$$

where we evaluate the arctangent on the right-hand side of the branch cut (so its real part is $\pi/2$) for the cases where $\mathcal{Z}$ is imaginary, which ensures the result is always real. For the unboosted case (`ho-v0q0`), we find the time from the simulation, $t_{\rm sim}$, to be larger than $t_{\rm m}$ with a relative error $\sim 18\%$. For the boosted cases, similar to the charged case, we scale both $t_{\rm sim}$ and $t_{\rm m}$ by the corresponding computation for the unboosted case and denote these scaled values by $\tilde{t}_{\rm m}$ and $\tilde{t}_{\rm sim}$, respectively. We find $\tilde{t}_{\rm sim}$ to be larger than $\tilde{t}_{\rm m}$ for both `ho-vp1q0` and `h0-vp3q0`, and the relative error between them to be $\sim 57\%$ for `ho-vp1q0`, and $\sim 103\%$ for `h0-vp3q0`.

There could be several reasons behind these large discrepancies for both charged and uncharged, boosted cases. In particular, our method to infer the collision time from the numerical evolutions likely overestimates the merger time compared, e.g., to using the first appearance of a common apparent horizon to determine the merger time, as was done in [137]. Additionally, for the boosted cases, as mentioned before, we use the quasi-equilibrium approximation ($u_{ij} = 0$) beyond its regime of validity. This, in addition to the

issues with filling the black holes described earlier and the effects of junk radiation, can result in the black holes in the simulation having different initial velocities than those used in the construction of the initial data.

As a rough check, we estimated the initial velocities of the black holes using the location of the black hole and finite differencing. We started at $13.5M_{\rm T,C}$ to be after the initial transients and considered a time span of $7M_{\rm T,C}$, chosen by eye so that a constant velocity given by the finite difference gives a good approximation to the time dependence of the black holes' positions. We found the initial velocities to be 0.087 and 0.130 for `ho-vp1q0` and `h0-vp3q0`, respectively. For `h0-v0q0`, we found the computed velocity to be zero, in agreement with the velocity used in the computation of the initial data. Using these velocities in the merger time calculation reduced the computed merger time as well as the relative error between $\tilde{t}_{\rm m}$ and $\tilde{t}_{\rm sim}$ to $\sim 23\%$ and $\sim 74\%$ for `h0-vp1q0` and `h0-vp3q0`, respectively.

## 4.4 Discussion

In this chapter, we carried out exploratory evolutions of charged and uncharged initial data using two different evolution codes (BAM in the uncharged case and HAD with both charged and uncharged data). Specifically, we evolved a quasicircular, uncharged, spinning binary with an eccentricity of $e \sim 0.06$ for approximately 8 orbits before merger, with BAM. In the charged case, we considered head-on collisions with different charge-to-mass ratios and found that our numerical results are consistent with the simple (Newtonian) analytic scalings presented in [137]. Our estimates of the time of collapse for boosted, head-on collisions differed significantly from a similar Newtonian estimate. While a number of factors particular to these results (as discussed in Sec. 4.3) might explain such differences, we observed that the collapse time decreased with increasing initial velocity as would be expected.

However, we were unable to obtain an orbiting evolution with HAD even in the uncharged case. We suspect that failure to orbit may be due to the method of filling the excised interior developed in HAD for these evolutions. In particular, even though [145] showed that the constraint violations from the filling do not propagate outside the horizon in BSSN, the finite difference stencils extend inside the horizon and thus the filling affects the evolution through the derivatives of the fields. In fact, [145] finds that one needs the filling to extend out to a coordinate radius at most 0.4 times the horizon radius in order for the filling not to affect the evolution (though the isotropic coordinate system of their initial data is rather different from our Kerr-Schild one). However, for our initial data

construction, the apparent horizon coincides with the excision surface, and so it is necessary to fill all the way to the apparent horizon. It thus might be worthwhile to extend the construction to allow for the excision surface to be inside the apparent horizon by using negative expansion boundary conditions, as in [146].

# Chapter 5

# Towards a parameterized hardness model for Boolean SAT instances

In this chapter, we investigate a parameterized hardness model for Boolean SAT instances. Building such a parameterized hardness model involves two parts. First, one needs to identify a suitable parameterization of a SAT instance, that is amenable to a theoretical analysis, i.e., can be used to prove that SAT instances with good values of such parameters do not have exponential–sized proofs. Second, one needs to also show that such parameters work well in practice; i.e., predictive of the solver runtime for different categories of SAT instances. This, however, has been challenging to do in practice. In particular, proposed parameters amenable to a theoretical analysis have either been empirically shown to be a poor predictor of solving time [85, 147] or limited in their range of applicability [148], whereas parameters that have been experimentally shown to be predictive of the solver runtime, have been shown to have counter examples, i.e., instances with good values of such parameters have been shown to require exponential–sized proofs to refute, or equivalently, solve [149]. For example, it was empirically shown that parameters based on the community structure of a graph encoding of a SAT formula are strongly predictive of solver runtime [150], and are able to distinguish between industrial and random instances [79], that are known to be easy and hard for a SAT solver to solve, respectively. However, in [149], Mull *et al.* were able to show that a SAT instance with good community structure can have an exponential–sized proof, thus proving that community structure alone is insufficient to determine the hardness of a SAT instance.

Here, we consider the hierarchical community structure (HCS)[1] of a graph encoding of a

[1]The idea of HCS, in the context of Boolean formula, as introduced in the HCS paper [2] was introduced

SAT formula. Our main motivation to investigate such a parameterization is twofold. First, many real world SAT instances are likely to inherit the underlying hierarchical structure of the human–developed systems they usually represent [151]; e.g., software libraries organized into functions, which are then organized into modules. Second, such a parameterization, would avoid the counter example proposed in [149] and thus might be a more suitable candidate towards building a parameterized hardness model for SAT instances. We use a machine learning based approach to build an empirical hardness model of a SAT instance based on the HCS parameterization, to distinguish between different categories of SAT instances that are generally assumed to be easy or hard for CDCL SAT solvers, as well as predict the runtime of the solver for these instances.

This chapter is organized as follows. In Sec. 5.1 we discuss the notion of a HCS of a SAT instance, and in Sec. 5.2, we discuss the details of our empirical model to predict the hardness of a SAT instance using HCS. Specifically, in Sec. 5.2.1, we investigate the ability of HCS to distinguish between instances that are known to be easy and hard for a SAT solver, i.e., those from industrial and randomly generated or cryptographic applications, respectively, and in Sec. 5.2.2 we build an empirical hardness model to map the HCS based parameters of a SAT instance to its solving time for a specific SAT solver. Finally, in Sec. 5.3, we summarize the results of our experiments and discuss the theoretical implications of those results.

## 5.1 HCS of a Boolean SAT formula

To describe the HCS of a SAT formula, we first need to define the community structure of a graph. The community structure $\mathcal{H}(G)$ of a graph $G$ is a partition of its vertex set $V$, such that for each subgraph (community) over each partition $P$, there are more inter-community edges, than edges between two communities [152]. To compute a hierarchical community structure, one recursively constructs a community structure for each such subgraph, until a subgraph can no longer be divided into separate communities [153].

There are several ways to construct a community structure for a graph $G$. We use an approach that is based on finding a partition $P$ of the vertex set $V$ that maximizes a quantity called the modularity ($Q$) over all possible partitions of $V$, i.e.,

$$\mathcal{H}(G) = \text{argmax}_P \; Q(G, P). \tag{5.1}$$

by Ian Li and Vijay Ganesh.

The modularity $Q$ of a partition $P$ is given by

$$Q(G,P) := \frac{1}{2|E|} \sum_{u,v \in V} \left[ A_{u,v} - \frac{d(u)d(v)}{2|E|} \right] \delta_P(u,v), \tag{5.2}$$

where $A$ is the adjacency matrix of $G$, $d(u)$ and $d(v)$ are the vertex degrees of vertices $u$ and $v$, respectively, $|E|$ is the total number of edges in the graph, and $\delta_P(u,v)$ is quantity that is equal to one, if both $u$ and $v$ lie in the same community, and zero, otherwise. Intuitively, Eq. (5.2) computes fraction of the edges that fall within a given partition minus the expected fraction if edges were distributed at random, thus measuring the strength of division of a graph into communities. To compute the community structure of a the graph, we use the Louvain method [154] implemented in the Python package igraph [155].

To compute the HCS of a Boolean formula, we must first encode it into a graph. We use the simplest possible encoding, called a variable incidence graph (VIG), where each node corresponds to a literal in the formula, and two nodes share an edge if the two literals appear in the same clause in any part of the formula. For example, the VIG (and its corresponding HCS) for the Boolean formula

$$(x_1 \wedge \neg x_2 \wedge x_3) \vee (x_1 \wedge \neg x_3) \vee (x_3 \wedge x_4) \vee (x_4 \wedge x_5 \wedge x_6) \vee (\neg x_5 \wedge x_6 \wedge x_7 \wedge x_8), \tag{5.3}$$

is shown in Fig. 5.1. Note that such an encoding is not bijective, i.e., one cannot recover the boolean formula from the VIG. Further, the VIG does not encode information about the polarity of the variables, and furthermore, it compresses large clauses into a clique, which can significantly distort the overall structure of the VIG.

Given HCS of a Boolean formula, we compute[2] several parameters characterizing its HCS; for a complete list, see [2]. Broadly, for each SAT instance, they summarize the depth of HCS of decomposition, the size of each community, the number of communities they are connected to, and the ratio between the number of intra-community edges and the inter-community edges at each level of the structure. These parameters are not all independent, and in fact, some of them are highly correlated with each other, and hence, from an empirical standpoint, redundant. In addition to the HCS parameters, we also compute a few parameters independent of the HCS (e.g., the clause variable ratio) that characterize a SAT instance. In total, we use 49 parameters to build our empirical hardness model for SAT instances. In the next section, we discuss the details of our empirical model and its performance on a variety of SAT instances.

[2]The data collection was done by Ian Li and Jonathan Chung, under the guidance of Vijay Ganesh. My contribution was to build a statistical model to predict if—and which of the various features—are truly predictive of solver behaviour, and constitute a basis for further theoretical analysis. This was done with inputs from Ian and Jonathan, and under the supervision of Vijay Ganesh.

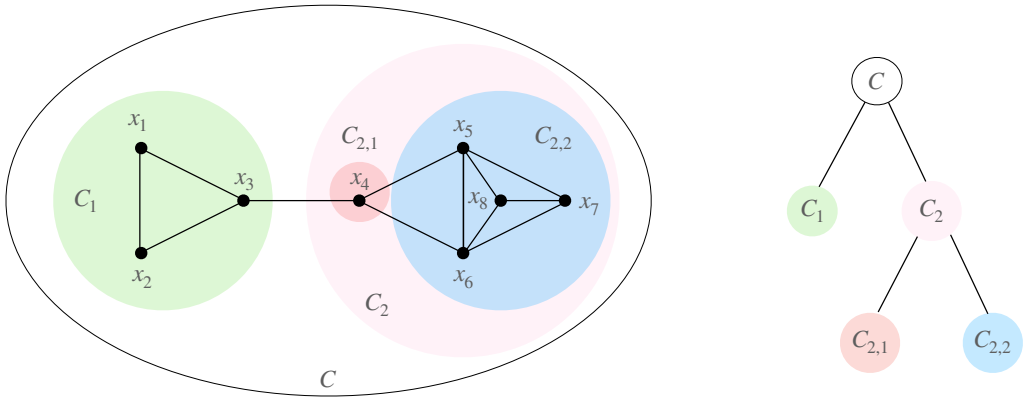


Figure 5.1: (Left) The variable incidence graph (VIG) of the Boolean formula given in Eq. (5.3) with nested circles showing the hierarchical community structure. Here, $C$ represents the root level community, that is the entire graph. Further, $C_1$ and $C_2$ are the two sub-communities containing nodes $(x_1, x_2, x_3)$ and $(x_4, x_5, ..., x_8)$ respectively. The community $C_2$ can be further decomposed into two communities $C_{2,1}$ and $C_{2,2}$, with literals $x_4$ and $(x_5, ..., x_8)$, respectively. (Right) The hierarchical structure of the partition of the vertex set shown as a tree.

## 5.2 Empirical hardness model for SAT using HCS

Our goal is to understand whether HCS of a SAT instance is predictive of its hardness, which, in our setting, corresponds to the solving time on a specific SAT solver. To answer this question, we need a model that maps the HCS parameters to the solving time of a SAT instance. Since no such canonical map exists in theory, we choose a model (map) and then evaluate the quality of our parameterization (i.e., HCS) for that model. This clearly introduces a problem, i.e., if the model performs poorly, how do we determine if the issue is the model, or the effectiveness of our parameterization. For example, previous studies [147] have used a linear (e.g., correlation) or higher order polynomial regression models to evaluate the performance of a particular parameterization in predicting the solving time of a SAT instance. However, if the relationship between such parameters and the solving time is highly nonlinear, such a model will perform poorly irrespective of the suitability of the parameterization in determining the hardness of a formula.

A more consistent approach, is to consider a generic, data-driven model, such as those used in machine learning. Machine learning based models, however, are often used as a black box, and known to be difficult to interpret. Since our end goal is to use the most

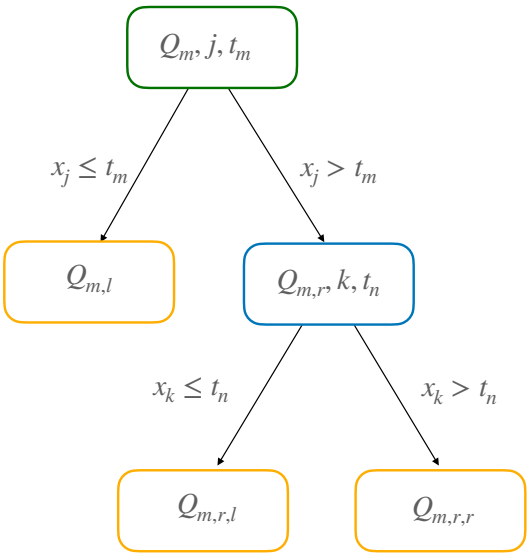


Figure 5.2: An example of a two–level decision tree, with one root node (red), one internal node (blue) and three leaf nodes (green). At the root node, the data $Q_m = \{x_i, y\}$ where $x_i$ are the set of features, and $y$ are the corresponding labels, is split into two subsets $(Q_{m,l}, Q_{m,r})$ on the $j^{\text{th}}$ feature, using a threshold $t_m$. The subset $Q_{m,r}$ is further split into $Q_{m,r,l}$ and $Q_{m,r,r}$ on the the $k^{\text{th}}$ feature for threshold parameter $t_n$. A split is only considered if the resulting tree minimizes an overall cost function; else the node terminates as a leaf node. In this simple case, learning the decision tree would involve learning the parameters $(j, t_m, k, t_n)$ that minimizes the associated cost function for the tree.

relevant HCS parameters for a more rigorous theoretical analysis, we use a simple machine learning model based on random forests [156], which can learn complex, highly nonlinear relationships, and yet have a relatively simpler structure, which makes them are easier to interpret than other models (e.g., deep neural networks).

Random forests are based on an ensemble of decision trees. A decision tree [157] is a nested chain of conditional statements (decision rules) that are learned from the data. Each node in the tree represents a decision rule, and can either branch into two further (internal) nodes or terminate in a leaf node, depending on the branching parameters for that node. Learning the decision tree essentially involves finding the branching parameters for all the nodes, that minimises a certain overall cost function (e.g., Gini impurity [157] or a mean squared loss) for the entire tree; see Fig. 5.2.

Once a decision tree is learned, it can then be used to classify data up to the precision

defined by the leaf nodes. Decision trees, however, have poor generalization error, i.e., they tend to overfit the data. Random forests prevent overfitting by constructing a large number of decision trees, each trained on a randomized subset of the data. In fact, a remarkable—and perhaps, non-intuitive—feature of random forests is that adding more trees does not lead to overfitting [156]. These randomized datasets are constructed by first sampling from the original dataset with replacement (bootstrapping) and then selecting a subset of features from this new dataset. For classification tasks, the algorithm returns the class selected by most trees, whereas for regression, it returns the prediction averaged over the ensemble of decision trees.

To quantify the merit of an HCS based parameterization for predicting the hardness, we ask two questions. First, we ask how well can we distinguish between different categories of SAT instances using HCS parameters. Second, we ask how well HCS parameters do in predicting the runtime of particular SAT instance. The first question naturally lends itself to a classification problem, whereas the second question corresponds to a regression problem (since the solving time is a continuous variable). Thus, we train a random forest classifier and regressor, to predict the category of a SAT instance and its solving time, respectively. We used an implementation of a random forest from the scikit-learn [158] library in Python. To train our random forest models, we considered all of the 49 parameters for $\sim 3000$ SAT instances equally distributed among 5 different categories (i.e., from applications generating such instances, namely verification, agile, random, crafted and crypto) with varying levels of hardness, and we tested the performance of our learned models over 5 cross-validation sets, and a sample size of 1000 SAT instances.

### 5.2.1 Predicting the category of a SAT instance

For the category classification problem, we found that our random forest model to perform extremely well. Concretely, we found our model to have an average accuracy score of $\sim 0.99$ over all the cross-validation sets. In fact, the classifier occasionally misclassified verification and agile instances, but never between verification and random/crafted instances.

Given the extremely high accuracy of our classifier, one may naturally ask if our model is overfitting. The remarkably high accuracy of our classifier is perhaps not as surprising when one considers a lower dimensional visualization of our data. A popular approach for visualizing higher dimensional data on a lower dimensional space is to use a method called t–distributed Stochastic Neighbour Embedding (t–SNE) [159]. On a high level, the t–SNE algorithm converts distances between data points to joint probabilities in both the high dimensional space as well as in the target lower dimensional space, and then tries

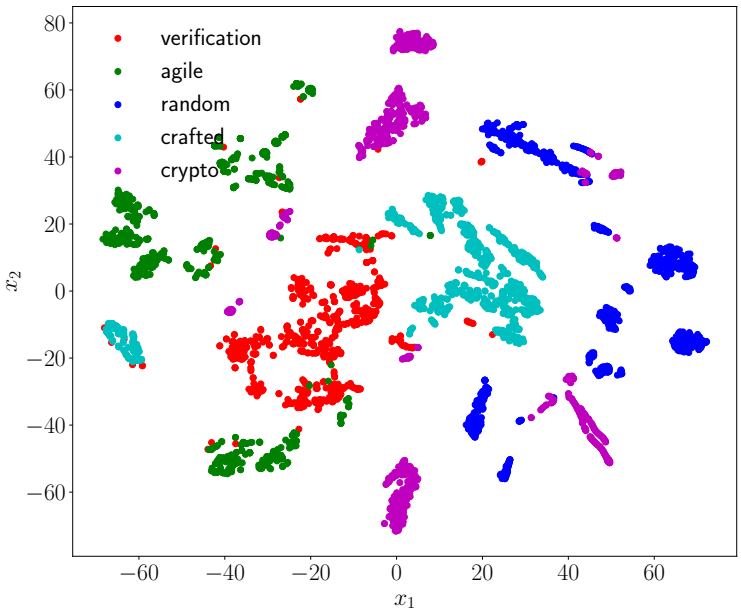


Figure 5.3: A 2D t–SNE embedding of our 49 dimensional data showing a clear separation between different categories of SAT instances. The axes $x_1$ and $x_2$ are arbitrary directions chosen by the t–SNE algorithm for the lower dimensional embedding. Note that the structure of a t–SNE embedding depends on the choice of certain parameters for the t–SNE algorithm. We verified that presence of well-separated clusters in the figure is independent of the choice of such parameters.

to minimize the Kullback-Leibler divergence [160] between the joint probabilities of the low-dimensional embedding and the higher-dimensional data. In Fig. 5.3, we show a two dimensional representation of our dataset computed using t–SNE. We observe that the categories of SAT instances are clearly separated even in the lower dimensional representation of the data, which suggests that the data might be well-separated even in the higher dimensional space, which would justify the high accuracy of our random forest classifier.

The high accuracy of our classification model strongly suggests that HCS based parameterization is very effective in capturing the underlying structure that make verification instances different from, e.g., random instances. In the following section, we investigate whether the underlying structure that distinguishes SAT instances from different cate-

gories, is also predictive of the hardness of the SAT formula, as measured by the runtime of the SAT solver for a given SAT instance.

### 5.2.2 Predicting the runtime of a SAT instance

For predicting the runtime, however, HCS parameters were significantly less predictive than they were for distinguishing between different categories of SAT instances. Specifically, we found our regression model to have an $R^2$ score of 0.83. The $R^2$ score measures the fraction of variance in the data that is unexplained by the model [161]. Thus, our regression model based on HCS parameters is able to account for only 83% of the variance in the solving time of a SAT instance. This suggests that the underlying structure that differentiates between different categories of SAT instances, might in fact be different than the structure that determines the hardness of a SAT formula, even though, empirically, SAT instances from different categories such as verification and random, are often considered to be easy and hard SAT instances, respectively. In Fig. 5.4, we show the predicted runtime by our random forest regression model with respect to the the actual runtime. We also see that our model, in general, performs much worse for predicting the solving time for harder SAT instances, than for easier instances. We also investigated how our regression model performed separately, for each category of instances. We found that the performance of our regression model varies with instance category. Concretely, agile outperformed all other categories with an average $R^2$ value of 0.94, followed by random, crafted and verification instances with scores of $0.81, 0.85$ and 0.74 respectively. Interestingly, the worst performance was shown by the instances in crypto, with an $R^2$ score of 0.48.

Finally, in order to find those HCS parameters that are most predictive of the runtime and category of an instance, we calculated the permutation importance score [156] for all the parameters. Permutation importance measures the average decrease in the predictive accuracy of the model when a single feature is randomly shuffled. In our case, as mentioned earlier, many of the HCS parameters are highly correlated, which can lead to inaccurate interpretations of importance of individual features [156]. Hence, we first performed hierarchical clustering on all 49 features to generate 22 clusters, and then picked a single feature from each of these clusters and ranked them (correspondingly, their parent clusters) according to their permutation importance scores. Among the HCS parameters, we found those based on the leaf-community size and inter-community edges of a SAT instance to be the most predictive for the accuracy of our hardness model.

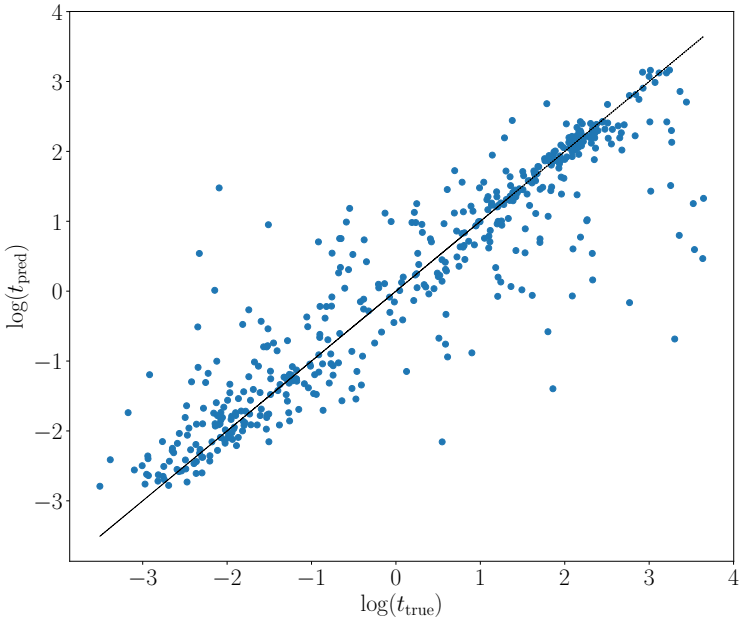


Figure 5.4: Predicted solving time ($t_{\text{pred}}$) vs. the actual solving time ($t_{\text{true}}$) for SAT instances with varying levels of hardness computed using the random forest regression model.

## 5.3 Conclusions

Given the central importance of the Boolean SAT problem in formal methods, and its potential utility in several areas of science, including numerical relativity, it is crucial that we understand why, in practice, we are able to solve what is conjectured to be an computationally intractable problem. Our main goal in this chapter, has been to investigate the suitability of a hierarchical community structure (HCS) based parameterized model for describing the hardness of SAT instances. To do this, we built a classification and regression model based on random forests, to distinguish between different categories of SAT instances (that are known to be easy and hard in practice) and to predict the solving time of a SAT instance on a specific SAT solver, respectively. We found that HCS is able to capture the underlying structural differences between real world (i.e., verification/agile) instances and random/cryptographic instances with very high ($\sim$ 99%) accuracy and is independent of the classification model. For predicting the solving time, the efficacy of the

HCS parameters was more moderate; we found our regression model fit the data with an $R^2$ value of 0.83. This suggests that the underlying structure of the formula that differentiates between easy (verification/agile) and hard (random/crypto) instances does not completely determine the hardness, or equivalently, solving time of a SAT instance. Thus, HCS of a Boolean formula may be necessary, but not sufficient to build a complete and consistent (with theory) parameterized hardness model.

Our conclusion is consistent with the theoretical results[3] presented in [2]. In our empirical investigations, we found the HCS parameters based on leaf-community size and inter-community edges to be the most predictive for predicting the category or the runtime of a SAT instance. While we were able to show that one can avoid hard SAT instances presented as counterexamples in [149] if one restricts the leaf community size of a SAT formula, we found that one can still find hard instances with small leaf communities unless one explicitly restricts the number of inter-community edges, and thus, hierarchical community structure alone is insufficient to build a hardness model for SAT instances.

[3]The theoretical results are due to Noah Fleming, Marc Vinyals, Antonina Kolokolova, Ian Li, and Vijay Ganesh.

# Chapter 6

# Summary & Future Directions

In this thesis, we investigated three different topics, of which, the first two are directly related to current challenges in computational relativity, and the third concerns a central problem in computer science, that has the potential to be useful for specific problems in computational relativity.

In Chapter 2, we investigated a spacetime discretization method in the context of numerical relativity. A spacetime discretization method, in many ways, is better suited for spacetime evolutions, than a 3+1 evolution scheme. In particular, they are agnostic towards a particular choice of a time coordinate, allow for *hp* adaptivity in both space and time, and have the potential to scale much more efficiently on distributed computing hardware than traditional 3+1 evolution methods. To construct our spacetime discretization method, we decomposed spacetime into spacetime volume elements using double null coordinates in spherical symmetry. We implemented a pseudospectral method to compute the solution in each spacetime element, and used an asynchronous computing model to distribute the computation across multiple processes. To test our numerical algorithm, we considered the evolution of a scalar wave in 1+1 dimensions, and the evolution of a Schwarzschild black hole and a self-gravitating scalar wave, in spherical symmetry. We found that our implementation performs very well (i.e., is stable, and convergences as expected) in all cases, except for the evolutions that include the axis of symmetry ($r = 0$), where our method fails to converge, likely due to numerical inaccuracies caused by the coordinate singularity at $r = 0$.

This problem due to the coordinate singularity, however, is not inherent to a spacetime method, but rather our choice of coordinates, i.e., double null coordinates adapted to spherical symmetry. While such a choice allowed us to investigate a spacetime method in

a simpler setting, such an approach based on double null coordinates may fail to work in higher dimensions, due to the presence of caustics [99]. Therefore, it would be useful to investigate spacetime methods based on unstructured spacetime elements, such as those explored in [107, 108].

In Chapter 3, we constructed conformally curved initial conditions for spinning charged black hole binaries in orbit. Specifically, we generalized the superpose-and-solve construction by Lovelace *et al.* [110] to include the effects of charge. Our approach—in addition to providing a completely independent method to construct charged binary black hole initial data—offers several advantages over the existing construction in [109], e.g., better control over the physics through the boundary conditions at the excision surface and the ability to construct binary initial data with larger spin, above the Bowen-York limit. We constructed initial data for different configurations of binary black holes (high charge, moderate spins, and a generic orbiting binary with spins), and found our method to converge exponentially for lower resolutions, but more slowly for higher resolutions.

There are several improvements one could make to our initial data construction. For example, it would be useful to understand and mitigate the loss of exponential convergence at higher resolutions, especially for binaries with large charge. This might require conformally rescaling the EM quantities as was done in [119, 109], and careful handling of the regularity conditions at the computational domain boundaries, where the gradients of electric constraint violations are the largest. Our construction can also be extended to construct initial data for binary black holes in Einstein-Maxwell-dilaton theory. In general, this would require superposing numerically constructed single black hole solutions for spinning black holes [162, 163]. Since analytical solutions are only known for black holes without spin, and for spinning black holes with specific values of the coupling parameter [164], an initial implementation could focus on these simpler cases. There are no additional constraint equations to solve for the dilaton field, just additional source terms in the Hamiltonian and momentum constraints. Evolutions with such initial data would improve upon the existing work by Hirschmann *et al.* [41] using approximate initial data, and also allow for comparisons with analytical work [46, 55].

In Chapter 4, we discussed some evolutions of charged and uncharged initial data using the HAD and BAM code. In particular, we discussed the evolution of uncharged, spinning binary black holes in orbit, using BAM. We also considered head-on collisions of charged black holes with different charge-to-mass ratios, and head-on collisions of uncharged black holes with different boosts, evolved using the HAD code. For the head-on collisions of charged black holes with different charge-to-mass ratios, we found our numerical results to be consistent with the simple (Newtonian) analytic estimates presented in [137]. For the head-on collisions of the boosted, uncharged black holes, we observed that the collapse time

decreased with increasing initial velocity. However, the time of collapse computed from the numerical simulation differed significantly from the corresponding Newtonian estimate.

Here, we were only able to evolve charged binary black holes for the head-on case, for the orbiting initial data (even for the uncharged case, which orbits in BAM) failed to orbit in HAD, likely due to the issues related to the black hole filling in HAD. We will thus need to resolve the outstanding issues with black hole filling in HAD. In particular, it would be worth exploring if setting the excision surface to be inside the apparent horizon, as in [146], mitigates the issues we encountered while evolving our excision initial data using puncture methods. One goal is to use our initial data to compute low-eccentricity charged binary black hole waveforms that are sufficiently accurate for data analysis applications. Such waveforms will allow us to check how sensitive current LIGO-Virgo tests [24, 25] are to completely consistent, parameterized deviations from GR. To evolve our charged initial data, it would also be useful to investigate other evolution codes, that use a different approach to filling inside black holes compared to HAD, and allow us to compute the quasilocal mass, charge, and spin of black holes during evolution.

In Chapter 5, we constructed an empirical hardness model for Boolean SAT instances using a parameterization based on the hierarchical community structure of SAT instances. Specifically, we built a machine learning model based on Random Forests to distinguish between different categories of SAT instances, and predict the runtime of a SAT solver for a given SAT instance, based on a characterization of its hierarchical community structure. We found that our parameterization works very well for distinguishing between different classes of SAT instances. However, for predicting the runtime of the solver, we discovered that our parameterization is not as effective, at least for the simple graph encoding based on a variable incidence graph we considered here. It might be useful to consider a different graph encoding that better encodes the clause structure of the formula, or consider the polarity of the Boolean variables. The goal however, cannot be to only improve the accuracy of the empirical model, but also investigate parameterizations that are amenable to a theoretical analysis. From such a point of view, it would be useful to investigate parameterizations that are theoretically motivated, rather than which perform well on empirical tests.

An important goal of this work in the context of this thesis, is to initiate a bridge between computational relativity, formal verification methods, and Boolean SAT solvers. There are several areas where Boolean SAT solvers could play an important role in numerical relativity applications, e.g., verification of floating point computations, or checking the existence of a solution for a set of nonlinear algebraic equations, and it would be interesting to investigate these, and other such avenues in the future.

# Bibliography


[1] Soham Mukherjee et al. "Conformally curved initial data for charged, spinning black hole binaries on arbitrary orbits". In: (2022). arXiv: 2202.12133 [gr-qc].

[2] Chunxiao Li et al. "On the Hierarchical Community Structure of Practical Boolean Formulas". In: *arXiv e-prints*, arXiv:2103.14992 (Mar. 2021), arXiv:2103.14992. arXiv: 2103.14992 [cs.LO].

[3] Michele Punturo, Harald Lück, and Mark Beker. "A Third Generation Gravitational Wave Observatory: The Einstein Telescope". In: *Advanced Interferometers and the Search for Gravitational Waves*. Ed. by Massimo Bassan. Vol. 404. Astrophysics and Space Science Library. Jan. 2014, p. 333. DOI: 10.1007/978-3-319-03792-9_13.

[4] Rana X. Adhikari et al. "Astrophysical science metrics for next-generation gravitational-wave detectors". In: *Class. Quant. Grav.* 36.24 (2019), p. 245010. DOI: 10.1088/1361-6382/ab3cff. arXiv: 1905.02842 [astro-ph.HE].

[5] K. Ackley et al. "Neutron Star Extreme Matter Observatory: A kilohertz-band gravitational-wave detector in the global network". In: *Publ. Astron. Soc. Austral.* 37 (2020), e047. DOI: 10.1017/pasa.2020.39. arXiv: 2007.03128 [astro-ph.HE].

[6] Mark A. Miller. "Accuracy requirements for the calculation of gravitational waveforms from coalescing compact binaries in numerical relativity". In: *Phys. Rev. D* 71 (2005), p. 104016. DOI: 10.1103/PhysRevD.71.104016. arXiv: gr-qc/0502087.

[7] Deborah Ferguson et al. "Assessing the readiness of numerical relativity for LISA and 3G detectors". In: *Phys. Rev. D* 104.4 (2021), p. 044037. DOI: 10.1103/PhysRevD.104.044037. arXiv: 2006.04272 [gr-qc].

[8] Francois Foucart et al. "Snowmass2021 Cosmic Frontier White Paper: Numerical relativity for next-generation gravitational-wave probes of fundamental physics". In: (Mar. 2022). arXiv: 2203.08139 [gr-qc].

[9] Lawrence E. Kidder et al. "SpECTRE: A Task-based Discontinuous Galerkin Code for Relativistic Astrophysics". In: *J. Comput. Phys.* 335 (2017), pp. 84–114. DOI: 10.1016/j.jcp.2016.12.059. arXiv: 1609.00098 [astro-ph.HE].

[10] Milinda Fernando et al. "Massively Parallel Simulations of Binary Black Hole Intermediate-Mass-Ratio Inspirals". In: (July 2018). DOI: 10.1137/18M1196972. arXiv: 1807.06128 [gr-qc].

[11] Frank Löffler et al. "The Einstein Toolkit: a community computational infrastructure for relativistic astrophysics". In: *Classical and Quantum Gravity* 29.11 (May 2012), p. 115001. DOI: 10.1088/0264-9381/29/11/115001. URL: https://doi.org/10.1088/0264-9381/29/11/115001.

[12] Bela Szilagyi, Lee Lindblom, and Mark A. Scheel. "Simulations of Binary Black Hole Mergers Using Spectral Methods". In: *Phys. Rev. D* 80 (2009), p. 124010. DOI: 10.1103/PhysRevD.80.124010. arXiv: 0909.3557 [gr-qc].

[13] Bernd Brügmann et al. "Calibration of Moving Puncture Simulations". In: *Phys. Rev. D* 77 (2008), p. 024027. DOI: 10.1103/PhysRevD.77.024027. arXiv: gr-qc/0610128.

[14] Michael Dumbser et al. "Conformal and covariant Z4 formulation of the Einstein equations: strongly hyperbolic first-order reduction and solution with discontinuous Galerkin schemes". In: *Phys. Rev. D* 97.8 (2018), p. 084053. DOI: 10.1103/PhysRevD.97.084053. arXiv: 1707.09910 [gr-qc].

[15] Ramesh Narayan et al. "HEROIC: 3D general relativistic radiative post-processor with comptonization for black hole accretion discs". In: *mnras* 457.1 (Mar. 2016), pp. 608–628. DOI: 10.1093/mnras/stv2979. arXiv: 1510.04208 [astro-ph.HE].

[16] Yucong Zhu et al. "hero – A 3D general relativistic radiative post-processor for accretion discs around black holes". In: *Monthly Notices of the Royal Astronomical Society* 451.2 (June 2015), pp. 1661–1681. ISSN: 0035-8711. DOI: 10.1093/mnras/stv1046. eprint: https://academic.oup.com/mnras/article-pdf/451/2/1661/5705021/stv1046.pdf. URL: https://doi.org/10.1093/mnras/stv1046.

[17] Savithru Jayasinghe et al. "A space-time adaptive method for reservoir flows: formulation and one-dimensional application". In: *Computational Geosciences* 22.1 (Feb. 2018), pp. 107–123. ISSN: 1573-1499. DOI: 10.1007/s10596-017-9673-9. URL: https://doi.org/10.1007/s10596-017-9673-9.

[18] Daniel Pook-Kolb et al. "Horizons in a binary black hole merger I: Geometry and area increase". In: (June 2020). arXiv: 2006.03939 [gr-qc].

[19] Daniel Pook-Kolb et al. "Horizons in a binary black hole merger II: Fluxes, multipole moments and stability". In: (June 2020). arXiv: 2006.03940 [gr-qc].

[20] B. P. Abbott et al. "GWTC-1: A Gravitational-Wave Transient Catalog of Compact Binary Mergers Observed by LIGO and Virgo during the First and Second Observing Runs". In: *Phys. Rev. X* 9.3 (2019), p. 031040. DOI: 10.1103/PhysRevX.9.031040. arXiv: 1811.12907 [astro-ph.HE].

[21] R. Abbott et al. "GWTC-2: Compact Binary Coalescences Observed by LIGO and Virgo During the First Half of the Third Observing Run". In: *Phys. Rev. X* 11 (2021), p. 021053. DOI: 10.1103/PhysRevX.11.021053. arXiv: 2010.14527 [gr-qc].

[22] R. Abbott et al. "GWTC-3: Compact Binary Coalescences Observed by LIGO and Virgo During the Second Part of the Third Observing Run". In: (Nov. 2021). arXiv: 2111.03606 [gr-qc].

[23] B. P. Abbott et al. "Tests of General Relativity with GW170817". In: *Phys. Rev. Lett.* 123.1 (2019), p. 011102. DOI: 10.1103/PhysRevLett.123.011102. arXiv: 1811.00364 [gr-qc].

[24] R. Abbott et al. "Tests of general relativity with binary black holes from the second LIGO-Virgo gravitational-wave transient catalog". In: *Phys. Rev. D* 103.12 (2021), p. 122002. DOI: 10.1103/PhysRevD.103.122002. arXiv: 2010.14529 [gr-qc].

[25] R. Abbott et al. "Tests of General Relativity with GWTC-3". In: (Dec. 2021). arXiv: 2112.06861 [gr-qc].

[26] Alvin J. K. Chua and Michele Vallisneri. "On parametric tests of relativity with false degrees of freedom". In: (June 2020). arXiv: 2006.08918 [gr-qc].

[27] Scott E. Perkins et al. "Improved gravitational-wave constraints on higher-order curvature theories of gravity". In: *Phys. Rev. D* 104.2 (2021), p. 024060. DOI: 10.1103/PhysRevD.104.024060. arXiv: 2104.11189 [gr-qc].

[28] Hai-Tian Wang et al. "Tight constraints on Einstein-dilation-Gauss-Bonnet model with the GWTC-2 events". In: *Phys. Rev. D* 104.2, 024015 (Apr. 2021), p. 024015. DOI: 10.1103/PhysRevD.104.024015. arXiv: 2104.07590 [gr-qc].

[29] Áron D. Kovács and Harvey S. Reall. "Well-Posed Formulation of Scalar-Tensor Effective Field Theory". In: *Phys. Rev. Lett.* 124.22 (2020), p. 221101. DOI: 10.1103/PhysRevLett.124.221101. arXiv: 2003.04327 [gr-qc].

[30] Áron D. Kovács and Harvey S. Reall. "Well-posed formulation of Lovelock and Horndeski theories". In: *Phys. Rev. D* 101.12 (2020), p. 124003. DOI: 10.1103/PhysRevD.101.124003. arXiv: 2003.08398 [gr-qc].

[31] William E. East and Justin L. Ripley. "Evolution of Einstein-scalar-Gauss-Bonnet gravity using a modified harmonic formulation". In: *Phys. Rev. D* 103.4 (2021), p. 044040. DOI: 10.1103/PhysRevD.103.044040. arXiv: 2011.03547 [gr-qc].

[32] William E. East and Justin L. Ripley. "Dynamics of Spontaneous Black Hole Scalarization and Mergers in Einstein-Scalar-Gauss-Bonnet Gravity". In: *Phys. Rev. Lett.* 127.10 (2021), p. 101102. DOI: 10.1103/PhysRevLett.127.101102. arXiv: 2105.08571 [gr-qc].

[33] Pau Figueras and Tiago França. "Black Hole Binaries in Cubic Horndeski Theories". In: (Dec. 2021). arXiv: 2112.15529 [gr-qc].

[34] Maria Okounkova et al. "Numerical relativity simulation of GW150914 beyond general relativity". In: *Phys. Rev. D* 101.10 (2020), p. 104016. DOI: 10.1103/PhysRevD.101.104016. arXiv: 1911.02588 [gr-qc].

[35] Maria Okounkova et al. "Numerical binary black hole collisions in dynamical Chern-Simons gravity". In: *Phys. Rev. D* 100.10 (2019), p. 104026. DOI: 10.1103/PhysRevD.100.104026. arXiv: 1906.08789 [gr-qc].

[36] Maria Okounkova. "Numerical relativity simulation of GW150914 in Einstein dilaton Gauss-Bonnet gravity". In: *Phys. Rev. D* 102.8 (2020), p. 084046. DOI: 10.1103/PhysRevD.102.084046. arXiv: 2001.03571 [gr-qc].

[37] Helvi Witek et al. "Black holes and binary mergers in scalar Gauss-Bonnet gravity: scalar field dynamics". In: *Phys. Rev. D* 99.6 (2019), p. 064035. DOI: 10.1103/PhysRevD.99.064035. arXiv: 1810.05177 [gr-qc].

[38] Hector O. Silva et al. "Dynamical Descalarization in Binary Black Hole Mergers". In: *Phys. Rev. Lett.* 127.3 (2021), p. 031101. DOI: 10.1103/PhysRevLett.127.031101. arXiv: 2012.10436 [gr-qc].

[39] José T. Gálvez Ghersi and Leo C. Stein. "Numerical renormalization-group-based approach to secular perturbation theory". In: *Phys. Rev. E* 104.3 (2021), p. 034219. DOI: 10.1103/PhysRevE.104.034219. arXiv: 2106.08410 [hep-th].

[40] Ramiro Cayuso and Luis Lehner. "Nonlinear, noniterative treatment of EFT-motivated gravity". In: *Phys. Rev. D* 102.8 (2020), p. 084008. DOI: 10.1103/PhysRevD.102.084008. arXiv: 2005.13720 [gr-qc].

[41] Eric W. Hirschmann et al. “Black Hole Dynamics in Einstein-Maxwell-Dilaton Theory”. In: *Phys. Rev. D* 97.6 (2018), p. 064032. DOI: 10.1103/PhysRevD.97.064032. arXiv: 1706.09875 [gr-qc].

[42] G. W. Gibbons and Kei-ichi Maeda. “Black Holes and Membranes in Higher Dimensional Theories with Dilaton Fields”. In: *Nucl. Phys.* B298 (1988), pp. 741–775. DOI: 10.1016/0550-3213(88)90006-5.

[43] Emanuele Berti et al. “Numerical simulations of single and binary black holes in scalar-tensor theories: circumventing the no-hair theorem”. In: *Phys. Rev. D* 87.12 (2013), p. 124020. DOI: 10.1103/PhysRevD.87.124020. arXiv: 1304.2836 [gr-qc].

[44] James Healy et al. “Late Inspiral and Merger of Binary Black Holes in Scalar-Tensor Theories of Gravity”. In: *Classical Quantum Gravity* 29 (2012), p. 232002. DOI: 10.1088/0264-9381/29/23/232002. arXiv: 1112.3928 [gr-qc].

[45] Clifford M. Will. “The Confrontation between General Relativity and Experiment”. In: *Living Rev. Relativity* 17 (2014), p. 4. DOI: 10.12942/lrr-2014-4. arXiv: 1403.7377 [gr-qc].

[46] Mohammed Khalil et al. “Hairy binary black holes in Einstein-Maxwell-dilaton theory and their effective-one-body description”. In: *Phys. Rev. D* 98.10 (2018), p. 104010. DOI: 10.1103/PhysRevD.98.104010. arXiv: 1809.03109 [gr-qc].

[47] Óscar J. C. Dias, Mahdi Godazgar, and Jorge E. Santos. “Linear Mode Stability of the Kerr-Newman Black Hole and Its Quasinormal Modes”. In: *Phys. Rev. Lett.* 114.15 (2015), p. 151101. DOI: 10.1103/PhysRevLett.114.151101. arXiv: 1501.04625 [gr-qc].

[48] Óscar J. C. Dias et al. “Eigenvalue repulsions in the quasinormal spectra of the Kerr-Newman black hole”. In: (Sept. 2021). arXiv: 2109.13949 [gr-qc].

[49] Gregorio Carullo et al. “Splitting the third hair: constraints on Kerr-Newman black holes from merger-ringdown gravitational-wave observations”. In: (Sept. 2021). arXiv: 2109.13961 [gr-qc].

[50] Banafsheh Shiralilou et al. “Post-Newtonian gravitational and scalar waves in scalar-Gauss–Bonnet gravity”. In: *Classical Quantum Gravity* 39.3 (2022), p. 035002. DOI: 10.1088/1361-6382/ac4196. arXiv: 2105.13972 [gr-qc].

[51] Noah Sennett, Sylvain Marsat, and Alessandra Buonanno. “Gravitational waveforms in scalar-tensor gravity at 2PN relative order”. In: *Phys. Rev. D* 94.8 (2016), p. 084003. DOI: 10.1103/PhysRevD.94.084003. arXiv: 1607.01420 [gr-qc].

[52] Vitor Cardoso et al. "Black holes and gravitational waves in models of minicharged dark matter". In: *J. Cosmol. Astropart. Phys.* 05 (2016). **04**, E01 (2020), p. 054. DOI: 10.1088/1475-7516/2016/05/054. arXiv: 1604.07845 [hep-ph].

[53] Kent Yagi et al. "Post-Newtonian, Quasi-Circular Binary Inspirals in Quadratic Modified Gravity". In: *Phys. Rev. D* 85 (2012). **93**, 029902(E) (2016), p. 064022. DOI: 10.1103/PhysRevD.85.064022. arXiv: 1110.5950 [gr-qc].

[54] Nathan K. Johnson-McDaniel et al. "Investigating the relation between gravitational wave tests of general relativity". In: *Phys. Rev. D* 105.4 (2022), p. 044020. DOI: 10.1103/PhysRevD.105.044020. arXiv: 2109.06988 [gr-qc].

[55] Félix-Louis Julié. "Gravitational radiation from compact binary systems in Einstein-Maxwell-dilaton theories". In: *J. Cosmol. Astropart. Phys.* 10 (2018), p. 033. DOI: 10.1088/1475-7516/2018/10/033. arXiv: 1809.05041 [gr-qc].

[56] Ruomin Zhu and Thomas Osburn. "Inspirals into a charged black hole". In: *Phys. Rev. D* 97.10 (2018), p. 104058. DOI: 10.1103/PhysRevD.97.104058. arXiv: 1802.00836 [gr-qc].

[57] Justin Y. J. Burton and Thomas Osburn. "Reissner-Nordström perturbation framework with gravitational wave applications". In: *Phys. Rev. D* 102.10 (2020), p. 104030. DOI: 10.1103/PhysRevD.102.104030. arXiv: 2010.12984 [gr-qc].

[58] T. Torres and S. R. Dolan. "Electromagnetic self-force on a charged particle on Kerr spacetime: equatorial circular orbits". In: (Aug. 2020). arXiv: 2008.12703 [gr-qc].

[59] Pawan Kumar Gupta et al. "Bounding dark charges on binary black holes using gravitational waves". In: *Phys. Rev. D* 104.6 (2021), p. 063041. DOI: 10.1103/PhysRevD.104.063041. arXiv: 2107.12111 [gr-qc].

[60] Gabriele Bozzola and Vasileios Paschalidis. "General Relativistic Simulations of the Quasicircular Inspiral and Merger of Charged Black Holes: GW150914 and Fundamental Physics Implications". In: *Phys. Rev. Lett.* 126.4 (2021), p. 041103. DOI: 10.1103/PhysRevLett.126.041103. arXiv: 2006.15764 [gr-qc].

[61] Gabriele Bozzola and Vasileios Paschalidis. "Numerical-relativity simulations of the quasicircular inspiral and merger of nonspinning, charged black holes: Methods and comparison with approximate approaches". In: *Phys. Rev. D* 104.4 (2021), p. 044004. DOI: 10.1103/PhysRevD.104.044004. arXiv: 2104.06978 [gr-qc].

[62] Wolfgang Tichy. "A New numerical method to construct binary neutron star initial data". In: *Classical Quantum Gravity* 26 (2009), p. 175018. DOI: 10.1088/0264-9381/26/17/175018. arXiv: 0908.0620 [gr-qc].

[63] Tim Dietrich et al. “Binary Neutron Stars with Generic Spin, Eccentricity, Mass ratio, and Compactness - Quasi-equilibrium Sequences and First Evolutions”. In: *Phys. Rev. D* 92.12 (2015), p. 124007. DOI: 10.1103/PhysRevD.92.124007. arXiv: 1507.07100 [gr-qc].

[64] Steven L. Liebling, Carlos Palenzuela, and Luis Lehner. “Toward fidelity and scalability in non-vacuum mergers”. In: *Classical Quantum Gravity* 37.13 (2020), p. 135006. DOI: 10.1088/1361-6382/ab8fcd. arXiv: 2002.07554 [gr-qc].

[65] Edmund M Clarke Jr et al. *Model Checking*. MIT press, 2018.

[66] G. Barrett. “Formal methods applied to a floating-point number system”. In: *IEEE Transactions on Software Engineering* 15.5 (1989), pp. 611–621. DOI: 10.1109/32.24710.

[67] Marc Daumas, Laurence Rideau, and Laurent Théry. “A Generic Library for Floating-Point Numbers and Its Application to Exact Computing”. In: *Proceedings of the 14th International Conference on Theorem Proving in Higher Order Logics*. TPHOLs ’01. Berlin, Heidelberg: Springer-Verlag, 2001, pp. 169–184. ISBN: 354042525X.

[68] John Harrison. “Formal Verification of Floating Point Trigonometric Functions”. In: *Formal Methods in Computer-Aided Design*. Ed. by Warren A. Hunt and Steven D. Johnson. Berlin, Heidelberg: Springer Berlin Heidelberg, 2000, pp. 254–270. ISBN: 978-3-540-40922-9.

[69] Daniel M. Siegel et al. “Recovery schemes for primitive variables in general-relativistic magnetohydrodynamics”. In: *Astrophys. J.* 859.1 (2018), p. 71. DOI: 10.3847/1538-4357/aabcc5. arXiv: 1712.07538 [astro-ph.HE].

[70] Leonardo de Moura and Nikolaj Bjørner. “Z3: An Efficient SMT Solver”. In: *Tools and Algorithms for the Construction and Analysis of Systems*. Ed. by C. R. Ramakrishnan and Jakob Rehof. Berlin, Heidelberg: Springer Berlin Heidelberg, 2008, pp. 337–340. ISBN: 978-3-540-78800-3.

[71] Sicun Gao, Jeremy Avigad, and Edmund Clarke. “Delta-Complete Decision Procedures for Satisfiability over the Reals”. In: *arXiv e-prints*, arXiv:1204.3513 (Apr. 2012), arXiv:1204.3513. arXiv: 1204.3513 [cs.LO].

[72] Vijay Ganesh and Moshe Y. Vardi. “On the Unreasonable Effectiveness of SAT Solvers”. In: *Beyond the Worst-Case Analysis of Algorithms*. 2020.

[73] Justyna Petke. “Bridging Constraint Satisfaction and Boolean Satisfiability”. In: *Artificial Intelligence: Foundations, Theory, and Algorithms*. 2015.

[74] Russell Impagliazzo and Ramamohan Paturi. "On the Complexity of K-SAT". In: *J. Comput. Syst. Sci.* 62.2 (Mar. 2001), pp. 367–375. ISSN: 0022-0000. DOI: 10.1006/jcss.2000.1727. URL: https://doi.org/10.1006/jcss.2000.1727.

[75] Stephen A. Cook. "The Complexity of Theorem-Proving Procedures". In: *Proceedings of the 3rd Annual ACM Symposium on Theory of Computing*. 1971, pp. 151–158. DOI: 10.1145/800157.805047.

[76] Niklas Eén and Niklas Sörensson. "An Extensible SAT-solver". In: *SAT*. 2003.

[77] Gilles Audemard and Laurent Simon. "Predicting Learnt Clauses Quality in Modern SAT Solvers". In: *Proceedings of the 21st International Joint Conference on Artificial Intelligence*. IJCAI'09. Pasadena, California, USA: Morgan Kaufmann Publishers Inc., 2009, pp. 399–404.

[78] Jia Hui Liang et al. "Learning Rate Based Branching Heuristic for SAT Solvers". In: *Proceedings of the 19th International Conference on Theory and Applications of Satisfiability Testing - SAT 2016*. 2016, pp. 123–140. DOI: 10.1007/978-3-319-40970-2_9.

[79] Carlos Ansótegui, Jesús Giráldez-Cru, and Jordi Levy. "The Community Structure of SAT Formulas". In: *Proceedings of the 15th International Conference on Theory and Applications of Satisfiability Testing - SAT 2012*. 2012, pp. 410–423. DOI: 10.1007/978-3-642-31612-8_31.

[80] Ryan Williams, Carla P. Gomes, and Bart Selman. "Backdoors To Typical Case Complexity". In: *IJCAI-03, Proceedings of the Eighteenth International Joint Conference on Artificial Intelligence*. 2003, pp. 1173–1178. URL: http://ijcai.org/Proceedings/03/Papers/168.pdf.

[81] Edward Zulkoski et al. "Learning-Sensitive Backdoors with Restarts". In: *Proceedings of the 24th International Conference on Principles and Practice of Constraint Programming*. 2018, pp. 453–469. DOI: 10.1007/978-3-319-98334-9_30.

[82] Rémi Monasson et al. "Determining Computational Complexity from Characteristic 'Phase Transitions'". In: *Nature* 400.6740 (1999), pp. 133–137.

[83] Michael Alekhnovich and Alexander Razborov. "Satisfiability, Branch-Width and Tseitin Tautologies". In: *computational complexity* 20.4 (Dec. 2011), pp. 649–678. ISSN: 1420-8954. DOI: 10.1007/s00037-011-0033-1.

[84] Marko Samer and Stefan Szeider. "Fixed-Parameter Tractability." In: *Handbook of Satisfiability*. Ed. by Armin Biere et al. Second. Vol. 336. Frontiers in Artificial Intelligence and Applications. IOS press, Feb. 2021.

[85] Robert Mateescu. *Treewidth in Industrial SAT Benchmarks*. Tech. rep. MSR-TR-2011-22. Microsoft, Feb. 2011. URL: https://www.microsoft.com/en-us/research/publication/treewidth-in-industrial-sat-benchmarks/.

[86] J. Tinsley Oden. "A general theory of finite elements. II. Applications". In: *International Journal for Numerical Methods in Engineering* 1.3 (1969), pp. 247–259. DOI: https://doi.org/10.1002/nme.1620010304. eprint: https://onlinelibrary.wiley.com/doi/pdf/10.1002/nme.1620010304. URL: https://onlinelibrary.wiley.com/doi/abs/10.1002/nme.1620010304.

[87] J. H. Argyris and A. S. L. Chan. "Applications of finite elements in space and time". In: *Ingenieur-Archiv* 41.4 (July 1972), pp. 235–257. ISSN: 1432-0681. DOI: 10.1007/BF00533764. URL: https://doi.org/10.1007/BF00533764.

[88] Thomas J. R. Hughes and Gregory M. Hulbert. "Space-time finite element methods for elastodynamics: formulations and error estimates". In: *Applied Mechanics and Engineering* 66 (1988), pp. 339–363.

[89] Gregory M. Hulbert and Thomas J.R. Hughes. "Space-time finite element methods for second-order hyperbolic equations". In: *Computer Methods in Applied Mechanics and Engineering* 84.3 (1990), pp. 327–348. ISSN: 0045-7825. DOI: https://doi.org/10.1016/0045-7825(90)90082-W. URL: https://www.sciencedirect.com/science/article/pii/004578259090082W.

[90] Frans Pretorius and Luis Lehner. "Adaptive mesh refinement for characteristic codes". In: *J. Comput. Phys.* 198 (2004), pp. 10–34. DOI: 10.1016/j.jcp.2004.01.001. arXiv: gr-qc/0302003.

[91] U. Sperhake, K. R. P. Sjodin, and J. A. Vickers. "Dynamic cosmic strings 2: Numerical evolution of excited cosmic strings". In: *Phys. Rev. D* 63 (2001), p. 024012. DOI: 10.1103/PhysRevD.63.024012. arXiv: gr-qc/0003114.

[92] Jorg Hennig and Marcus Ansorg. "A Fully Pseudospectral Scheme for Solving Singular Hyperbolic Equations on Conformally Compactified Space-Times". In: *J. Hyperbol. Diff. Equat.* 6.01 (2009), pp. 161–184. DOI: 10.1142/S0219891609001769. arXiv: 0801.1455 [gr-qc].

[93] Rodrigo Panosso Macedo and Marcus Ansorg. "Axisymmetric fully spectral code for hyperbolic equations". In: *J. Comput. Phys.* 276 (2014), pp. 357–379. DOI: 10.1016/j.jcp.2014.07.040. arXiv: 1402.7343 [physics.comp-ph].

[94] Will Farr and Edmund Bertschinger. "Numerical Relativity from a Gauge Theory Perspective". In: *APS April Meeting Abstracts*. APS Meeting Abstracts. Apr. 2008, D10.007, p. D10.007.

[95] B. Waugh and Kayll Lake. "Double-null coordinates for the Vaidya metric". In: *Phys. Rev. D* 34 (10 Nov. 1986), pp. 2978–2984. DOI: 10.1103/PhysRevD.34.2978. URL: https://link.aps.org/doi/10.1103/PhysRevD.34.2978.

[96] Rufus S. Hamade and John M. Stewart. "The Spherically symmetric collapse of a massless scalar field". In: *Class. Quant. Grav.* 13 (1996), pp. 497–512. DOI: 10.1088/0264-9381/13/3/014. arXiv: gr-qc/9506044.

[97] B. Waugh and K. Lake. "Double Null Coordinates for the Vaidya Metric". In: *Phys. Rev. D* 34 (1986), pp. 2978–2984. DOI: 10.1103/PhysRevD.34.2978.

[98] Jorge Nocedal and Stephen J. Wright. *Numerical Optimization*. 2e. New York, NY, USA: Springer, 2006.

[99] Jeffrey Winicour. "Characteristic Evolution and Matching". In: *Living Rev. Rel.* 8 (2005), p. 10. DOI: 10.12942/lrr-2005-10. arXiv: gr-qc/0508097.

[100] Robert M Wald. *General relativity*. Chicago, IL: Chicago Univ. Press, 1984. URL: https://cds.cern.ch/record/106274.

[101] Carsten Gundlach, Richard H. Price, and Jorge Pullin. "Late time behavior of stellar collapse and explosions: 2. Nonlinear evolution". In: *Phys. Rev. D* 49 (1994), pp. 890–899. DOI: 10.1103/PhysRevD.49.890. arXiv: gr-qc/9307010.

[102] David Garfinkle. "Choptuik scaling in null coordinates". In: *Phys. Rev. D* 51 (1995), pp. 5558–5561. DOI: 10.1103/PhysRevD.51.5558. arXiv: gr-qc/9412008.

[103] Eric Poisson and W. Israel. "Internal structure of black holes". In: *Phys. Rev. D* 41 (1990), pp. 1796–1809. DOI: 10.1103/PhysRevD.41.1796.

[104] Fernando Girotto and Alberto Saa. "Semi-analytical approach for the Vaidya metric in double-null coordinates". In: *Phys. Rev. D* 70 (2004), p. 084014. DOI: 10.1103/PhysRevD.70.084014. arXiv: gr-qc/0406067.

[105] John P. Boyd. *Chebyshev and Fourier Spectral Methods*. Second. Dover Books on Mathematics. Mineola, NY: Dover Publications, 2001. ISBN: 0486411834.

[106] Steven A. Orszag. "On the Elimination of Aliasing in Finite-Difference Schemes by Filtering High-Wavenumber Components." In: *Journal of Atmospheric Sciences* 28.6 (Sept. 1971), pp. 1074–1074. DOI: 10.1175/1520-0469(1971)028\textless{}1074:OTEOAI\textgreater{}2.0.CO;2.

[107] Shripad Thite. "Adaptive spacetime meshing for discontinuous Galerkin methods". In: *Computational Geometry* 42.1 (2009), pp. 20–44. ISSN: 0925-7721. DOI: https://doi.org/10.1016/j.comgeo.2008.07.003. URL: https://www.sciencedirect.com/science/article/pii/S0925772108000618.

[108] Jeff Erickson. "Adaptive Unstructured Spacetime Meshing for Four-dimensional Spacetime Discontinuous Galerkin Finite Element Methods". In: 2011.

[109] Gabriele Bozzola and Vasileios Paschalidis. "Initial data for general relativistic simulations of multiple electrically charged black holes with linear and angular momenta". In: *Phys. Rev. D* 99.10 (2019), p. 104044. DOI: 10.1103/PhysRevD.99.104044. arXiv: 1903.01036 [gr-qc].

[110] Geoffrey Lovelace et al. "Binary-black-hole initial data with nearly-extremal spins". In: *Phys. Rev. D* 78 (2008), p. 084017. DOI: 10.1103/PhysRevD.78.084017. arXiv: 0805.4192 [gr-qc].

[111] James W. York Jr. "Conformal 'thin sandwich' data for the initial-value problem". In: *Phys. Rev. Lett.* 82 (1999), pp. 1350–1353. DOI: 10.1103/PhysRevLett.82.1350. arXiv: gr-qc/9810051.

[112] Harald P. Pfeiffer and James W. York Jr. "Extrinsic curvature and the Einstein constraints". In: *Phys. Rev. D* 67 (2003), p. 044022. DOI: 10.1103/PhysRevD.67.044022. arXiv: gr-qc/0207095.

[113] Geoffrey Lovelace. "Reducing spurious gravitational radiation in binary-black-hole simulations by using conformally curved initial data". In: *Classical Quantum Gravity* 26 (2009). Ed. by Patrick Sutton and Deirdre Shoemaker, p. 114002. DOI: 10.1088/0264-9381/26/11/114002. arXiv: 0812.3132 [gr-qc].

[114] Gregory B. Cook. "Initial data for numerical relativity". In: *Living Rev. Relativity* 3 (2000), p. 5. DOI: 10.12942/lrr-2000-5. arXiv: gr-qc/0007085.

[115] Wolfgang Tichy. "The initial value problem as it relates to numerical relativity". In: *Rep. Prog. Phys.* 80.2 (2017), p. 026901. DOI: 10.1088/1361-6633/80/2/026901. arXiv: 1610.03805 [gr-qc].

[116] Miguel Alcubierre. *Introduction to 3+1 Numerical Relativity*. New York: Oxford University Press, 2008. DOI: 10.1093/acprof:oso/9780199205677.001.0001.

[117] Jeffrey M. Bowen and James W. York Jr. "Time asymmetric initial data for black holes and black hole collisions". In: *Phys. Rev. D* 21 (1980), pp. 2047–2056. DOI: 10.1103/PhysRevD.21.2047.

[118] Thomas W. Baumgarte and Stuart L. Shapiro. "Numerical relativity and compact binaries". In: *Phys. Rep.* 376 (2003), pp. 41–131. DOI: 10.1016/S0370-1573(02)00537-9. arXiv: gr-qc/0211028.

[119] Miguel Alcubierre, Juan Carlos Degollado, and Marcelo Salgado. "The Einstein-Maxwell system in 3+1 form and initial data for multiple charged black holes". In: *Phys. Rev. D* 80 (2009), p. 104022. DOI: 10.1103/PhysRevD.80.104022. arXiv: 0907.1151 [gr-qc].

[120] Serguei Ossokine et al. "Improvements to the construction of binary black hole initial data". In: *Classical Quantum Gravity* 32 (2015), p. 245010. DOI: 10.1088/0264-9381/32/24/245010. arXiv: 1506.01689 [gr-qc].

[121] Harald P. Pfeiffer et al. "Reducing orbital eccentricity in binary black hole simulations". In: *Classical Quantum Gravity* 24 (2007). Ed. by Manuela Campanelli and Luciano Rezzolla, S59–S82. DOI: 10.1088/0264-9381/24/12/S06. arXiv: gr-qc/0702106.

[122] N. Lages. "Apparent Horizons and Marginally Trapped Surfaces in Numerical General Relativity". PhD thesis. Friedrich-Schiller-Universität Jena, 2010. URL: https://www.db-thueringen.de/servlets/MCRFileNodeServlet/dbt_derivate_00019649/Lages/Dissertation.pdf.

[123] Robert Owen et al. "Black Hole Spin Axis in Numerical Relativity". In: *Phys. Rev. D* 99.8 (2019), p. 084031. DOI: 10.1103/PhysRevD.99.084031. arXiv: 1708.07325 [gr-qc].

[124] Gregory B. Cook and Bernard F. Whiting. "Approximate Killing Vectors on S**2". In: *Phys. Rev. D* 76 (2007), p. 041501. DOI: 10.1103/PhysRevD.76.041501. arXiv: 0706.0199 [gr-qc].

[125] William E. East. "Massive Boson Superradiant Instability of Black Holes: Nonlinear Growth, Saturation, and Gravitational Radiation". In: *Phys. Rev. Lett.* 121.13 (2018), p. 131104. DOI: 10.1103/PhysRevLett.121.131104. arXiv: 1807.00043 [gr-qc].

[126] Abhay Ashtekar, Stephen Fairhurst, and Badri Krishnan. "Isolated horizons: Hamiltonian evolution and the first law". In: *Phys. Rev. D* 62 (2000), p. 104025. DOI: 10.1103/PhysRevD.62.104025. arXiv: gr-qc/0005083.

[127] Abhay Ashtekar and Badri Krishnan. "Isolated and dynamical horizons and their applications". In: *Living Rev. Relativity* 7 (2004), p. 10. DOI: 10.12942/lrr-2004-10. arXiv: gr-qc/0407042.

[128] G. C. Reifenberger. "Binary Black Hole Mergers: Alternatives to Standard Puncture Initial Data and the Impact on Gravitational Waveforms". PhD thesis. Florida Atlantic University, 2013. URL: http://fau.digital.flvc.org/islandora/object/fau%3A4224.

[129] Marcus Ansorg. "Multi-Domain Spectral Method for Initial Data of Arbitrary Binaries in General Relativity". In: *Classical Quantum Gravity* 24.12 (2007). Ed. by Manuela Campanelli and Luciano Rezzolla, S1–S14. DOI: 10.1088/0264-9381/24/12/S01. arXiv: gr-qc/0612081.

[130] Pedro Marronetti et al. "Binary black holes on a budget: Simulations using workstations". In: *Classical Quantum Gravity* 24 (2007). Ed. by Manuela Campanelli and Luciano Rezzolla, S43–S58. DOI: 10.1088/0264-9381/24/12/S05. arXiv: gr-qc/0701123.

[131] Hwei-Jang Yo, Thomas W. Baumgarte, and Stuart L. Shapiro. "Improved numerical stability of stationary black hole evolution calculations". In: *Phys. Rev. D* 66 (2002), p. 084026. DOI: 10.1103/PhysRevD.66.084026. arXiv: gr-qc/0209066.

[132] Erik Schnetter, Badri Krishnan, and Florian Beyer. "Introduction to dynamical horizons in numerical relativity". In: *Phys. Rev. D* 74 (2006), p. 024028. DOI: 10.1103/PhysRevD.74.024028. arXiv: gr-qc/0604015.

[133] Abhay Ashtekar, Christopher Beetle, and Jerzy Lewandowski. "Mechanics of rotating isolated horizons". In: *Phys. Rev. D* 64 (2001), p. 044016. DOI: 10.1103/PhysRevD.64.044016. arXiv: gr-qc/0103026.

[134] D. Christodoulou and R. Ruffini. "Reversible transformations of a charged black hole". In: *Phys. Rev. D* 4 (1971), pp. 3552–3555. DOI: 10.1103/PhysRevD.4.3552.

[135] E. (Ted) Newman and T. Adamo. "Kerr-Newman metric". In: *Scholarpedia* 9.10 (2014). revision #144839, p. 31791. DOI: 10.4249/scholarpedia.31791.

[136] Abdul H. Mroué and Harald P. Pfeiffer. "Precessing Binary Black Holes Simulations: Quasicircular Initial Data". In: (Oct. 2012). arXiv: 1210.2958 [gr-qc].

[137] Miguel Zilhao et al. "Collisions of charged black holes". In: *Phys. Rev. D* 85 (2012), p. 124062. DOI: 10.1103/PhysRevD.85.124062. arXiv: 1205.1063 [gr-qc].

[138] Miguel Zilhão et al. "Collisions of oppositely charged black holes". In: *Phys. Rev. D* 89.4 (2014), p. 044008. DOI: 10.1103/PhysRevD.89.044008. arXiv: 1311.6483 [gr-qc].

[139] Steven L. Liebling and Carlos Palenzuela. "Electromagnetic Luminosity of the Coalescence of Charged Black Hole Binaries". In: *Phys. Rev. D* 94.6 (2016), p. 064046. DOI: 10.1103/PhysRevD.94.064046. arXiv: 1607.02140 [gr-qc].

[140] Gabriele Bozzola. "Does Charge Matter in High-Energy Collisions of Black Holes?" In: *Phys. Rev. Lett.* 128.7 (2022), p. 071101. DOI: 10.1103/PhysRevLett.128.071101. arXiv: 2202.05310 [gr-qc].

[141] Sascha Husa et al. "Frequency-domain gravitational waves from nonprecessing black-hole binaries. I. New numerical waveforms and anatomy of the signal". In: *Phys. Rev. D* 93.4 (2016), p. 044006. DOI: 10.1103/PhysRevD.93.044006. arXiv: 1508.07250 [gr-qc].

[142] Ezra Newman and Roger Penrose. "An Approach to gravitational radiation by a method of spin coefficients". In: *J. Math. Phys. (N.Y.)* 3 (1962), pp. 566–578. DOI: 10.1063/1.1724257.

[143] Micheal Boyle. *Quaternionic package*. https://github.com/moble/quaternionic. 2017.

[144] Michael Boyle. "How should spin-weighted spherical functions be defined?" In: *J. Math. Phys. (N.Y.)* 57.9 (2016), p. 092504. DOI: 10.1063/1.4962723. arXiv: 1604.08140 [gr-qc].

[145] J. David Brown et al. "Turduckening black holes: An Analytical and computational study". In: *Phys. Rev. D* 79 (2009), p. 044023. DOI: 10.1103/PhysRevD.79.044023. arXiv: 0809.3533 [gr-qc].

[146] Vijay Varma, Mark A. Scheel, and Harald P. Pfeiffer. "Comparison of binary black hole initial data sets". In: *Phys. Rev. D* 98.10 (2018), p. 104011. DOI: 10.1103/PhysRevD.98.104011. arXiv: 1808.08228 [gr-qc].

[147] Edward Zulkoski et al. "The Effect of Structural Measures and Merges on SAT Solver Performance". In: *Proceedings of the 24th International Conference on Principles and Practice of Constraint Programming*. 2018, pp. 436–452. DOI: 10.1007/978-3-319-98334-9_29.

[148] Tobias Friedrich et al. "Phase Transitions for Scale-Free SAT Formulas". In: *Proceedings of the Thirty-First AAAI Conference on Artificial Intelligence*. AAAI'17. San Francisco, California, USA: AAAI Press, 2017, pp. 3893–3899.

[149] Nathan Mull, Daniel J. Fremont, and Sanjit A. Seshia. "On the Hardness of SAT with Community Structure". In: *Proceedings of the 19th International Conference on Theory and Applications of Satisfiability Testing (SAT)*. July 2016, pp. 141–159. DOI: 10.1007/978-3-319-40970-2_10.

[150] Zack Newsham et al. "Impact of Community Structure on SAT Solver Performance". In: *Theory and Applications of Satisfiability Testing - SAT 2014 - 17th International Conference, Held as Part of the Vienna Summer of Logic, VSL 2014, Vienna, Austria, July 14-17, 2014. Proceedings*. 2014, pp. 252–268. DOI: 10.1007/978-3-319-09284-3_20.

[151] Herbert A. Simon. "The Architecture of Complexity". In: *Proceedings of the American Philosophical Society* 106.6 (1962), pp. 467–482. ISSN: 0003049X. URL: http://www.jstor.org/stable/985254.

[152] M. Girvan and M. E. J. Newman. "Community structure in social and biological networks". In: *Proceedings of the National Academy of Science* 99.12 (June 2002), pp. 7821–7826. DOI: 10.1073/pnas.122653799. arXiv: cond-mat/0112110 [cond-mat.stat-mech].

[153] Aaron Clauset, Cristopher Moore, and M. E. J. Newman. "Hierarchical Structure and the Prediction of Missing Links in Networks". In: *Nature* 453.7191 (May 2008), pp. 98–101. ISSN: 1476-4687. DOI: 10.1038/nature06830.

[154] Vincent Blondel et al. "Fast Unfolding of Communities in Large Networks". In: *Journal of Statistical Mechanics Theory and Experiment* 2008 (Apr. 2008). DOI: 10.1088/1742-5468/2008/10/P10008.

[155] The igraph Core Team. "igraph". In: (Apr. 2022). DOI: 10.5281/zenodo.6425453.

[156] Leo Breiman. "Random Forests". In: *Mach. Learn.* 45.1 (Oct. 2001), pp. 5–32. ISSN: 0885-6125. DOI: 10.1023/A:1010933404324. URL: https://doi.org/10.1023/A:1010933404324.

[157] T. Hastie, R. Tibshirani, and J.H. Friedman. *The Elements of Statistical Learning: Data Mining, Inference, and Prediction*. Springer series in statistics. Springer, 2009. ISBN: 9780387848846. URL: https://books.google.ca/books?id=eBSgoAEACAAJ.

[158] F. Pedregosa et al. "Scikit-learn: Machine Learning in Python". In: *Journal of Machine Learning Research* 12 (2011), pp. 2825–2830.

[159] Laurens van der Maaten and Geoffrey Hinton. "Visualizing Data using t-SNE". In: *Journal of Machine Learning Research* 9.86 (2008), pp. 2579–2605. URL: http://jmlr.org/papers/v9/vandermaaten08a.html.

[160] S. Kullback and R. A. Leibler. "On Information and Sufficiency". In: *The Annals of Mathematical Statistics* 22.1 (1951), pp. 79–86. DOI: 10.1214/aoms/1177729694. URL: https://doi.org/10.1214/aoms/1177729694.

[161] Robert George Douglas Steel and James Hiram Torrie. *Principles and Procedures of Statistics*. McGraw-Hill, 1960.

[162] Burkhard Kleihaus, Jutta Kunz, and Francisco Navarro-Lérida. "Global charges of stationary nonAbelian black holes". In: *Phys. Rev. Lett.* 90 (2003), p. 171101. DOI: 10.1103/PhysRevLett.90.171101. arXiv: hep-th/0210197.

[163] Burkhard Kleihaus, Jutta Kunz, and Francisco Navarro-Lérida. "Stationary black holes with static and counter rotating horizons". In: *Phys. Rev. D* 69 (2004), p. 081501. DOI: 10.1103/PhysRevD.69.081501. arXiv: gr-qc/0309082.

[164] Valeri P. Frolov, A. I. Zelnikov, and U. Bleyer. "Charged Rotating Black Hole From Five-dimensional Point of View". In: *Ann. Phys. (N.Y.)* 44 (1987), pp. 371–377. DOI: 10.1002/andp.19874990509.

[165] Daniel Henry Gottlieb, M. Yousuff Hussaini, and Steven A. Orszag. "Theory and applications of spectral methods". In: 1984.

[166] Lloyd N. Trefethen. *Spectral Methods in MATLAB*. USA: Society for Industrial and Applied Mathematics, 2000. ISBN: 0898714656.

[167] G. C. Debney, Roy P. Kerr, and A. Schild. "Solutions of the Einstein and Einstein-Maxwell Equations". In: *J. Math. Phys. (N.Y.)* 10 (1969), p. 1842. DOI: 10.1063/1.1664769.

[168] Erin Bonning et al. "Physics and initial data for multiple black hole space-times". In: *Phys. Rev. D* 68 (2003), p. 044019. DOI: 10.1103/PhysRevD.68.044019. arXiv: gr-qc/0305071.

# Appendices

# Appendix A

# Pseudospectral method using Chebyshev Gauss Lobatto points

In this Appendix, we list the expressions for the Chebyshev Gauss Lobatto collocation points, the associated derivative operator, and the integration weights, in one dimension. The collocation points $x_i$, for a grid of size $N+1$, corresponding to a pseudospectral method of order $N$, are given by

$$x_i = \cos\left(\frac{\pi i}{N}\right), \qquad i = 0, \ldots, N \tag{A.1}$$

The one dimensional derivative operator is given by (see, e.g., [165])

$$D_{ij} = \begin{cases} \left(1+2N^2\right)/6 & i = j = 0 \\ -\left(1+2N^2\right)/6 & i = j = N \\ -x_j/\left[2\left(1-x_j^2\right)\right] & i = j;\ 0 < j < N \\ (-1)^{i+j}\beta_i/\left[p_j\left(x_i - x_j\right)\right] & i \neq j \end{cases} \tag{A.2}$$

where $\beta_j = 1$ and $\beta_0 = \beta_N = 2$. Finally the quadrature weights for these collocation points are given by (see, e.g., Chapter 12 in [166])

$$w_j = 1 + \sum_{j=2}^{N} \frac{q_i l_j}{N(1-j^2)} \cos\left[\frac{\pi i j}{N}\right], \quad q_0 = q_N = 1, q_i = 2, \tag{A.3}$$

where $l_j = 1$ if $j$ is even, and zero otherwise. These weights can be arranged into an operator $W_{ij} = \mathrm{diag}(w_j)$, which we denote as the one dimensional integration operator in Sec. 2.1.2.

# Appendix B

# Kerr-Newman black hole in Kerr-Schild coordinates

In the 3+1 setting, the spatial metric and extrinsic curvature for a stationary Kerr-Newman black hole in Kerr-Schild coordinates are given by [167, 135]

$$\gamma_{ij} = f_{ij} + 2Hl_i l_j, \tag{B.1a}$$

$$K_{ij} = \frac{1}{2\alpha}\left(\nabla_i \beta_j + \nabla_j \beta_i - \partial_t \gamma_{ij}\right), \tag{B.1b}$$

where the lapse $\alpha$ and the shift $\beta_i$ are given by

$$\alpha = \frac{1}{\sqrt{1+2Hl_0^2}}, \qquad \beta_i = 2Hl_0 l_i, \tag{B.2}$$

writing these in a form that makes it easy to compute their boosted form, following [168]. In the above equations, the metric function $H$ and the null vector $l_\mu \doteq \{l_0, l_i\}$ are given by

$$H = \frac{Mr^3 - (Qr)^2/2}{r^4 + (\mathbf{a}\cdot\mathbf{x})^2}, \tag{B.3a}$$

$$l_\mu \doteq \left\{1, \frac{r\left[\mathbf{x} - (\hat{\mathbf{a}}\cdot\mathbf{x})\,\hat{\mathbf{a}}\right] - (\mathbf{a}\times\mathbf{x})}{r^2 + a^2} + \frac{(\hat{\mathbf{a}}\cdot\mathbf{x})\,\hat{\mathbf{a}}}{r}\right\}, \tag{B.3b}$$

where $\mathbf{x} \doteq \{x, y, z\}$ is the three dimensional coordinate vector, $\mathbf{a} = a\,\hat{\mathbf{a}}$ is the angular momentum per unit mass, and $M$ and $Q$ are the mass and charge of the black hole,

respectively. Here we use $\doteq$ to denote that we are giving the components of a vector. The parameter $r$ is given by

$$r^2 = \frac{1}{2}(\rho^2 - a^2) + \sqrt{\frac{1}{4}\left(\rho^2 - a^2\right)^2 + (\mathbf{a}\cdot\mathbf{x})^2}, \tag{B.4a}$$

$$\rho^2 = x^2 + y^2 + z^2. \tag{B.4b}$$

Note that in Eq. (B.3b) and in Eq. (B.5) below, we use the Euclidean cross product. To compute the electric and magnetic fields for a Kerr-Newman black hole, we use the four-potential [135]

$$A_\mu \doteq -\frac{Qr^3}{r^4 + (\mathbf{a}\cdot\mathbf{x})^2}\Big\{1, \frac{r\left[\mathbf{x} - (\hat{\mathbf{a}}\cdot\mathbf{x})\,\hat{\mathbf{a}}\right] - \mathbf{a}\times\mathbf{x}}{r^2 + a^2} + \frac{(\hat{\mathbf{a}}\cdot\mathbf{x})\,\hat{\mathbf{a}}}{r}\Big\}, \tag{B.5}$$

and compute the electric and magnetic field using [119]

$$E^\mu := -n_\nu F^{\nu\mu}, \quad B^\mu := -n_\nu {}^*F^{\nu\mu}, \tag{B.6}$$

where $n_\mu \doteq \{\alpha, 0, 0, 0\}$ is the four velocity of an Eulerian observer, and $F_{\mu\nu}$ and ${}^*F^{\mu\nu}$ are the Faraday tensor and its dual

$$F_{\mu\nu} = \partial_\mu A_\nu - \partial_\nu A_\mu, \quad {}^*F^{\mu\nu} := -\frac{1}{2}\epsilon^{\mu\nu\eta\gamma}F_{\eta\gamma}. \tag{B.7}$$

Here $\epsilon^{\mu\nu\eta\gamma}$ is the curved-space Levi-Civita symbol, such that $\epsilon^{0123} = -1/\sqrt{-g}$, where $g$ is the determinant of the full 4-dimensional spacetime metric.

For a boosted Kerr-Newman black hole, we first compute $H$ and the vector quantities $U_\mu \in \{l_\mu, n_\mu, A_\mu\}$ in the boosted coordinates $\bar{x}_\alpha$, given by

$$x^\beta = \Lambda^\beta{}_\alpha\, \bar{x}^\alpha, \tag{B.8}$$

where $x^\alpha$ are the inertial (grid) coordinates and $\Lambda^\beta{}_\alpha$ is the Lorentz transformation matrix relating the two frames, and then apply the Lorentz transformation to the vectors themselves, i.e.,

$$H(x^\alpha) = \bar{H}\big([\Lambda^{-1}]^\beta{}_\alpha\, x^\alpha\big), \tag{B.9a}$$

$$U_\delta(x^\alpha) = \Lambda^\gamma{}_\delta\, \bar{U}_\gamma\big([\Lambda^{-1}]^\beta{}_\alpha\, x^\alpha\big), \tag{B.9b}$$

where barred quantities correspond to the boosted frame. We then use Eqs. (B.1), (B.2), (B.6), and (B.7) to compute the relevant quantities for the boosted black hole.

# Appendix C

# Linearized XCTS equations

To solve the non-linear equations (3.3) and (3.16), together with the boundary conditions (3.9), (3.10), (3.12), and (3.21), we need to compute their linearized counterparts. Consider the linearized variables $\hat{\psi}$, $\hat{\beta}_i$, $\widehat{\alpha\psi}$ and $\hat{\phi}$. We compute the Fréchet derivatives for all the terms that are functions of these variables; see, e.g., Appendix C in [105] on how to compute these derivatives. The linearized versions of Eq. (3.3) read

$$\tilde{\nabla}^2\hat{\psi} - \frac{1}{8}\tilde{R}\hat{\psi} - \frac{5}{12}K^2\psi^4\hat{\psi} - \frac{7}{8}\psi^{-8}\hat{\psi}\tilde{A}^{ij}\tilde{A}_{ij} + \frac{1}{8}\psi^{-7}\widehat{\tilde{A}^{ij}\tilde{A}_{ij}} = -2\pi\psi^5\hat{\rho} - 10\pi\psi^4\hat{\psi}\rho, \quad \text{(C.1a)}$$

$$\begin{aligned}&\partial_j\left[\frac{7\psi^6\hat{\psi}}{2(\alpha\psi)} - \frac{\psi^7\widehat{\alpha\psi}}{2(\alpha\psi)^2}\right]\left(\tilde{L}\beta\right)^{ij} + \partial_j\left[\frac{\psi^7}{2(\alpha\psi)}\right]\left(\tilde{L}\hat{\beta}\right)^{ij} + \frac{7\psi^6\hat{\psi}}{2(\alpha\psi)}\tilde{\nabla}_j\left[\left(\tilde{L}\beta\right)^{ij}\right]\\ &- \frac{\psi^7\widehat{\alpha\psi}}{2(\alpha\psi)^2}\tilde{\nabla}_j\left[\left(\tilde{L}\beta\right)^{ij}\right] + \frac{\psi^7}{2(\alpha\psi)}\tilde{\nabla}_j\left[\left(\tilde{L}\hat{\beta}\right)^{ij}\right] - 4\psi^5\hat{\psi}\tilde{\nabla}^i K = 80\pi\psi^9\hat{\psi}J^i + 8\pi\psi^{10}\hat{J}^i,\end{aligned} \quad \text{(C.1b)}$$

$$\begin{aligned}&\tilde{\nabla}^2(\widehat{\alpha\psi}) - (\widehat{\alpha\psi})\left[\frac{\tilde{R}}{8} + \frac{5}{12}K^2\psi^4 + \frac{7}{8}\psi^{-8}\tilde{A}^{ij}\tilde{A}_{ij}\right] - (\alpha\psi)\left[\frac{5}{3}K^2\psi^3\hat{\psi} - \frac{7}{\psi^9}\hat{\psi}\tilde{A}^{ij}\tilde{A}_{ij} + \frac{7}{8}\psi^{-8}\widehat{\tilde{A}^{ij}\tilde{A}_{ij}}\right]\\ &- 5\psi^4\hat{\psi}\beta^k\partial_k K - \psi^5\hat{\beta}^k\partial_k K = (\widehat{\alpha\psi})\left[2\pi\psi^4(\rho+2S)\right] + (\alpha\psi)\left[8\pi\psi^3\hat{\psi}(\rho+2S)\right]\\ &\qquad + (\alpha\psi)\left[2\pi\psi^4(\hat{\rho}+2\hat{S})\right],\end{aligned} \quad \text{(C.1c)}$$

where we have used the two intermediate linearized quantities

$$\widehat{\tilde{A}^{ij}\tilde{A}_{ij}} = \frac{\psi^7}{(\alpha\psi)}\left[\tilde{A}^{ij}(\tilde{L}\hat{\beta})_{ij}\right] + \left[\frac{14\hat{\psi}}{\psi} - \frac{2\widehat{\alpha\psi}}{\alpha\psi}\right]\tilde{A}^{ij}\tilde{A}_{ij}, \tag{C.2}$$

$$(\tilde{L}\hat{\beta})_{ij} = \tilde{\nabla}_i\hat{\beta}_j + \tilde{\nabla}_j\hat{\beta}_i - \frac{2}{3}\tilde{\gamma}_{ij}\tilde{\nabla}_k\hat{\beta}^k, \tag{C.3}$$

and the linearized source terms $\hat{\rho}$ and $\hat{J}^i$ that are given by

$$\hat{\rho} = \hat{S} = \frac{1}{4\pi\psi^4}\left[\tilde{\gamma}^{jm}(\hat{B}_jB_m + \hat{E}_jE_m) - 2\,\tilde{\gamma}^{jk}\frac{\hat{\psi}}{\psi}(B_jB_k + E_jE_k)\right], \tag{C.4}$$

$$\hat{J}^i = \frac{\tilde{\gamma}^{im}\sqrt{\tilde{\gamma}}}{4\pi\psi^6}\epsilon^F_{mkl}\left[\tilde{\gamma}^{kn}\tilde{\gamma}^{lm}(\hat{E}_nB_m + E_n\hat{B}_m - \frac{6\hat{\psi}}{\psi}E_nB_m)\right], \tag{C.5}$$

In the above equations, we have further used

$$\hat{E}_j = \partial_j\hat{\phi}, \tag{C.6}$$

$$\hat{B}_i = -\frac{2\hat{\psi}\,\tilde{\gamma}_{ij}}{\psi^3\sqrt{\tilde{\gamma}}}\,\epsilon_F^{jkl}\partial_k(A_{\rm sp})_l, \tag{C.7}$$

Further, for Eq. (3.16), the linear equation for $\hat{\phi}$ reads

$$\begin{aligned}\tilde{\nabla}^2\hat{\phi} + 2\,\partial^k\left(\frac{\hat{\psi}}{\psi}\right)\partial_k\phi + 2\,(\partial^k\ln\psi)\,\partial_k\hat{\phi} = &\left(-\frac{2\,\hat{\psi}}{\psi^3\sqrt{\tilde{\gamma}}} + \frac{1}{\psi^2\sqrt{\tilde{\gamma}}}\right)\partial_k\left[\tilde{\gamma}^{km}(E_{\rm sp})_m\psi^2\sqrt{\tilde{g}}\right]\\ &+ \frac{1}{\psi^2\sqrt{\tilde{\gamma}}}\,\partial_k\left[2\,\tilde{\gamma}^{km}(E_{\rm sp})_m\,\psi\hat{\psi}\,\sqrt{\tilde{\gamma}}\right],\end{aligned} \tag{C.8}$$

which can be simplified further to get

Finally, for those boundary conditions which are functions of the non-linear variables themselves, i.e., for Eqs.(3.12), (3.10), , and (3.21), we get

$$\begin{aligned}\tilde{s}^k\partial_k\hat{\psi} = &-\left[\frac{\psi^3}{2(\alpha\psi)}\hat{\psi} - \frac{\psi^4}{8(\alpha\psi)^2}\widehat{\alpha\psi}\right]\tilde{s}^a\tilde{s}^b(\tilde{L}\beta)_{ab} - \frac{\psi^4}{8(\alpha\psi)}\tilde{s}^a\tilde{s}^b(\tilde{L}\hat{\beta})_{ab}\\ &- \frac{\hat{\psi}}{4}\tilde{h}^{ab}\tilde{\nabla}_a\tilde{s}_b + \frac{1}{2}K\psi^2\hat{\psi},\end{aligned} \tag{C.9}$$

$$\hat{\beta}_i = \left[\frac{\widehat{\alpha\psi}}{\psi} - \frac{\alpha\psi}{\psi^2}\hat{\psi}\right]s_i + 4\Omega^k_r\psi^3\hat{\psi}\tilde{\gamma}_{im}\xi^m_{(k)}, \tag{C.10}$$

$$\tilde{\gamma}^{am}s_m\partial_a\hat{\phi} = \hat{\zeta}\,\tilde{\gamma}^{am}s_m(E_{\rm sp})_a, \tag{C.11}$$

respectively, where

$$\hat{\zeta} = -4\pi Q_{\rm H} \left[ 2 \oint_{\mathcal{S}} \hat{\psi}\psi \tilde{g}^{ab} (E_{\rm sp})_a \sqrt{\tilde{h}}\, dS_b \right] \left[ \oint_{\mathcal{S}} \psi^2 \tilde{g}^{ab} (E_{\rm sp})_a \sqrt{\tilde{h}}\, dS_b \right]^{-2} \tag{C.12}$$

is the linearized version of Eq. (3.43). Here $\tilde{S}_a$ is the conformal spherical surface element.